Development of a dual ECIS-SPR sensor platform for cell-based assays:

Label-free analysis of g-protein coupled receptor signal transduction

DISSERTATION

zur Erlangung des Doktorgrades

der Naturwissenschaften (Dr. rer. nat.) der

Fakultät Chemie Pharmazie an der

Universität Regensburg

vorgelegt von **Zlatko Parić** aus Moosburg an der Isar, 2019

Diese Doktorarbeit entstand im Zeitraum von Juni 2014 bis Juni 2019 am Institut für Analytische Chemie, Chemo- und Biosensorik der Fakultät Chemie und Pharmazie an der Universität Regensburg.

Diese Arbeit wurde angeleitet von Prof. Dr. Joachim Wegener.

Promotionsgesuch eingereicht am:		4.12.2019
Disputation am:		5.02.2020
Prüfungsausschuss:	Vorsitzender:	Prof. Dr. Oliver Tepner
	Erstgutachter:	Prof. Dr. Joachim Wegener
	Zweitgutachterin:	Prof. Dr. Antje Bäumner
	Drittprüfer:	Prof. Dr. Rainer Müller

This work was financed and supported by the Deutsche Forschungsgemeinschaft (DFG),

GRK 1910 “Medicinal Chemistry of Selective GPCR Ligands”

Mache dich auf, werde Licht;

Jesaja 60, 1

Contents

1 Introduction

1.1 G-Protein Coupled Receptors (GPCRs)

Two main groups of membrane proteins exist: peripheral and integral membrane proteins. Integral membrane proteins are integrated into the membrane and are often composed of an intracellular, an extracellular and a transmembrane domain. Peripheral membrane proteins contain a residue with a hydrophobic side chain which interacts with membrane phospholipids for anchoring the protein to the membrane [1]. G-Protein coupled receptors (GPCR) represent the largest and multifunctional group of integral membrane receptors, which represent a huge class of drug targets [2-5]. The human genome encodes over 800 GPCRs [6]. GPCRs can be classified in five major families. The largest class has about 700 members, named the rhodopsin like receptor family. Furthermore there are adhesion, secretin, glutamate and frizzled/taste receptors [7]. Another part of the GPCR superfamily is the group of orphan receptors with not yet identified endogenous ligands and functions [8]. The GPCR superfamily has structural similarities containing an N-terminal extracellular domain, seven transmembrane domains (seven transmembrane or 7TM receptors) which are connected by three extracellular and three intracellular loops and a C-terminal domain in the intracellular space [9]. Signal transduction is mediated by the activated G-proteins. The heterometric G-protein was discovered more than 40 years ago. GPCR mediated signal transduction is triggered by ligand binding which leads to conformational changes of the receptor leading to activation of the G-protein [10, 11]. G-proteins consist of three polypeptides, GDP/GTP-binding G-α subunit and the G-βγ dimer [12]. Initially the G-α and the G-βγ subunit are non-covalently bound to each other. The activation is resulting after the agonist binds to the receptor extracellularly and the latter relays the signal into the inner side of the cell. G-protein activation by the receptor results in the exchange of guanosine diphosphate (GDP) for guanosine triphosphate (GTP) within the G-α subunit. After the GDP/GTP exchange, the G-protein separates into G-α and the G-βγ subunit. The two subunits have the ability to stimulate different pathways in the cell [13]. The endurance of the signalling depends on the rate of the intrinsic GTP hydrolysis by the G-α subunit and the following re-association of the G-α-GDP with the G-βγ part [14, 15]. Currently there are 16 mammalian G-α subunits described, based on the sequence of the G-α subunit and their functional proteins.

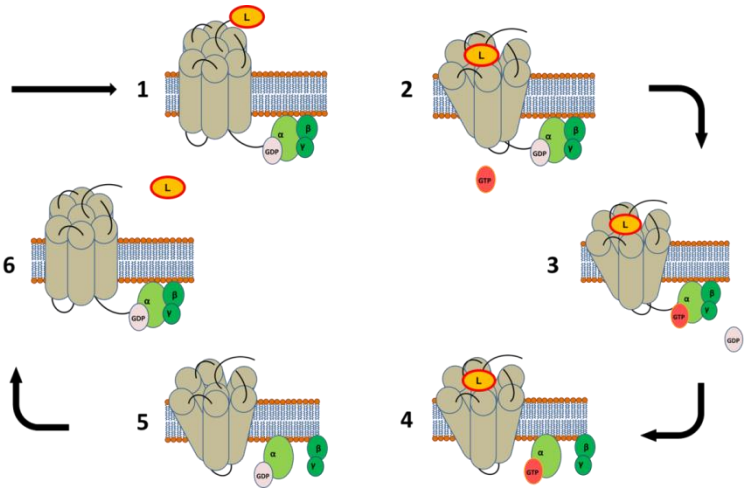

Fig. 1-1 shows the activation of a G-protein coupled receptor (GPCR). (1) Ligand (L) binding to the external domain. (2) Ligand induced conformational change. (3) G-protein activation (GDP-GTP exchange). (4) Dissociation of the G-α and G-βγ subunits inducing further signal transduction. (5) GTP hydrolyses to GDP. (6) Re-association of the G-α and G-βγ subunits and reset to an inactivated GPCR.

G-proteins are grouped into four classes: $G\alpha_{i/o}$, $G\alpha_{s}$, $G\alpha_{q/11}$ and $G\alpha_{12/13}$ [14, 16, 17]. In addition there are 5 known isoforms of the G-β and 12 of the G-γ subunit [16]. G-proteins may activate or inhibit adenylyl cyclase activity, followed by an decrease or increase in intracellular cyclic AMP (cAMP) levels, always dependent on the G-protein subtype ($G\alpha_{i/o}$- or $G\alpha_{s}$-subunit) [18-20]. The second messenger cAMP is able to activate different signals like the transcription factor CREB (cAMP response element binding protein), the Rap guanine exchange factor Epac (exchange protein activated by cAMP) or activate the cAMP dependent protein kinase A (PKA) [18, 20-22]. There is a wider scope of the role of $G\alpha_{i/o}$ proteins, like AC independent responses e.g. the blocking of calcium channels, by stimulation of G-protein inwardly rectifying potassium channels (GIRK) and stimulating the phosphodiesterase [4, 21]. ACs are controlled not only by $G\alpha_{s}$ and $G\alpha_{i/o}$ proteins, but also by the G-βγ subunit via calcium-calmodulin [16].

The $G\alpha_{q/11}$ subunit induces the stimulation of phospholipase C (PLC) that leads to the formation of inositol triphosphate (IP_3) and diacylglycerol (DAG). The release of calcium ions to the cytosol results from stimulation of IP3-sensitive receptors located in the membrane of the endoplasmatic reticulum. Diacylglycerol is able to activate protein kinase C (PKC) in co-presence of Ca^{2+} [17, 21, 23]. G12 is the latest discovery in the Gα protein subfamily consisting of two members, the $G\alpha_{12}$ and the $G\alpha_{13}$ protein. The G12 subfamily is associated with the activation of 25 different GPCRs [24, 25]. The coupling of GPCRs to the $G\alpha_{12/13}$ subunit activates GTPase´s like Rho A, furthermore it has been reported that $G\alpha_{12/13}$ is involved in cell proliferation and morphological changes [13, 26]. G-βγ subunits interact with small GTP-binding proteins, phosphatidylinositol-3-kinases(PI3K) and effectors like mitogen-activated protein kinases (MAPKs) [27]. The GPCR desensitization and downregulation is

affected by dissociated G-βγ subunits [28]. The desensitization of receptors after activation with an agonist terminates the signalling process and represents a significant step in the regulation of GPCR mediated effects [29]. GPCRs are often characterized with respect to their coupling to distinct G-proteins while an increasing fraction of GPCRs has been identified as unselective receptors having the ability of coupling to various G-proteins [30, 31].

The GPCRs have a wide range of activators including physical and chemical stimuli. Neurotransmitters, hormones, peptides, ions and light can activate GPCRs where the signal is subsequently transduced into a cellular response [32]. GPCRs are involved in a lot of physiological functions and in a vast number of different diseases [33, 34]. Further signalling mechanisms are G-protein independent [4, 35, 36]. GPCRs use different pathways for signal transduction, the canonical (G-protein mediated) and the non-canonical way (G-protein independent) like β-arrestin [37]. Arrestin function was discovered through their ability to terminate G-protein mediated signalling by the interaction with phosphorylated, ligand activated GPCRs and inducing receptor internalization [38, 39]. This process involves G-protein coupled receptor kinases (GRKs), and after internalization, GPCRs get recycled by re-integration into the membrane or by dismantling them. Arrestins, which exist in four isoforms, have the ability to regulate a vast majority of GPCRs. Beside their role in desensitizing the receptor, these proteins have the ability to trigger various signalling pathways that are different from classical G-protein mediated impact [37, 38, 40, 41].

Successful sequencing genomes of vertebrates and invertebrates changed the GPCR drug development. Researchers have successfully sequenced the entire genome today but knowledge about function and interactions of the encoded proteins is not yet complete. More than 30 % of today's drugs address GPCRs as targets. There is still a large number of G protein coupled receptors to be studied and validated for further drug discovery [42]. The GPCR superfamily is the most successful target in terms of drug discovery [43]. The signalling of GPCRs is not only depending on the G-protein subfamily it is also depending on the cellular background of the cells under study [44].

1.2 Canonical assays

Traditional GPCR assays have a variety of detection principles to report on GPCR-ligand interactions, receptor activation and receptor triggered pathways. Two main groups of GPCR assays have been defined as ligand-binding assays and functional assays. GPCR research advanced since the early 1970s with the development of radio ligand binding assays [45, 46]. Principally there are three kinds of ligand-binding experiments to perform [47]. There are kinetic experiments where association (k_{on}) and dissociation (k_{off}) rate constants are

determined. Determination of the binding constant (K_i) of non-labelled ligands by replacing a radio ligand from the binding pocket is performed with competition experiments. The information provided by radio ligand binding assays do not contain information on the pharmacological nature of the compound under test, which might be an agonist, an antagonist or an inverse agonist [6].

In the twentieth century functional assays were based on laboratory animals and preparations of their isolated organs and tissues, which had a central role in drug research before the development of reductionist cellular and molecular model systems. Today's GPCR ligand research is usually based on human receptors of interest expressed in appropriate host cells – often including the proteins of the entire signalling pathway. This enables the clear characterization of agonists, antagonists or inverse agonists. These assays are mostly performed as endpoint assays and often require cell lysis. Assays for the determination of transient changes in the cytosolic calcium concentration (Ca^{2+}), resulting from calcium release from the intracellular store like endoplasmatic reticulum (ER), are easily followed by calcium-sensitive fluorescent dyes ([48, 49]). Intracellular calcium (Ca^{2+}) is monitored in real time by using calcium sensitive dyes like Fura-2, Fluo-3 or Fluo-4. The data provides information on agonists, antagonists and from allosteric modulators but not from inverse agonists [48, 50]. The GPCR mediated calcium signal is predominantly depending on $G\alpha_{q/11}$ coupling [51].

Our present knowledge of GPCR pharmacology has been gathered by conducting conventional second messenger based assays, making these assays an essential tool in GPCR pharmacology. These methods are neither universal nor ideal because only in rare cases these assays are performed with native cells reflecting the in vivo situation. Experimental manipulations of cells used in these assays range from addition of indicators to complex genetic modifications, respective expression of receptors, effector proteins and gene reporters [6]. For uncovering complex signalling pathways these reductionist approaches, focusing on an specific pathway are not usable for uncovering an overall cellular response [52], furthermore they are of limited use in de-orphanizing orphan receptors or their ligands. Label-free assay techniques are a possibility to overcome these problems. Label-free assays are non-invasive, holistic and provide a time resolved cellular response.

1.3 Label-free Whole Cell Biosensors

The common way for label free biosensors to convert the cellular response to a given stimulus into a quantifiable signal is the general use of transducers. There are different types of transducers depending on the physicochemical principle used for detection: electrical

(impedimetric, amperometric and potentiometric), optical, thermometric, piezoelectric and magnetic transduction [53]. The change at a sensor surface might be triggered by any kind of molecular interaction or a complex biological reaction. Enzymes, antibodies/antigens, nucleic acids, DNA strands, cell organelles, microorganisms, eukaryotic cells or tissues can build up the biological recognition unit of biosensors. Label free assays use biosensors to record a ligand-induced effects in a non-invasive mode and without adding any chemical labels or additives [54, 55]. The principal of operation within a cell-based biosensor is to convert a vast number of cellular effects (cell shape changes, cell adhesion / proliferation / death) into an exploitable signal [56-59]. The signal is a holistic answer of the cell layer including: cytoskeletal rearrangements, cell-cell interactions and cell volume change. The outcome of the label-free assay is commonly called a “black box” readout, as it is challenging to interpret the holistic answer of the sensor with respect to the contributing pathways of the selected cell system [60]. In comparison to traditional label-based assay formats, label-free technologies do not depend on an a priori knowledge of the involved pathway as the readout is integral and not specific for any of the signalling routes. [61]. Label-free technologies are usable for any GPCR, even orphans, if the receptor of choice is expressed in an suitable cell type [62]. Label-free assays quantify integral changes of the cells, more than having the possibility for resolving the pathway of the overall response with molecular specificity. These technology format increases the possibility to identify involved biological compounds that are not detectable in label dependent assays [40]. Dependent on the physical principle used for signal transduction label-free biosensors are grouped into explicit groups, as described in literature [53].

1.3.1 Electric Cell Substrate Impedance Sensing (ECIS)

Electric Cell Substrate Impedance Sensing (ECIS) is a technique, which enables a non-invasive, time resolved and label-free observation of changes in morphology of adherent cells in vitro. For the first time this technique was described in 1984, and later classified as a “morphological biosensor for mammalian cells” [63, 64]. This biosensor consists of a working electrode (WE) and a counter electrode (CE) which is 100 – 1000 times larger than the WE. Both are deposited as thin film electrodes on the bottom of a cell culture dish. AC impedance of the two electrodes immersed in culture fluid is the physical parameter to measure. The measured impedance is dominated by the WE, as the voltage drop and current density at the CE can be disregarded because of the size difference. Adherent cells behave essentially like an insulator due to the non-conductive properties of the cell membranes and thereby increase the electrode impedance when present on the electrode surface. The cell culture medium above the cell layer is a highly conductive salt solution. When a small sinusoidal alternating

current is applied (AC), the corresponding voltage drop in the system is studied as a function of frequency so that the impedance of the system is calculated according to Ohm's law. There are two principal pathways for the applied current to cross the insulating cell layer. At frequencies below 10 kHz the preferred pathway is around the cell body, while at frequency's above 10 kHz capacitive coupling through the cell membrane becomes the main pathway [65]. Frequency-dependent impedance data can be split into three theoretical parameters with the help of a physical model that is referred to as the ECIS model. In this model R_b describes the impedance contributed by specific resistance of the cell-cell junctions. C_m represents the average capacitance of the cell membranes, but it is noteworthy that it is not possible to distinguish between the upper and lower membrane of the cell. The third parameter α, depending on the cell-electrode distance and the cell radius, describes the impedance due to current flow between electrode surface and cells [59, 66]. Applying this model, overall and integral impedance changes are attributed to individual parts of the cell body.

The ECIS readout is multi-modal and allows studying a variety of cell phenotypes including cell viability, barrier function, cytotoxicity, cell migration, wound healing, drug efficacy and GPCR stimulation. They all have been successfully monitored using ECIS [64, 67-70].

1.3.2 Surface Plasmon Resonance (SPR)

Surface Plasmon Resonance (SPR) is an optical readout that can be applied for living animal cells as well as for complex biological systems and different immune assays [71]. SPR was first described in the late 1960s by Otto and Kretschmann [72, 73]. SPR is mostly used as a very sensitive reporter to characterize bimolecular interactions at the interface between analyte-containing bulk phase and sensor surface (usually gold). More recently is has been used to capture organisms like bacteria and to monitor reactions in biological systems like cells and tissues as well [74, 75]. The operating mode of SPR sensors is to measure shifts in the refractive index (RI) which occur at the interface of the sensor surface. The sensitivity of the device for RI changes is characterized by $\Delta n/n = 10^{-7}$ [76]. The phenomenon of surface plasmon resonance takes place when a monochromatic light beam hits the interface between a thin layer of metal (silver or gold) and the environment under conditions of total internal reflection. Propagating light consist of a transverse electric field (TE or s-polarized light) and transverse magnetic field (TM or p-polarized). Surface plasmon resonance takes place when p-polarized light hits the surface while s-polarized light increases just the background intensity of reflected light and does not cause plasmon resonance. In addition several instrumental configurations exist to excite surface plasmons, like prisms, grating or optical waveguides [71, 77]. At resonance, at which a maximum fraction of light is coupled into the surface, an

evanescent field and plasmons are excited. Level of plasmon generation depends on the wavelength and angle of incidence as well as on the refractive index of the prism (waveguide/ grating structure), the metal film and the neighbouring medium. Resonance is manifested as minimum in the intensity of the reflected light (reflectance). Thus, when all parameters of the system are kept constant and the device is illuminated with monochromatic light at different angles (angle scan), an RI change of the micro-environment close to the metal layer (200 nm) can be measured by a shift of the angle of minimal reflectance.

1.3.3 Dual ECIS-SPR Sensor Platform

The label-free techniques ECIS and SPR, as described above, show advantages and limitations of their specific capabilities to solve certain problems. As described before ECIS is able to measure changes in morphology and dynamics of cell layers attached to the substrate surface non-invasively and sensitively, including the weakening of cell-cell or cell-substrate contacts, caused by internal or external stimuli. Reactions that do not go along with changes in morphology or weakening/tightening of the cell-cell or cell-substrate contacts are not measureable with this impedance-based technique. SPR is an evanescent field based technique which measures the changes in refractive index close to the substrate surface. The evanescent field penetrates only in the lower part of the cell layer. SPR is not able to detect changes, which occur outside of the evanescent field like cell-cell interaction via tight junction proteins. The ECIS and SPR technique are the most widespread label-free techniques on the market and subsequently the next step is to combine these two readouts on one substrate for recording the cellular response with both measurement principles for the same cell population [78]. The two techniques are based on different physical principles. The ECIS (electrical) readout provides data integrated over the entire cell body while the SPR readout (optical) detects difference on the refractive index close to the substrate surface (200 nm). The readout of one cell population with two different readout techniques could yield complementary data obtained from the same cell layer [78].

1.3.4 Dynamic Mass Redistribution (DMR)

Dynamic mass redistribution (DMR) within adherent cells can be recorded by an optical sensor such as a resonant waveguide grating (RWG). RWG is used since the 1990s and was originally used for investigations to monitor binding events at the solid-liquid-interphase [79]. The sensor consists of a substrate layer, a waveguide film wherein an optical grating structure

is embedded, a medium and a cell layer [80]. By illumination from the bottom of the microplate with broadband light centred at 830 nm in a specific angle, the light moves in parallel through the bottom of each well of the microtiter plate [81]. As a result from the interaction of the light and the grating a evanescent field occurs which decays exponentially from the sensor surface [56]. The electromagnetic field interacts with the cell layer close to the sensor surface and is transmitted only for the resonant wavelength. The latter depends on the local refractive index in the sample so that subtle changes in the cell layer induce a change in the reflected wavelength. The readout records the shift of the resonant wavelength in pico meter (pm) as a function of time [82]. GPCR-agonist induced cellular response leads to changes in the refractive index close to the surface which causes a shift in the resonant wavelength (pm) [83]. Mass redistribution towards the sensor surface is detectable as signal increase, when mass is moved to the surface while a signal decrease occurs when mass moves away from the surface. Mass movement parallel to the surface is not detectable [56]. Similar to SPR, the penetration depth of the RWG evanescent field is about 200 nm, thus DMR only records changes within this distance from the surface. Concluding the optical RWG method can be considered as another non-invasive and label-free technique to monitor cell-based assays [82, 84]. Fig. 1-2 shows schematic the principle of resonant waveguide grating

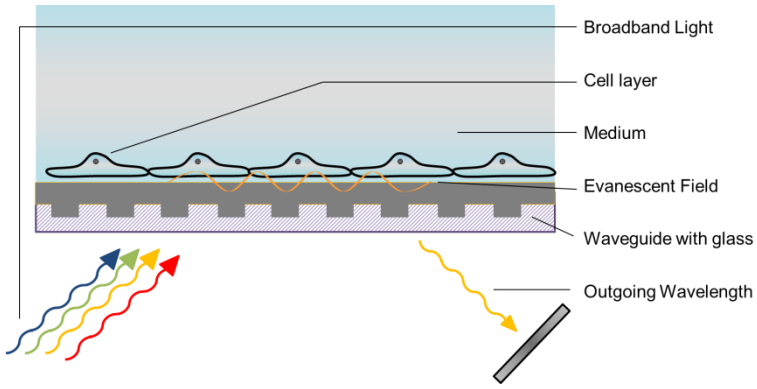

Fig. 1-2 Schematic representation of a resonant waveguide grating system for the excitation of an evanescent measurement field. The substrate consists of a waveguide on a glass substrate. The evanescent field is not drawn to scale.

2 Scope and Objectives

As shown in the introduction, ECIS and SPR are two high-performance tools for label-free, non-invasive, time-resolved wholistic monitoring of cell-based assays that have developed independently. The two techniques provide complimentary information's. Label-free readouts themselves can be described as "black box" readouts and return complementary results to the canonical assays. The commonalty of ECIS and SPR is the integral time resolved recording of the cell response, but they don't provide specific molecular informations. Interpretation of the signal patterns is therefore difficult. It is the idea and the scope of this thesis to combine the two methods in one platform and establish a dual ECIS-SPR sensor. Thereby information from both readouts is recorded in one experiment from the identical cell layer. The data provided by the dual sensor platform provides a stronger basis for data analysis and interpretation. The successful development requires extensive work on the sensor chip, cell culture conditions, liquid handling and data analysis. The dual ECIS-SPR sensor setup promises to assist in deconvolution of the time resolved wholistic signal patterns after GPCR stimulation. Thereby the availability of simultaneously recorded data from both readout methods should provide additional benefit. For support and better data understanding theoretical simulations will be performed for animal cells adhered on a sensor chip for both measuring methods. Simulation experiments will be performed for a better comprehension of the individual signal patterns. To substantiate the experiments of this thesis, they will be complemented by time course data recorded with commercially available ECIS and DMR devices. The dual ECIS-SPR setup will serve as sensor to monitor GPCR receptor stimulation. The first cell line of choice is the U-373 MG cell expressing the human histamine-1 receptor $_{h}H_1$ activating the $G_{\alpha i/11}$ signal pathway. This well investigated cell line is the main model system for the development of a reliable ECIS-SPR assay format and the necessary sensor chip. The second cell line used in this thesis is the CHO parental cell line genetically engineered to express the dopamine D_2 receptor which activates the $G_{i\alpha}$ signal transduction pathway. The CHO cells are available with two receptor isoforms of the D_2 receptor family, D_2S (short) and D_2L (long). The well understood signal transduction pathway for both cell lines allows applying specific pharmaceutical tools to block or modulate precisely the internal signal. These pharmaceutical tools will be used to influence artificially the signal transductions of the stimulated cell lines with their specific G-protein coupled receptors. It is the objective of this thesis to establish a new ECIS-SPR sensor platform to monitor cell-based assays, capable of distinguishing different GPCR stimulation patterns by recording fingerprint like signal patterns with both readout approaches that might help to deconvolute the signalling pathways for unknown agonists or receptors in the future..

3 Material and Methods

3.1 Cell culture

3.1.1 Cell lines

Experiments in this thesis were performed with the cell lines listed below. Astrocytic U-373 MG (human glioblastoma cell line), the epithelial cell line MDCK-II (Madin Darby canine kidney, strain II) and CHO cells stably expressing the dopamine receptor D2 in a short and long isoform. Prof. Buschauer (University of Regensburg, Germany) provided U-373 MG cells. MDCK-II cells were obtained from the DSMZ (Deutsche Sammlung von Mikroorganismen und Zellkulturen), whereas CHO D2 L/S were kindly provided by Prof. Gmeiner (University of Erlangen, Germany). Information about the cell lines used in this thesis is listed in Tab. 3-1.

Table 3-1 Cell lines used in this thesis

Cell line	origin	morphology	literature	supplier
U-373 MG	human glioblastoma cell line	polymorphic/ astrocytic	Bigener et. al. 1981	Prof. Buschauer
MDCK-II	canine kidney	epithelial	Richardson et. al. 1981, Balcarova-Staender et. al. 1984	DSMZ, Germany
CHO D2 Long CHO D2 Short	chinese hamster ovary	epithelial-like	Hayes et. al. 1992	Prof. Gmeiner

3.1.2 General cell culture conditions

The general culture work was performed under sterile conditions using a laminar flow hood (Thermo Fischer Scientific Inc., Waltham, USA). Buffers, media and other solutions were routinely autoclaved (20 min, 120 °C) or have been passed through a sterile filter with a pore diameter of 0.2 µm (TPP®, Sigma Aldrich, Munich, Germany). All cell lines were cultured on the bottom of sterile culture flasks with a growth area of 25 cm² (Greiner, Kremsmünster, Austria) and kept in cell culture incubators (Thermo Fischer Scientific Inc., Waltham, USA) at 37 °C in a humidified atmosphere supplemented with 5 % CO_2. Cell culture medium (Tab. 3-2) was exchanged every third day.

Table 3-2 Cell culture media composition

medium	composition
U-373 MG culture medium	Minimum Essential Medium Eagle (MEM) incl. 1g/L glucose 5 % (v/v) fetal bovine serum (FBS) 100 µg/mL penicillin 100 µg/mL streptomycin 2 mM L-glutamine
MDCK-II culture medium	MEM-Eagle incl. 1g/L glucose 5 % (v/v) (FBS) 100 µg/mL penicillin 100 µg/mL streptomycin 4 mM L-glutamine
CHO D2 Long/Short	Dulbecco´s Modified Eagle's Medium / Nutrient F-12 Ham (DMEM) 10 % (v/v) FBS 100 µg/ml penicillin 100 µg/mL streptomycin 500 µg/mL $NaHCO_3$ 0.8 µg/mL Geniticin G-418

3.1.3 Sub-cultivation

All cell lines were subcultured once a week. A standard protocol was used to transfer the cells into new flasks after they reached 90 % confluence (Tab. 3-3, Tab 3-4). All buffer solutions and required media were pre-warmed to 37 °C in a water bath (Julabo, type TW 12, Seelbach, Germany). Cells were washed with phosphate buffered saline solution without calcium and magnesium ions (PBS --, Sigma Aldrich, Munich, Germany). Subsequently, cells were incubated with EDTA solution (ethylene-diamin-tetraacetic acid, Merck KGaA, Darmstadt, Germany) at 37 °C followed by an enzymatic digestion with trypsin (Sigma Aldrich, Munich, Germany). Enzymatic activity was stopped by addition of culture medium (10-fold excess). Suspended cells were transferred into a centrifugation tube (Cellstar® centrifuge tubes, Greiner Bio-one, Kremsmünster, Austria) and spun down at 110 x g for 10 min at room temperature (RT) (Heraeus 1-SR, Thermo Fischer Scientific Inc., Waltham, USA). The supernatant was

discarded and the cell pellet was resuspended in fresh culture medium. Cells were diluted and seeded into new culture flasks.

Table 3-3 Incubation times at 37 °C for individual sub-cultivation steps for each cell line under study.

Cell line	**PBS $^{--}$**	**EDTA**	**trypsin**
U-373 MG	1 x wash	-	2 – 3 min
MDCK-II	3 x 5 min	2 x 10 min	10 – 15 min
CHO D2 Long/Short	1 x wash	-	2 – 3 min

Table 3-4 Composition of buffers used for sub-cultivation

buffer / solution	composition
Dulbecco's Phosphate Buffered Saline (PBS--)	0.2 g/L KCl 0.2 g/L KH_2PO_4 8.0 g/L NaCl 1.15 g/L Na_2HPO_4
EDTA solution Trypsin/EDTA solution	1 mM EDTA in PBS^{--} 0.025 % (w/v) trypsin in 1mM EDTA solution (0.25 % (w/v) trypsin (for MDCK-II) 1mM EDTA solution

3.1.4 Cell Preparation for Experiments

By default, cells were fed the day before they were seeded on the different sensor devices (ECIS electrode array or SPR-chip) with fresh culture medium. This is necessary to remove dead cells, to maintain a consistent viability and to standardize metabolic activity of the cell layer for the assay. The suspended cells were seeded on the different sensor devices for an experiment after removing them from the culture flask, following the standard protocol of sub-cultivation (3.1.3). In order to ensure aseptic conditions for cell experiments, the growth substrates were sterilized with an argon plasma treatment for 30 sec (Plasma cleaner, Harrick Plasma Inc., Ithaca, USA). For better reproducibility, the cells were seeded upon the sensors with a defined cell number per unit area. Therefore the cells, after resuspension of the cell pellet, were counted with a hemocytometer (Bürker, Marienfeld-Superior, Lauda Königshofen, Germany). The cell suspension was then appropriately diluted to the desired cell density (Tab. 3.5) with culture medium before seeding. The day after seeding the cells were fed with culture medium again and at the day of the experiments (2 h before), they were incubated with the CO_2 independent medium L-15 (Leibovitz, Sigma Aldrich, Munich, Germany) that was used as experimental buffer in all experiments.

Table 3-5 Area specific seeding density of the cell lines to provide confluent cell layers on sensor devices.

Cell line	**Seeding density**
U-373 MG	120.000 cells/cm²
MDCK-II	450.000 cells/cm²
CHO D2 Long/Short	120.000 cells/cm²

Chemicals for investigations on G protein-coupled receptors (GPCRs) were always directly prepared before use and diluted in L 15 media.

Table 3-6 Chemicals and drugs used for GPCR investigations in this thesis

substance	formula	classification	supplier
BAPTA AM	$C_{34}H_{40}N_2O_{18}$	Calcium chelator	BIOMOL GmbH, Hamburg, Germany
Calcimycin (A 23187)	$C_{29}H_{37}N_3O_6$	Calcium ionophor	Sigma Aldrich, München, Germany
1,2-Dioctanoyl-*sn*-glycerol	$C_{19}H_{36}O_5$	activator of protein kinase C	Merck KGaA, Darmstadt, Germany
dopamine hydrochloride	$C_8H_{11}NO_2$ •HCl	endogenous D_2-receptor agonist	Sigma Aldrich, München, Germany
haloperidol	$C_{21}H_{23}ClFNO_2$	neuroleptic	TCI, Deutschland GmbH, Eschborn
forskolin	$C_{22}H_{34}O_7$	stimulator of adenylate cyclase	Sigma Aldrich, München, Germany
histamine dihydrochloride	$C_5H_9N_3$ •2HCl	endogenous H_1-receptor agonist	Carl Roth, Karlsruhe, Germany
Pluronic® F-127	-	detergent	Sigma Aldrich, München, Germany
quinpirole hydrochloride	$C_{13}H_{21}N_3$ •HCl	synthetic D_2-receptor agonist	Sigma Aldrich, München, Germany
sulfinpyrazone	$C_{23}H_{20}N_2O_3S$	inhibitor of organic anion transporter	Sigma Aldrich, München, Germany
UR-KUM 530	$C_{16}H_{18}N_5Br$	synthetic H1-receptor agonist	Prof. Buschauer, University Regensburg, Germany [85]

3.1.5 Cell Storage

Cell lines were deep-frozen in a cryogenic tank in order to store the cell line for a longer period. For this, a confluent cell layer on a flask was treated the same way as for sub-cultivation. After centrifugation the cell pellet was re-suspended in a special freezing-medium. For the U373-MG and MDCK-II cell lines the freezing-media consisted of 90 % FBS (sigma Aldrich, Munich, Germany) and 10 % (v/v) DMSO (Dimethyl sulfoxide, Carl Roth, Karlsruhe, Germany). CHO D2 Long/Short were frozen in 70 % standard culture medium, 20 % (v/v) FBS and 10 % (v/v) DMSO. The cell suspension was then transferred into cryovials (TPP®, Sigma Aldrich, Munich, Germany) and cooled to – 70 °C using a isopropanol bath (Nalgene® CyoBox™, Sigma Aldrich, Munich, Germany). This first part of slow cooling (1 °C/min) was followed by a final transfer into a liquid nitrogen tank (German Cryo GC-BR2150 M, german-cryo® GmbH, Jüchen, Germany) for the long term storage. For recultivation of the frozen cells, the cryovials were removed from the liquid nitrogen tank and then kept for 1 h at -20 °C. Subsequently, the cryovials containing the cells were thawed using a 37 °C warm water bath (Julabo, type TW 12, Seelbach, Germany). The cells suspension was transferred into a centrifugation tube and diluted by a dropwise addition of 10 mL pre-warmed culture medium. After centrifugation (110 x g, 10 min at RT) the cell pellet was re-suspended in standard culture medium. Cells were seeded in culture flasks at different ratios with respect to their former growth area. 24 h after cell thawing, the culture medium was exchanged. Cells kept under general culture conditions according to Chapter 3.1.2.

3.2 Electric Cell-Substrate Impedance Sensing (ECIS)

Electric Cell-Substrate Impedance Sensing (short: ECIS) is the name for an electrochemical method which allows monitoring the behaviour of adherent cells when grown on gold-film electrodes by measuring the electrode's' impedance depending on the used AC frequency. Changes in morphology in the cell layer can be monitored with a high temporal resolution non-invasively and quantitatively. Planar gold film electrodes are the sensor surface, which is used at the same time as growth substrate. The measuring setup contains two electrodes, the working electrode and the counter electrode which are conductively connected via the culture medium (Fig. 3-1). The basic idea of the method is based on the application of a sinusoidal alternating voltage of low amplitude along a range of discrete frequencies [66]. Measurement of the current allows the determination of the impedance as a function of the AC frequency. As a result of different sizes of working and counter electrode the impedance is predominantly determined through the small working electrode and the cells growing on its surface. For most

frequencies the cells act like isolating, nonconductive particles that force the current to flow around the cells. As a result of this behaviour the impedance of a cell covered electrode compared to a cell free electrode is higher. Cells change their morphology due to external stimuli or changes in their environment which causes changes the current pathways around the cell bodies and results in a change in impedance. Consequently impedance measurements are suitable to detect changes in cell morphology with a high time resolution.

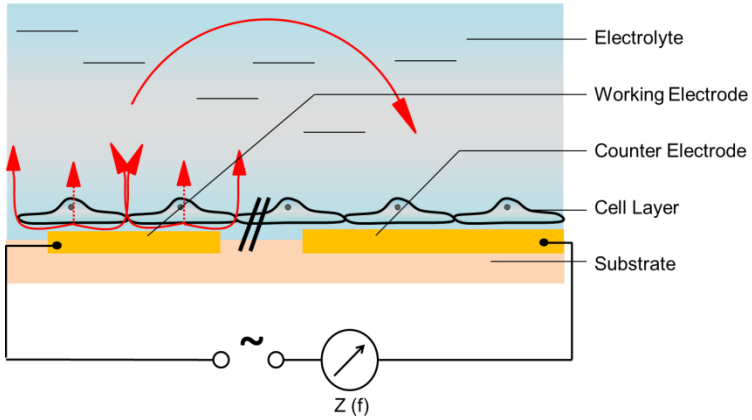

Fig. 3-1: Schematic drawing of the ECIS measurement principle. A small working electrode (WE) and a big counter electrode (CE) (CE > 100 fold bigger than WE), both made from thin gold-films, are used as transducers to monitor cell behavior. Low frequency current flows on paracellular pathways beneath and between the cells and through tight junctions, whereas high frequency current passes the cells on the transcellular pathway. The working electrode and the counter electrode are conductively connected via the culture medium.

Frequency dependent impedance measurements in combination with data modelling are used to distinguish between the impedance contribution of cell-cell contacts and cell-substrate contacts. The technique uses low amplitude signals to keep the influence on the cell layer as small as possible. In AC circuits it is beneficial to describe voltage, current and resulting impedance in complex numbers. For an AC voltage *U(t)* with a frequency ω:

$$U(t) = U_0 \cdot e^{i \cdot t \cdot \omega} \qquad \text{(Eq. 1)}$$

with the voltage amplitude U_0, the angular frequency $\omega(=2\pi f)$, the time t and $i = \sqrt{-1}$. For the resulting current the complex notation is:

$$I(t) = I_0 \cdot e^{i \cdot (\omega \cdot t - \varphi)} \qquad \text{(Eq. 2)}$$

I(t) is the actual value of the current, I_0 is the current amplitude. The phase shift between voltage *U(t)* and current I(t) is represented by the phase angle φ. The impedance Z corresponds to the ratio of voltage and current from which results:

$$Z = \frac{U_0}{I_0} \cdot e^{i \cdot \varphi} = |Z| \cdot e^{i \cdot \varphi} \qquad \text{(Eq. 3)}$$

The presentation of the complex impedance in the cartesian coordinate system is shown in figure 3-2. with the real part of the impedance denoted as Z´ and the imaginary part as Z``.

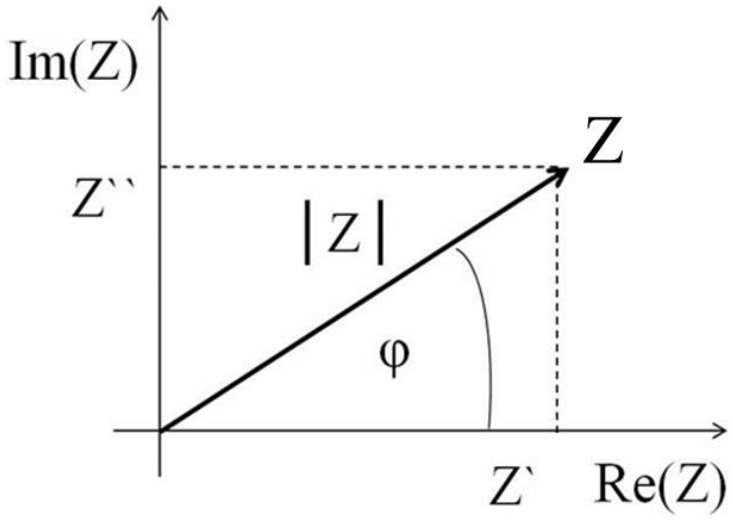

Fig. 3-2: The figure shows the impedance Z in the complex Gaussian plane. The x-axis is the real part of the complex impedance Re(Z), whereas the ordinate displays the imaginary part Im (Z). Z can be described in polar coordinates by the vector length IZI (impedance magnitude) and the angle φ (phase shift between voltage and current)

Shown in Gaussian plane the vector Z of impedance corresponds to the complex value:

$$Z = Z' + i \cdot Z`` \qquad \text{(Eq. 4)}$$

Accordingly,

$$Z` = |Z| \cdot \cos\varphi \qquad \text{(Eq. 5)}$$

and

$$Z`` = |Z| \cdot \sin\varphi \qquad \text{(Eq. 6)}$$

The length of the vector corresponds to the magnitude of the impedance IZI and the phase shift φ is the angel between the vector and the real axis Re (Z).

The magnitude of the impedance IZI and the phase shift φ are calculated from Z' and Z'' by the following equations:

$$|Z| = \sqrt{Z`^2 + Z`^2} \qquad \text{(Eq. 7)}$$

$$\varphi = arctan\ \frac{Z``}{Z`} \qquad \text{(Eq. 8)}$$

3.3 Surface Plasmon Resonance (SPR)

Surface plasmon resonance spectroscopy (SPR) is a label-free, time resolved surface sensitive method. The SPR can be used for investigations on cellular processes in particular morphological changes in adherent cell monolayers [74, 86]. The principle of the SPR is based on two physical phenomena: (i) total internal reflection (TIR) and the (ii) generation of surface plasmons at metal surfaces [87]. TIR occurs when light travels from a medium with a high refractive index η_p (e.g. prism) across the interface to a media with a low refractive index η_d (e.g. water). When a certain angle (critical angle, θ_c) is exceeded, total internal reflection into the media with the higher refractive index η_p is observed. The Snellius's law describes the critical angle θ_c:

$$\theta_c = \arcsin\left(\frac{n_d}{n_p}\right) \qquad \text{(Eq. 9)}$$

The total reflected beam does not lose any of its energy but the electric field of the photons extends across the interface into the medium with the lower refractive index. Consequently, there is no immediate sharp boundary for the electromagnetic field behind the interface but an evanescent field reaches into the medium of lower refractive index. The amplitude of the evanescent field decreases exponentially with increasing distance to the interface. It depends on the refractive index η_d of the medium with the lower optical density and on the wavelength of the incident light beam. The wave vector (k_{ev}) of the evanescent field is:

$$k_{ev} = \frac{\omega}{c} \cdot n_p \cdot \sin\theta \qquad \text{(Eq. 10)}$$

in which ω denotes the angular frequency of the incoming light, c is the speed of light, η_p is the refractive index of the prism and θ the angle of incidence. When the prism is coated with a thin metal layer (e.g. gold), there is an interaction of the evanescent field with the free electrons of the metal. At a certain angle of incidence at the interface between the prism and the gold surface, the photons couple with the electrons of the metal and produce electron density fluctuation, the so called surface plasmons. Due to the oscillation of the free electrons, which create an electromagnetic field, the reflected light is attenuated in its intensity.

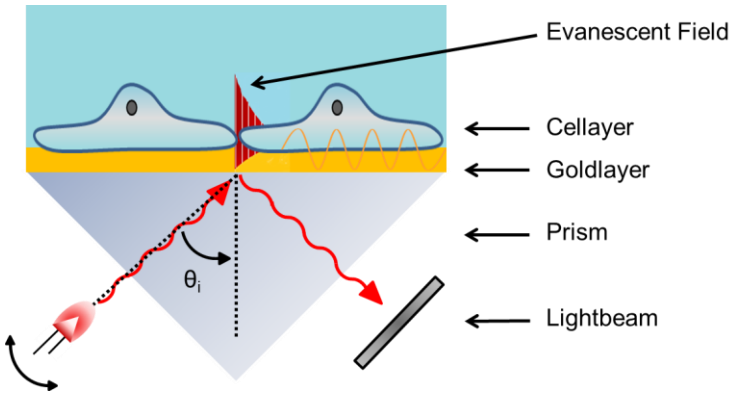

Fig. 3-3: Schematic representation of a prism coupling system for the excitation of an evanescent measurement field. On top of the prism is a gold film with adherent cells on the surface. The evanescent field is not drawn to scale.

For resonance and the generation of plasmons to occur, magnitude and direction of the wave vectors of the photons and plasmons have to match. The magnitude of the wave vector k_{SPR} of the surface plasmons is:

$$k_{SPR} = \frac{\omega}{c} \cdot \sqrt{\frac{\varepsilon_M \cdot n_d^2}{\varepsilon_M + n_d^2}} \qquad \text{(Eq. 11)}$$

With the refractive index of the dielectric (n_d) $n^2_d = \varepsilon_d \cdot \mu_d$ in which the permeability μ_d is 1 for transparent media and ε_M is the permittivity of the metal.

This match of wave vectors is achieved by p-polarized light. The generated surface plasmons can migrate along both sides of the metal surface. Thereby the wave gets in contact to the media adjacent to the metal film with a smaller optical density η_d (e.g. water). The length of the plasmon wave vector corresponds to the evanescent field wave vector. The excitation maximum of the SPR that corresponds with an intensity minimum of the surface reflected light, also given as reflectivity of the metal layer, is reached when the light incises with the angle θ_{SPR}. The surface plasmon reaches maximum intensity when the wave vectors k_{SPR} and k_{ev} are are identical. This is obvious from the minimization of the reflected light at the interface (Fig. 3-4)

$$k_{SPR} = k_{ev} \qquad \text{(Eq. 12)}$$

Accordingly, the resonant angle of incidence θ_{SPR} is given by eq. (13):

$$\theta_{SPR} = \arcsin\left(\frac{1}{n_p}\sqrt{\frac{\varepsilon_M \cdot n_d^2}{\varepsilon_M + n_d^2}}\right) \qquad \text{(Eq. 13)}$$

In this equation η_d is the refractive index of the adjacent media with the smaller optical density and ε_M is the permittivity of the metal.

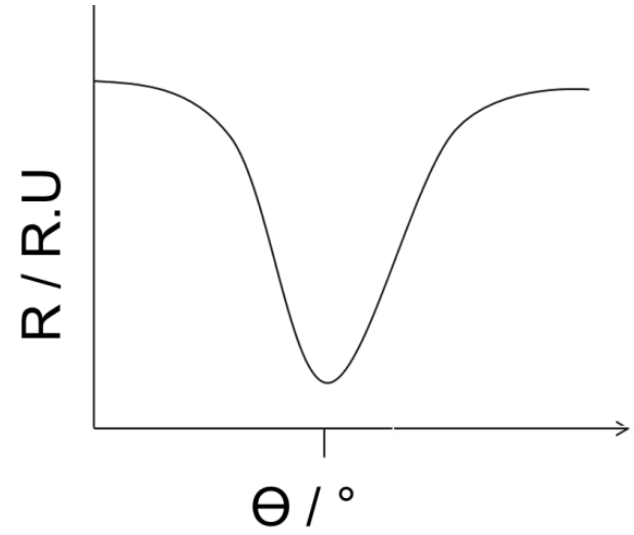

Fig. 3-4: Reflectivity R as a function of the angle of incidence Θ. The maximum intensity of the evanescent field/surface plasmons is reached at a minimum of reflectivity which corresponds to the resonant angle θ_{SPR}.

Eq. 13 shows, that the resonant angle θ_{SPR} reports on changes of the refractive index of the medium, which is in contact to the gold surface and is a direct measure for all changes occurring at the interface. The time resolved change of the minimum angle is a so called sensogram. There are two different measurement options available. The first possibility is to measure the reflectivity (R) at a constant angle θ_i. In this case the angle θ_i is fixed at the half maximum of the reflectivity R (kinetic mode). Changes of the intensity in reflected light get recorded and plotted as reflectivity (R) time profiles (Fig. 3-5 A). The second possibility is the measurement of the resonant angle of incidence $\theta_{SPR,}$ i.e. recording continuous angle scans to determine the resonant angle θ_{SPR} from these measurements (angle mode) (Fig. 3-5 B).

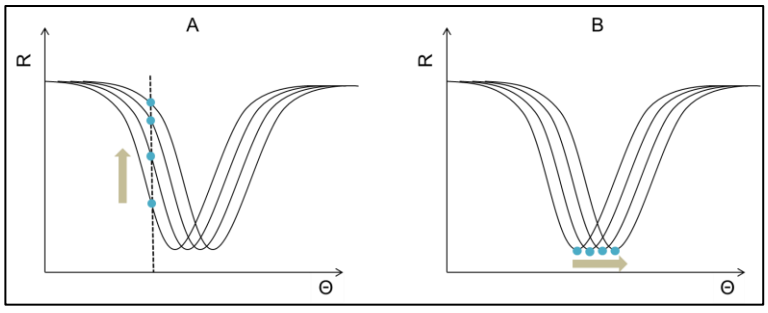

Fig. 3-5: Illustration of the two SPR measurement principles. **(A)** Kinetic measurement mode; the angle is fixed to a value where the negative slope is the biggest. Changes of the intensity in reflected light can be recorded over time with high time resolution. **(B)** Angle scan mode; R(Θ) spectra get recorded and the shift of the resonant angle (Θ_{SPR}) is followed as a function of time.

3.4 Experimental setup

The experimental setup to for the dual ECIS-SPR sensor experiments and the experimental procedures are described below.

3.4.1 Setup of the SPR measuring device

All SPR experiments were performed on the surface plasmon resonance spectrometer Biosuplar 400T (Mivitec GmbH). The system is built up in the Kretschmann configuration and has a laser diode as light source (Wavelength 630-670 nm). In this system the incident light is split into two beams. Both get p-polarized and are then guided to a glass prism (η_p = 1.62). The prism has a metallized back so the reflected light hits the sensor surface and is then guided to the detector inside the spectrometer. The entire setup is placed in an incubator at 37°C (Orbital Incubator SI50, Stuart). The device is controlled by the Biosuplar 400T software (Mivitec GmbH) provided by the manufacturer.

3.4.2 Setup of the ECIS measuring device

For a time-resolved impedimetric monitoring of the same cell population in parallel to an SPR-based cell analysis, a special layout of the sensor chips was designed and prepared (cf. fig. 3-6). The two working electrodes (WE) and the counter electrode (CE) on the sensor chip were electrically connected to an impedance analyser (Fig. 3-6). A relay allowed switching between the two working electrodes.

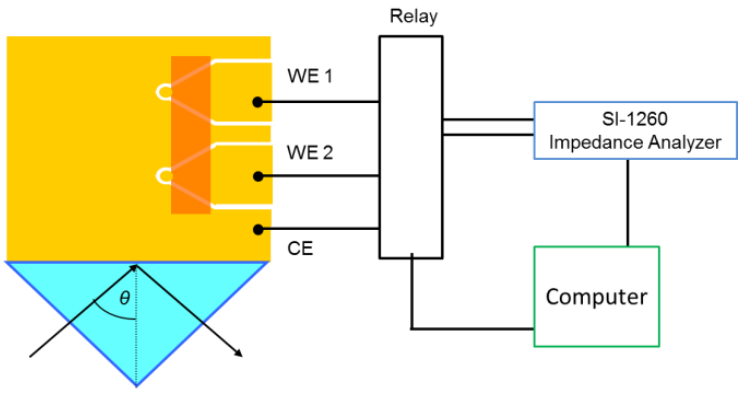

Fig. 3-6. Experimental setup of the ECIS readout on the dual ECIS-SPR sensor. The sensor chip is placed on a prism with the laser beam coupled into the gold surface for SPR recording. For ECIS recordings the electrodes, working electrode (WE) and the bigger counter electrode (CE), are connected to an impedance analyzer with a computer controlled relay switch, which allows the readout of the two different working electrodes.

Relay and impedance analyser were controlled by an ordinary computer. For acquiring impedance data, the continuous wave impedance analyser (Solatron Instruments-1260, Farnborough, UK) applied a non-invasive AC voltage of 30 mV to a working electrode/counter electrode couple. Measurements were performed at 61 designated frequencies (1 Hz-1-MHz) equally spaced on a logarithmic scale. The associated current was measured phase-sensitively and provided the complex impedance of the system as function of frequency.

Preparation of the SPR and ECIS-SPR sensor surfaces

The reaction chamber (Fig. 3-7B) is prepared from PDMS (polydimethylsiloxane). A corresponding mould made from Teflon (Fig. 3-7A) is filled with a mixture of Elastomer (elastomer base) and hardener (curing agent) in proportion 10:1 (Sylgard®, Type 184). The mixture is allowed to dry for 24h at 60°C. The PDMS chamber and the sensor surface with the gold layout get cleaned in argon plasma (30 s, Plasma cleaner, Harric Plasma). After cleaning the PDMS spacer is mounted to the sensor surface with silicone glue (Master fix Aquarium Silikon, Warenimport und Handels GmbH, Vienna, Austria) followed by 24h of drying (cf. fig. 3-7C). The finished sensor chips get cleaned again in argon plasma as described. The reaction chamber gets filled with culture medium (100 µL), followed by seeding of the cells of interest into the reaction chamber with the desired density. While cultivating the cells to 100% confluency in an incubator (37°C, 5 % CO_2) the sensor chip is placed in a petri dish with a smaller petri dish as an additional water reservoir inside the first petri dish to avoid evaporation of culture medium (fig. 3-7D).

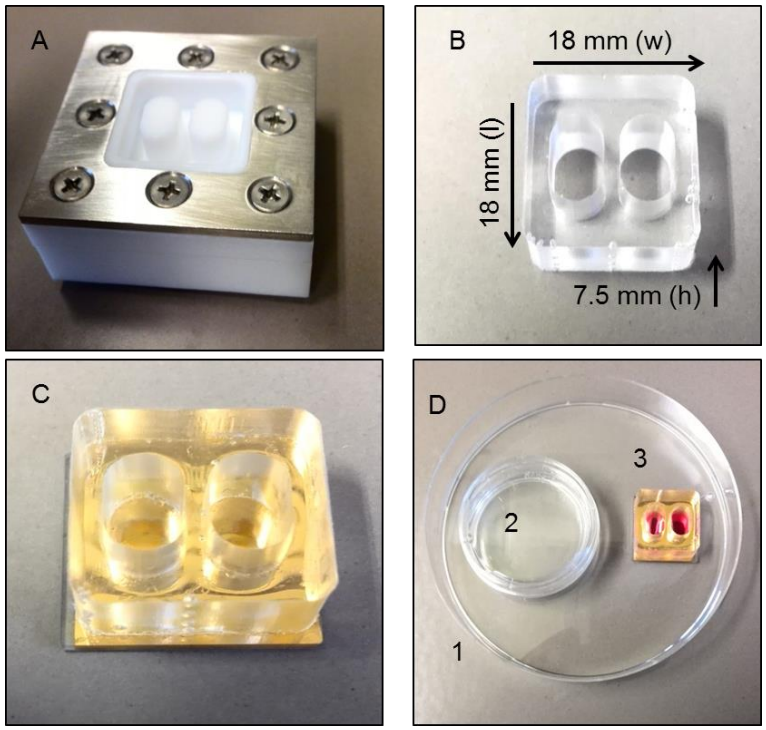

Fig. 3-7: (A) Teflon mould (size 40x40x12 mm) to shape the PDMS reaction chamber. **(B)** PDMS reaction chamber after drying and mounting to the gold surface to provide the final sensor device **(C)**. **(D)** Petri dish (1) with a small petri dish (2) filled with sterile water to keep humidity constant; the sensor chip (3) with filled chambers.

Experimental procedure

For the measurement it is necessary to provide an optical contact between the glass prism and the bottom side of the sensor surface. Therefore immersion oil (7.5 µL, Cargill $\eta_D^{25°C}$ = 1.61) is placed on the prism, which is pre-cleaned with ethanol and dried. The sensor chip gets cleaned on the bottom side with ethanol too and dried before placing on the prism. Finally, the lids for the reaction chamber are placed on the PDMS structure and are fixed with the locking pin.

3.4.3 Dual ECIS-SPR sensor measuring device

The dual sensor platform allows combining both techniques, ECIS and SPR, within one experimental setup. The ECIS-SPR chips were prepared of a high refractive index glass slides (2 cm x 2 cm) covered by a 5 nm chromium film followed by a 45 nm gold layer on the top. The metal layer was subsequently structured by photolithography followed by wet etching. The positive photoresist AZ ECI 3027 (MicroChemicals, Ulm Germany) was applied to the sensor surface by spin-coating at 300 rpm using the manual spin coater WS-400-6NPP-LITE (Laurel Technologies Corporation, North Wales, USA). The coated substrate was dried by a softbake

(30 min; 100 °C, heating oven type 500, Memmert, Schwabach, Germany) followed by exposure to UV light (2 min, isel® UV illumination device nr. 2, Elterfeld, Germany) through a corresponding layout mask which defined the UV-exposed areas for later lift-off. Gold was removed using an aqueous solution of KI (0.265 mmol/L) and I_2 (0.5 mmol/L) for 1 min. Finally, the substrate got washed with acetone to remove the remaining photoresist followed by a thoroughly wash with deionized water and eventually the substrates were dried at ambient conditions. To provide gold electrodes with well-defined surface areas and to prevent that other parts of the gold film contribute to the electrochemically active area, the contact paths were insulated with positive photoresist by adding a second spin-coating and photolithographic step using a different mask. Therefore, the adhesion promoter TI-Prime (MicroChemicals, Ulm, Germany) was spin-coated on the substrate surface before the photoresist was applied in order to improve resist adhesion after hard bake. On top of the finished sensor layout a PDMS spacer (Sylgard 184 silicone elastomer kit, Dow Corning, Michigan, USA) forming a cell culture compatible flow cell was glued on the top of the sensor using a nontoxic silicone adhesive (Master fix Aquarium Silikon, Warenimport und Handels GmbH, Vienna, Austria). The silicone glue was allowed to cure for 24 h. The resulting sensor surface (Fig. 3-8) featured two individually addressable small circular ECIS working electrodes (Ø = 1 mm) and one large counter electrode, which was used as an SPR readout field at the same time.

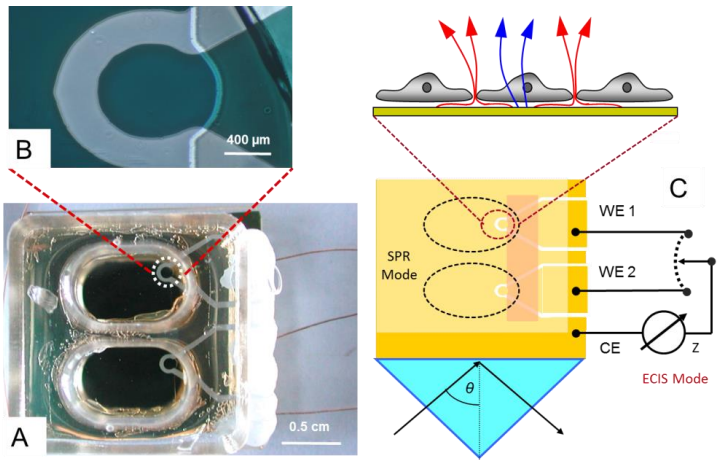

Fig. 3-8. (A) Photograph of the combined ECIS-SPR sensor surface with the wires connected to the hardware. **(B)** Magnification of a working electrode with an area of (0.64 mm^2). **(C)** Illustration of the sensor chip with the SPR detection area and the working electrodes for the ECIS measurement.

3.5 Dynamic mass redistribution (DMR)

The label-free readout which is referred to as dynamic mass redistribution (DMR) was conducted on an EnSpire multimode reader (PerkinElmer, Waltham, USA). This technique is based on the EPIC optical biosensor technology using resonance waveguides (RWG/DMR,

1.3.4). Prior to RWG-based assays, cells of interest were prepared in their individual culture medium from 90 % confluent cell layers by standard trypsinization. For the experiment cells were suspended in cell culture medium and seeded into uncoated 384-well EnSpire cell assay microplates. The standard volume to seed cells was 30 µL using a multichannel electronic finnpipette (Thermo Fisher Scientific, Waltham, MA, USA). The applied cell density was $1.5 \cdot 10^4$ cells / well. The microplates were incubated in a humidified atmosphere with 5% CO_2 at 37° for 24h providing confluent cell layers. Before the experiment, the cells were washed four times with L-15 medium and equilibrated for 1h in the multimode reader at 37° in L-15 medium. After baseline recording, 10 µL of the test substance dissolved in L-15 medium were added to the individual wells outside the reader using a multichannel finnpipette, afterwards the recording continued inside the reader. The time resolved data set is presented by a shift of the resonance wavelength Δ λ (t) relative to the last data point recorded before the test compound was added to the wells at time zero. Therefore, Δ λ (t) = λ (t) - λ (0). The time course patterns for all test compounds were subsequently corrected for the corresponding values of untreated controls (buffer only).

3.6 Dose-response analysis

The concentration response curves were constructed from the recorded time courses by measuring (1) the areas under the curve of individual response profiles [Δ IZI(t) or Δλ (t)] from 0-30 minutes or (2) The maximal value of the individual response profile [Δ I R_t - R_0 I or Δ IZI(t) or Δλ (t)], for each compound concentration. The concentration of half-maximum cell response EC_{50} was determined by fitting a four parameter sigmoidal transfer function (Eq. 14) to the recorded data using OriginPro 8 (OriginLab Corporation, Northampton, USA)

$$y = \frac{y_{min} - y_{max}}{1 + (x/x_0)^p} + y_{max} \qquad \text{(Eq. 14)}$$

Herein y denotes the signal response at a given concentration x, y_{max} is the maximal response and y_{min} the minimal response and x_0 marks the EC_{50} value with the Hill slope p.

4 Results and Discussion

4.1 Device development and Improvement

Monitoring cell-based assays with the help of SPR requires tailored technical solutions to exchange the incubation liquid inside the measurement chamber without inducing disturbances to the cell layer. This is particularly true for assays in which the cells respond rather quickly to the chemical stimulus. This situation applies to agonist/antagonist assays with G-protein coupled receptors. In the beginning of this thesis, a syringe pump (Model 540061, TSE System) was used for this purpose. The sensogram was recorded by the Biosuplar 400T software (Mivitech GmbH). The experimental work indicated that the use of the “flow” system was inappropriate to ensure reproducible results. Systematic analysis and test runs revealed that a manual exchange of the experimental buffer was the superior way of liquid handling and it ensures a complete mixing of the substance under test in the measurement chamber. Technically this concept required establishing of a measurement system with a fixed lid made of PMMA with two openings (Fig. 4-1). The lid was mechanically pressed to the top of the PDMS spacer above the sensor surface.

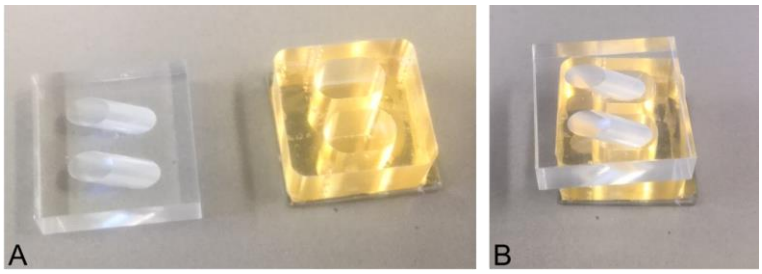

Fig. 4-1 A Lid made of PMMA with two openings on the top for liquid exchange. The lid was mechanically pressed to the PDMS spacer on the right. **B** Complete measurement chamber consisting of gold coated SPR chip, PDMS spacer and PMMA lid.

The cells were seeded and fed as previously described (3.1.4). On the day of the experiments the culture media was changed to phenol red free media (Leibovitz L-15). The measurement chamber (Fig. 4-1) was fixed in the SPR device and was equilibrated within the incubator for 60 minutes. The developed manual liquid handling system with a fixed lid and the addition of the reactive compound with a pipette led to a reproducible assay procedure (Fig. 4-2).

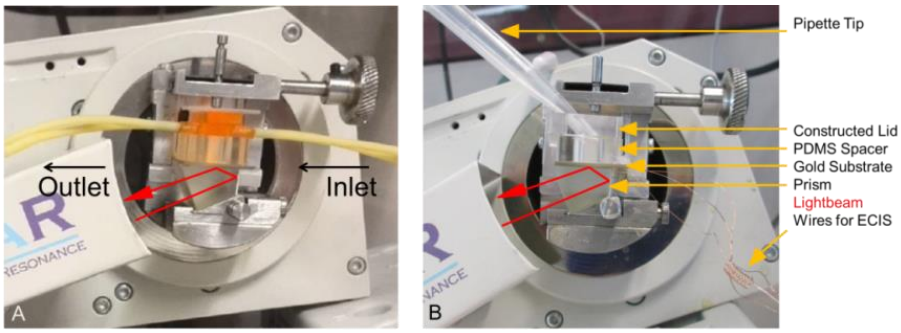

Fig. 4-2. Comparison of different liquid handling approaches used in this study. (A) Flow cell driven by syringe pump (not shown). The device provided irreproducible sensograms when experiments were repeated under exactly the same experimental conditions. (**B)** SPR setup prepared for manual liquid exchange by way of a regular pipette.

Fig. 4-3 shows confluent U-373 Mg cells exposed to 10 µM histamine at time zero using pump-controlled flow addition (A). The addition of the agonist (histamine) to the cell layer did not spread immediately and equally within the reaction chamber. The arrival of histamine with the flow of liquid at the cell surface seemed delayed and it was not possible to receive reproducible signal response. Repeating identical experiments returned highly variable signal patterns when a flow cell approach was used which were eventually considered not acceptable. Fig. 4-3 shows confluent U-373 MG cells exposed to10 µM histamine at time zero using manual liquid exchange (C). The agonist was added within a volume of 125 µL into the reaction chamber. The confluent cell layer is covered with 125 µL of cell media at the time of exposure. The addition of a double concentrated agonist solution to the cell layer provided permanently reproducible cell responses. Systematic analysis and test runs led to the development of a manual liquid exchange protocol. Reproducibility of the experiment with the new developed and established assay format provided significantly more reproducible signal patterns. Accordingly, all other experiments within this these were performed with a manual liquid exchange protocol.

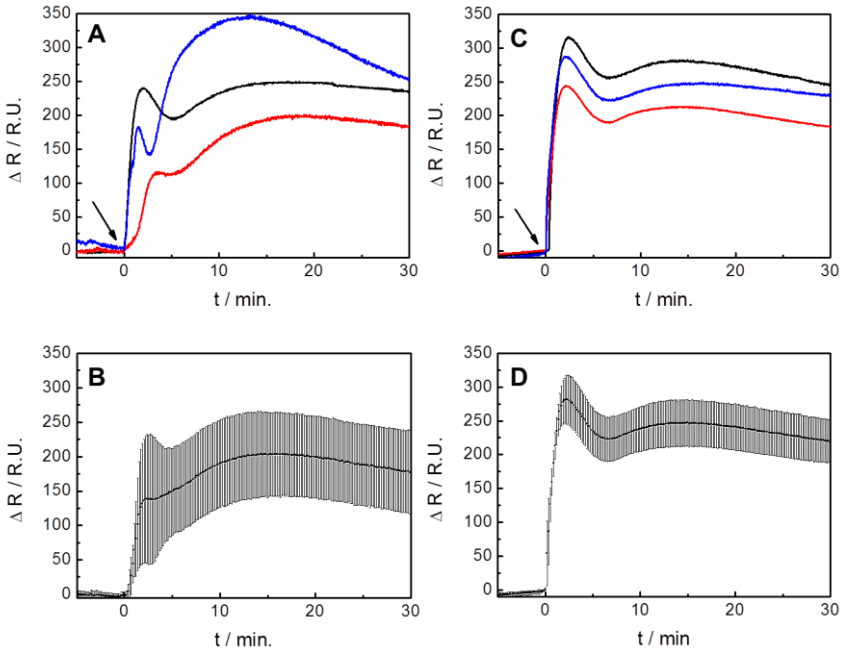

Fig. 4-3 Time course SPR data when confluent U373 cells, expressing the hH_1-receptor, are exposed to 10 µM histamine at time zero using either pump-controlled flow addition (A) or manual liquid exchange (C). The three curves show individual experiments that were repeated using identical experimental conditions. The average of the individual time courses in (A) is represented in (B), whereas the average of the time courses in (C) is shown in (D). Error bars are the standard deviation (SD) of three runs.

4.1.1 Discussion

In 2005 more than 87 % of the publications and 90 % of the installed SPR devices were by Biacore™ [88]. SPR investigations on cells have been performed on gold substrates as used in this thesis but without PDMS reaction chambers, which includes the possibility to put a dried out cell layer into the measuring device [89]. Literature reports of cell suspensions measured on a gold substrate [83]. Experiments on cellular response after GPCR activation have been performed [90] aiming for general cell response monitoring rather than investigating specific signal patterns recorded with SPR systems. The improved and optimized dual ECIS-SPR sensor system provides online monitoring of confluent cell layers like U-373 MG cells using both readout approaches. The device returns accurately reproducible signal patterns for each measurement principle after stimulating the histamine receptor. The EnSpire™ multimode reader (PerkinElmer, Waltham, USA) used in this thesis has no technical options for direct addition of drugs to the bathing fluid in contrast to the dual ECIS-SPR sensor. Drug addition to cells residing in 384-well multiwell plates needs to be performed outside the multimode reader with a multichannel electronic finnpipette and induces major disturbances of the readout due to cooling and warming of cells and solutions. The custom made dual ECIS-SPR sensor with the manual liquid exchange protocol offers a platform for undisturbed online monitoring and analysis of fingerprint like signalling profiles.

4.2 Theoretical Analysis of the Cell-Surface Junction in SPR and ECIS Recordings

4.2.1 Analysis of the Cell-Surface Junction in SPR-Recordings

The penetration depth of the SPR signal is in the order of 100 to 200 nm. As the cells are hovering in a distance between 20 nm and 200 nm from the surface of the SPR chip, the SPR signal must be dominated by the particular conditions and geometries of the cell-surface junction. Besides the distance between sensor surface and lower cell membrane, the refractive index of the cleft (n_{Cleft}) in between chip and membrane, the refractive index of the membrane (n_{mem}) and the refractive index of the cytoplasm (n_{cyt}) are assumed to affect the outcome of the measurement. These factors have a direct impact on the measured reflectivity (R / R.U.) and the angle of minimum reflectivity (θ_{min} / °). Fig. 4-4 shows a typical scan of the reflectivity as a function of the angle of incidence. The characteristic points within such datasets are the magnitude of minimum reflectivity and the corresponding angel of incidence. Real time monitoring with the dual ECIS-SPR sensor uses a fixed angle of incidence at which the reflectivity shows the maximum slope ($dR/d\theta$). The reflectivity at this angle of incidence is recorded as a function of time R(t). Changes in any of the above mentioned parameters describing the cell-surface junction are expected to have influence on the two SPR parameters θ and R even though there has never been any systematic study of this. Accordingly, when the impact of the different parameters of the cell-surface junction on the SPR signal is quantitatively known, it might be possible to interpret SPR time course data on the cellular level opening a new perspective for cell-based assays.

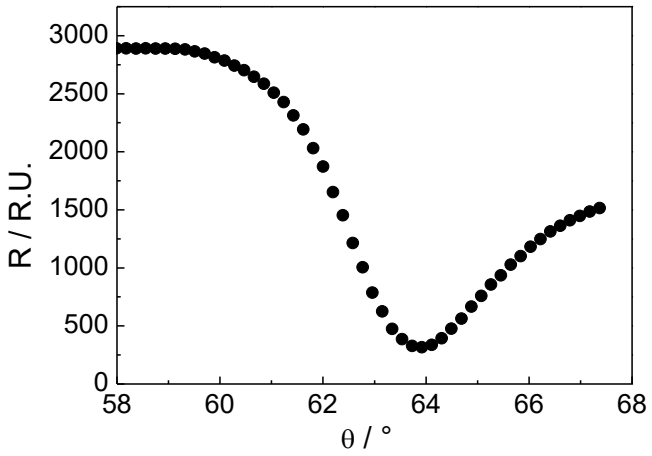

Fig. 4-4 Reflectivity R as a function of the angle of incidence θ. Monitoring the reflectivity (R/R.U.) at the angle of maximum slope ($dR/d\theta$) provides a sensitive measure for changes occurring in the cells close to the substrate.

The following simulations estimate the influence of the various parameters of the cell-surface junction on the scans of reflectivity as a function of angle of incidence. The reference situation for all theoretical simulations is a cell layer in which all individual cells have a defined plasma membrane thickness (d_{mem} = 4 nm), a specific refractive index (RI) of the cytosol (n_{cyt} = 1.33), the refractive index of the cleft between cell membrane and gold surface (n_{cleft} = 1.33), and an average refractive index of the membrane/lipid bilayer (n_{mem} = 1.45) itself. In all calculations the width of the cleft between the cell membrane and the gold surface d_{cleft} was varied between 0 and 300 nm. The light beam used in the simulation has a wave length of 632 nm. The theoretical simulations were performed with the spall70 software (Version 3.1., Optrel GBR, Germany). Reflectivity tracking was performed at a fixed angle of incidence at 62°, which typically refers to the angle of maximum slope as concluded from angle scan experiments (Fig. 4-4) recorded with the SPR device used in this thesis. The reference values of all parameters of the cell-surface junction are summarized in the Table 4-1:

Table 4-1: Physical parameters of the cell-surface junction as they were used for the reference cell layer on the SPR chip in subsequent simulations. n_{cleft} is the refractive index of the cleft between membrane and gold surface, n_{mem} represents the refractive index of the lipid bilayer, n_{cyt} represents the refractive index of the cytoplasm inside the cell, and d_{mem} represents the lipid bilayer thickness [89, 91].

	reference value	**variation**
n_{cleft}	1.33	± 0.05
n_{mem}	1.45	± 0.05
n_{cyt}	1.33	± 0.05
d_{mem}	4 nm	± 0.5 nm

A systematic analysis will reveal the individual impact of any of these physical parameters of the cell-surface junction on the overall SPR readout. Therefore, each parameter is systematically varied in the interval reference value ± variation.

Fig. 4-5 sketches the situation for SPR sensors with a cell (square shape) hovering in a distance d_{cleft} of 0 nm (A) and 300 nm (B) above the gold surface covering a supporting glass slide. To uncover the impact of d_{cleft} on SPR readouts, the parameter was systematically varied from 0 nm to 300 nm. All other parameters were kept constant at their reference values. The reference values of the four other parameters are given in table 4-1 and are estimates taken from the literature [88, 89]. For the case, cleft size is different from zero ($d_{cleft} \neq 0$ nm), the cleft is represented by a layer of cell culture medium completely filling the space between the lipid bilayer and the gold surface. The refractive index of the cytosol may change as a consequence of dynamic mass redistribution induced by downstream signalling of GPCR activation. The lipid bilayer of the cell may differ in its composition due to insertion or removal of a receptor from the cell membrane which changes its refractive index n_{mem}. The membrane

thickness d_{mem} is another value which has influence on the SPR readout. The distance between membrane and gold surface d_{cleft} is systematically varied for all different parameter combinations as this is supposedly the most decisive parameter for cell-based assays. Morphological changes of the cells may lead to significant changes in d_{cleft} that may be the dominant factor for the changes observed in the SPR signals.

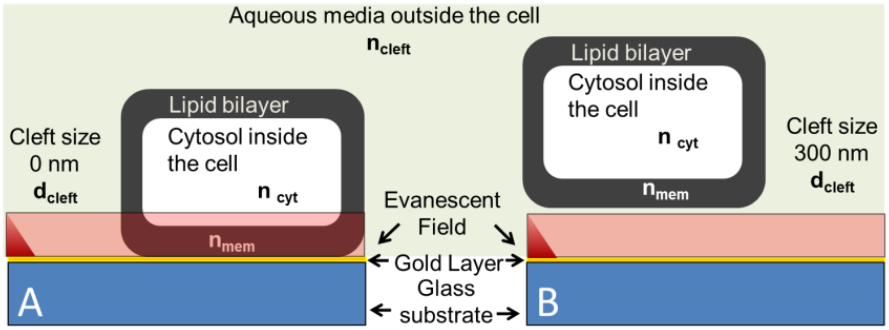

Fig. 4-5 Sketch illustrating cell-surface junction that is modelled with respect to its SPR signature. In (A) the cell is placed directly on the gold surface of the sensor chip (cleft size 0 nm). For all combinations of the parameters of the cell surface junction, an increasing cleft width d_{cleft} was analysed with respect to its impact on the SPR readout. (B) illustrates the situation for the biggest d_{cleft}, when the cell has left the reach of the evanescent field.

The model described in Fig. 4-5 was used to calculate angle scans for various sets of parameters as listed in Table 4-1. The following graphs contain always seven datasets which describe the outcome for one parameter changed in seven increments while all other parameters were kept constant. The parameter of interest gets increased (3 values) and decreased (3 values) around the reference value. In this series, the first graph describes always the angle of minimum reflectivity θ_{min} (θ_{min} / °) for minimum reflectivity as a function of distance between membrane and SPR chip (d_{cleft} / nm). The second graph always describes the reflectivity $R_{62°}$ measured at a constant angle of incidence of θ = 62 ° as a function of distance (d_{cleft}/nm) according to the real measurement conditions (Fig. 4-4). These two graphs are then combined in a three dimensional graph. The 3D graph illustrates the interdependence of minimum reflectivity $R_{62°}$ measured at a constant angle of incidence of θ = 62 °, angle of minimum reflectivity θ_{min} (θ_{min} / °) and the distance (d_{cleft} / nm). The series of curves for gradual changes of one of the remaining parameters shows the direct influence of this parameter on $R_{62°}$ and θ_{min}.

4.2.1.1 Variations of the refractive index of the cleft (n_{cleft})

Fig. 4-6 shows the angle of minimum reflectivity θ_{min} as a function of the distance d_{cleft} when the refractive index of the aqueous layer in the cleft (n_{cleft}) is changed systematically. For the reference value (n_{cleft} = 1.33) of the medium θ_{min} changes from 62° to 61.3° with increasing

distance d_{cleft}. In this particular case the refractive indices of the cleft n_{cleft} and the cytosol n_{cyt} are identical. Increasing the distance between cell and gold surface has only a minor influence on the angle of minimum reflectivity θ_{min}. The graph shows further 6 simulations with higher and lower refractive indices n_{cleft}. The increase of the n_{cleft} (max n_{cleft} = 1.38) leads to a shift of the angle of minimum reflectivity θ_{min} to higher values with increasing distance to the surface (θ_{min} = 67.2°). Higher refractive indices lead to bigger final values for the minimum angle of incidence. Decreasing n_{cleft} (min n_{cleft} = 1.28) leads to a decrease of the final minimum angle of incidence (θ_{min} = 55.4°) for the largest distance between cell and surface. The smallest n_{cleft} leads to the biggest decrease of the angle of minimum reflectivity θ_{min}. Small variations of the n_{cleft} (Reference n_{cleft} = 1.33) of the media are shifting the angle of minimum reflectivity θ_{min} to higher values with a higher n_{cleft}, while lower n_{cleft} than the reference value leads to smaller angle of minimum reflectivity θ_{min} with a increasing distance between cell and gold surface.

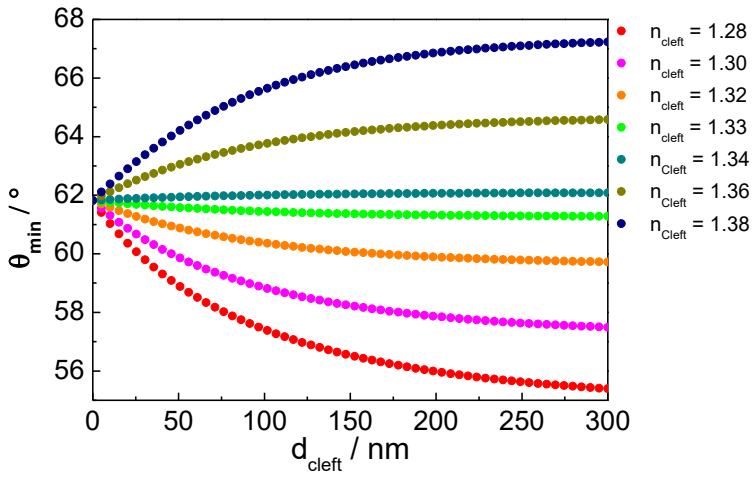

Fig. 4-6 Angle of minimum reflectivity θ_{min} as a function of distance between lower cell membrane and surface in a 4-layer system. The series of curves is calculated for different refractive indices of the cleft between the gold surface and the cell membrane (d_{cleft} / nm).

Fig. 4-7 shows the reflectivity $R_{62°}$ measured at a constant angle of incidence of θ = 62° at the minimum angle of incidence θ_{min} as a function of cleft height underneath the cells. Reflectivity tracking was performed at a fixed angle at 62 °. For the reference value (n_{cleft} = 1.33) $R_{62°}$ starts with a reflectivity close to zero. Increasing the distance between cell/gold surface to 300 nm leads to a reflectivity increase to 0.1. The increase of the refractive index to a value of n_{cleft} = 1.34 induces almost zero change in reflectivity with increasing distance d_{cleft}. In these two cases the variation of the refractive index has a very small influence on the cleft height dependent reflectivity. The next smaller RI (n_{cleft} = 1.32) increases the reflectivity up to 0.3 at a distance of 300 nm. Greater changes of the RI higher and lower than the reference value lead to massive increases of the reflectivity to about 0.5 and more within the first 150 nm of distance cell/gold.

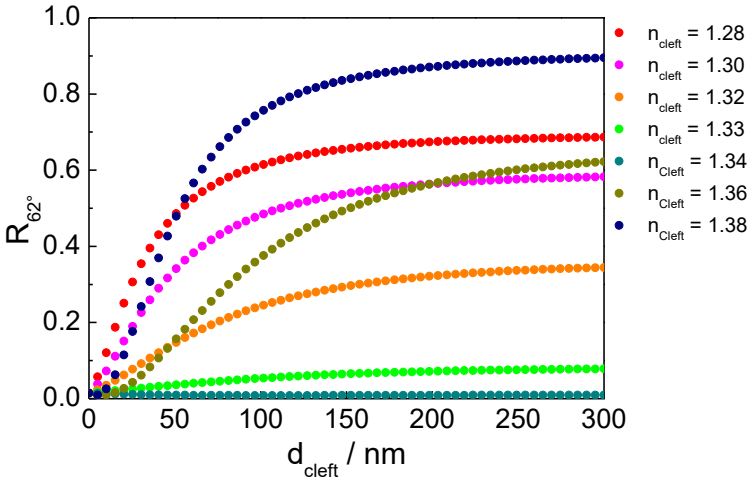

Fig. 4-7 Reflectivity $R_{62°}$ measured at a constant angle of incidence of θ = 62° as a function of distance between membrane and surface. The series of curves represents different refractive indices of the cleft (n_{cleft}) between membrane and surface.

Fig. 4-8 combines the previous two graphs in one plot. The reference value (n_{cleft} = 1.33) and the next higher one (n_{cleft} = 1.34) show minimal changes in angle of minimum reflectivity θ_{min} and reflectivity with an increasing gap between cell membrane and gold surface. The next smaller value for n_{cleft} (n_{cleft} = 1.32) describes a shift to lower angle of minimum reflectivity θ_{min} (from 62° to 60°) and an increase in reflectivity to 0.3. The two smallest refractive indices (n_{cleft} = 1.30; n_{cleft} = 1.28) curves describe a more intensive increase in reflectivity (> 0.5) and a bigger shift to lower angle values. The two biggest RI (n_{cleft} = 1.36, n_{cleft} = 1.38) describe curves to increased angle values θ_{min} and an increase of reflectivity (> 0.5) when the cell is the farthest away from the surface (300 nm). The value of n_{cleft} alters the cleft height d_{cleft} dependence of minimum angle θ_{min} and reflectivity.

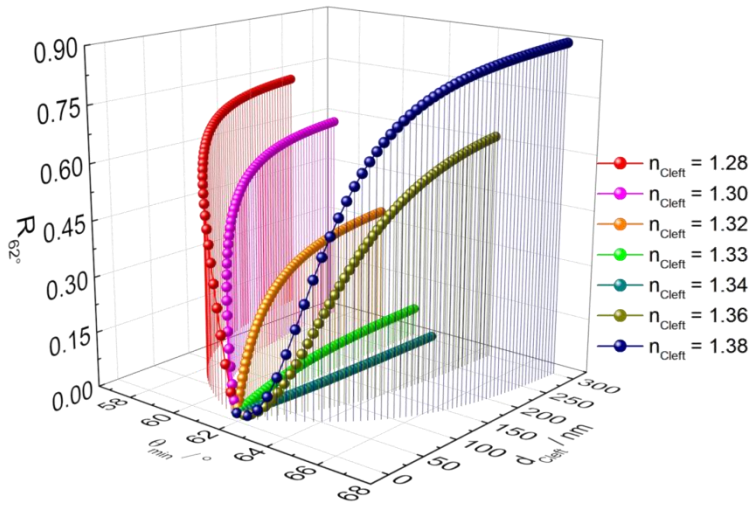

Fig. 4-8 is a combination of Fig. **4-6** and Fig. **4-7** and shows the 3 dimensional plot. The series of curves represents different refractive indices of the cleft (n_{cleft}) between membrane and surface.

4.2.1.2 *Variations of the refractive index of cytosol (n_{cyt})*

Fig. 4-9 describes the shift of the angle of minimum reflectivity θ_{min} as a function of the cleft height d_{cleft} for different refractive indices of the cytosol (n_{cyt}). Starting with the reference value for n_{cyt} (n_{cyt} = 1.33; θ_{min} = 62°), lifting the cell from the surface causes minimal changes in the angle of minimum reflectivity θ_{min} which is at the maximum distance d_{cleft} = 300 nm between cell and gold surface almost unchanged compared to the smallest distance d_{cleft} = 0 nm and amounts to 61.2°. An increase of n_{cyt} to values of 1.38 induces a higher starting value for the angle of minimum reflectivity θ_{min} for d_{cleft} = 0 nm (θ_{min} = 68°) converging to a minimum (θ_{min} = 62°) for the biggest distance d_{cleft}. A decrease of the n_{cyt} down to 1.28 causes a decrease of the starting value of the angle of minimum reflectivity θ_{min} (θ_{min} = 56°). An increase of the cleft width from d_{cleft} = 0 nm to 300 nm increases the angle of minimum reflectivity θ_{min}. It eventually asymptotically approaches values of the reference state (θ_{min} = 62°) for d_{cleft} = 300 nm.

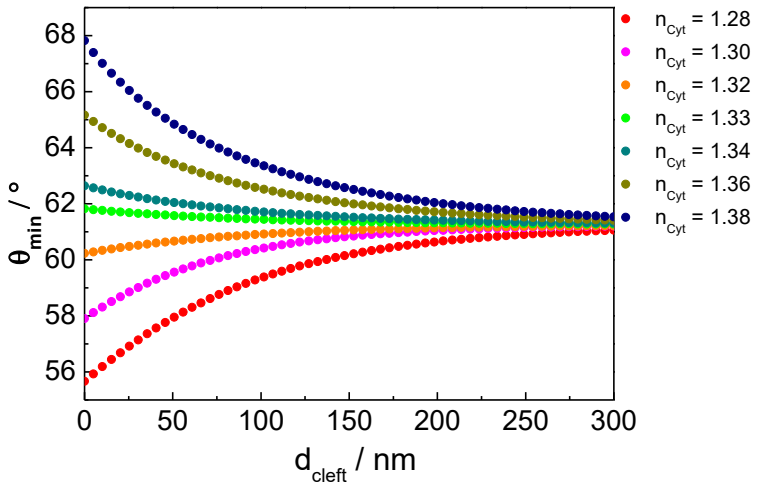

Fig. 4-9 Angle of minimum reflectivity θ_{min} as a function of cleft height d_{cleft} between the gold surface and the cell membrane (d_{cleft} / nm). The seven lines simulate different refractive indices of the cytosol (n_{cyt}).

Fig. 4-10 shows the reflectivity $R_{62°}$ as a function cleft height d_{cleft} when the refractive index in the cytosol n_{cyt} is varied systematically. The graph describes how $R_{62°}$ changes when the cell is lifting up from the gold surface and out of the evanescent field. The reference value (n_{cyt} = 1.33) induces a reflectivity almost to zero. Increasing the distance between cell/gold surface to 300 nm leads to a reflectivity increase to 0.1. Smaller Values of the refractive index (n_{cyt} < 1.33) start systematically at higher reflectivity and drop to a minimum of reflectivity (0.1) as the cell is lifted to higher distances d_{cleft}. The smallest value (n_{cleft} =1.28) induces a reflectivity of 0.7 at d_{cleft} = 0 nm and is reaching a minimum in a distance of 300 nm from the gold surface. The higher the value of the n_{cyt} is the higher is the starting point of reflectivity. The biggest value (n_{cleft} =1.38) induces a reflectivity of 0.92 at d_{cleft} = 0 nm and is reaching a minimum reflectivity (0.02) in a distance of 225 nm from the gold surface. All the curves converge to reflectivity of 0.1, finally having the nearly same reflectivity as the cell with the reference value (n_{cyt} = 1.33).

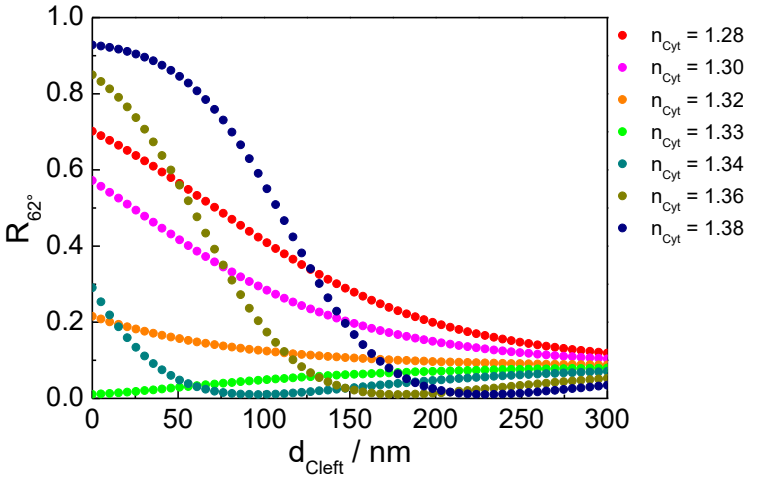

Fig. 4-10 Reflectivity $R_{62°}$ at constant angle of incidence θ = 62 ° as a function of distance between membrane and surface d_{cleft}. The series of curves represents different refractive indices of the cytosol n_{cyt}.

Fig. 4-11 combines the previous two graphs in one plot. The reference curve starts with almost zero reflectivity and a minimum angle of 62°. The reference curve increases to 0.1 reflectivity at a distance d_{cleft} = 300 nm. It converges with all other curves in the plot to a reflectivity of 0.1. The minimum angle gradually decreases towards 61° for all curves while bigger n_{cyt} goes along with higher θ_{min} values and lower n_{cyt} with lower θ_{min}. The curve for the lowest refractive index of the cytosol (n_{cyt} = 1.28) starts at a minimum angle of 56° for d_{cleft} = 0 nm and undergoes a gradual and monotonic increase to 61° with d_{cleft} = 300 nm. The reflectivity starts at 0.65 and decreases with max distance from the surface down to 0.1 reflectivity and reaches at that point a minimum angle of 61°. Increasing n_{cyt} from the smallest value compared to the reference value (n_{cyt} = 1.33) under study gradually shifts the curves to lower starting points of the reflectivity and higher starting angles. The next bigger n_{cyt} compared to the reference value starts at a reflectivity of 0.3 and shows a rapid decrease within the first 100 nm to almost 0 reflectivity rising to a value of 0.1 at for the maximum distance d_{cleft}. The minimum angel shifts from 63° to 61° where all the curves converge to. The two highest n_{cyt} provide angle shifts from individually higher angles for d_{cleft} = 0 to the end point of 61° for d_{cleft} = 300 nm, while the reflectivity begins for the biggest n_{cyt} at 0.92 and finishes at 0.1. The biggest n_{cyt} induces almost the same angle shift from the reference state in opposite directions than the smallest value and approach from different sides to an angle of 61 ° and a reflectivity of nearly 0.1 independent of d_{cleft}.

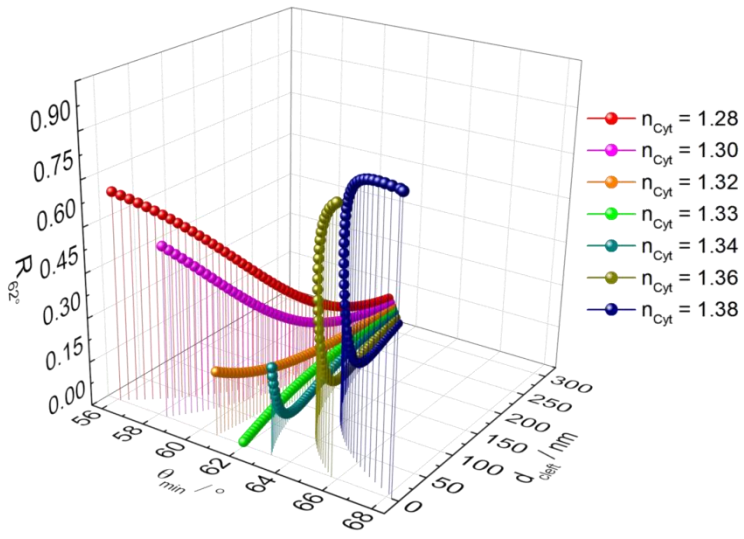

Fig. 4-11. is a combination of **Fig. 4-9** and **Fig. 4-10** and shows the 3 dimensional plot. The series of curves represents different refractive indices of the cytosol (n_{cyt}).

4.2.1.3 *Variations of the refractive index of the lipid bilayer membrane (n_{mem})*

Fig. 4-12 describes the impact of varying the refractive index of the plasma membrane n_{mem} on the angle of minimum reflectivity θ_{min} in the system under study. For all conditions, the angle of minimum reflectivity θ_{min} falls monotonically with increasing distance between membrane and surface and converges with the reference curve at high distances. For the reference value (n_{mem} = 1.45) the minimum angle at d_{cleft} = 0 nm amounts to 61.8° and decreases within a distance of 300 nm by 0.5°. Decreasing the refractive index of the bilayer to n_{mem} = 1.40 causes the curve to start at lower values for the angle of minimum reflectivity θ_{min} of about 61.6° while a bigger cleft leads to an end value very close to the reference value. The other way round an increase of the refractive index n_{mem} to 1.50 induces a bigger minimum angle of 62° for d_{cleft} = 0 nm that also converges to the reference curve for high cleft heights with a final value of θ_{min} = 61.3°. All curves share the monotonic decrease with rising distance d_{cleft} and the highest slope of the descending curve is observed for the biggest n_{mem}.

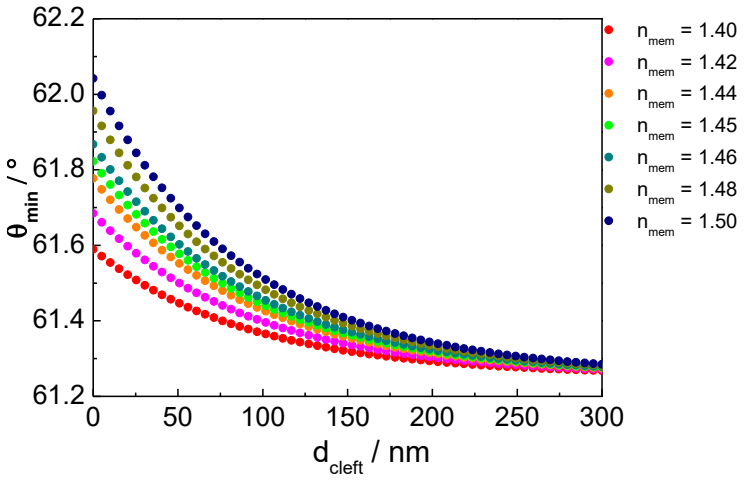

Fig. 4-12 Angle of minimum reflectivity θ_{min} as a function of cleft height d_{cleft} between the gold surface and the cell membrane (d_{cleft} / nm). The seven lines simulate different refractive indices of the membrane lipid bilayer.

Fig. 4-13 Shows the reflectivity $R_{62°}$ as a function of distance d_{cleft} when the cell membrane is modelled with increasing refractive indices n_{mem} of the membrane lipid bilayer. The reference curve (n_{mem} = 1.45) describes a reflectivity increase from 0.01 to 0.07 when d_{cleft} is varied from 0 nm to 300 nm. Bigger n_{mem} produce curves that start from smaller values at d_{cleft} = 0 nm compared to the reference curve but they all converge at a final value of 0.07 when d_{cleft} is closed to 300 nm and beyond. Smaller n_{mem} start at somewhat higher values at d_{cleft} = 0 nm compared to the reference and finish with similar curve patterns approaching 0.07 reflectivity for big cleft heights.

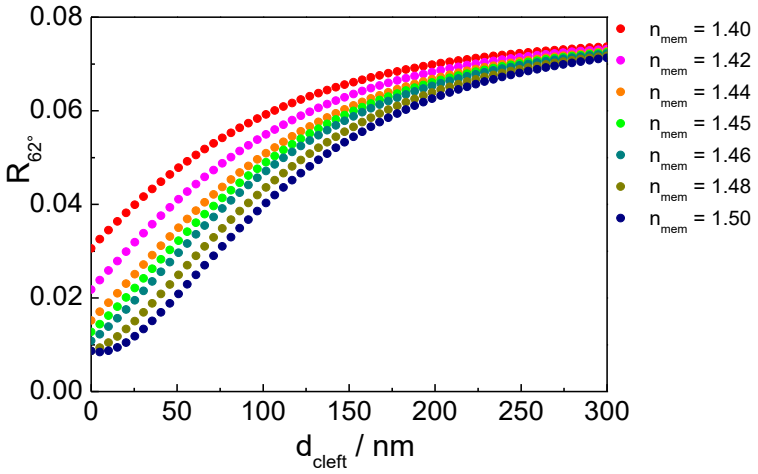

Fig. 4-13 Reflectivity $R_{62°}$ at a constant angle of incidence θ= 62 ° as a function of distance between membrane and surface d_{cleft}. The series of curves represents different refractive indices of the basal plasma membrane (n_{mem}).

Fig. 4-14 combines the previous two graphs in one plot. The reference curve (n_{mem} = 1.45) starts at 0.01 reflectivity and an angle of 61.8°. While lifting the cell up and thereby increasing

d_{cleft}, the curve increases to a reflectivity of 0.07 and slip to a smaller angle of 61.3°. Higher n_{mem} does not induce significantly lower reflectivity values at d_{cleft} = 0 nm but a bigger minimum angle of incidence. Lower n_{mem} are shifted to a higher starting value in reflectivity at d_{cleft} = 0 nm and smaller minimum angle of incidence compared to the reference curve.

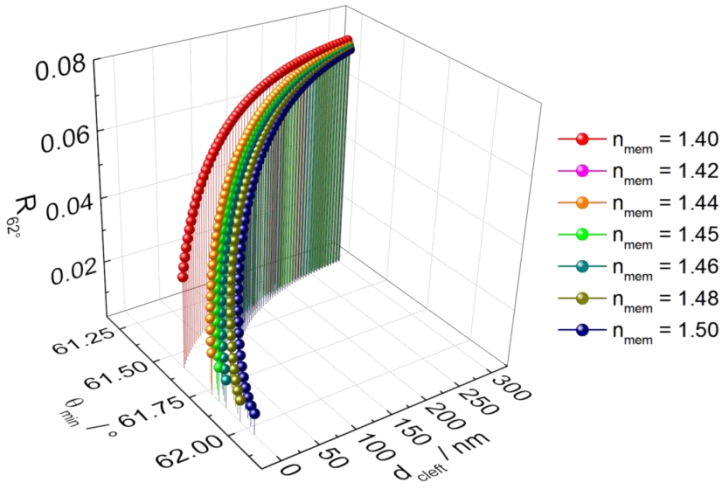

Fig. 4-14 is a combination of **Fig. 4-12** and **Fig. 4-13** and shows the 3 dimensional plot. The series of curves represents different refractive indices of the lipid bilayer (n_{mem}) of the basal side of the membrane.

4.2.1.4 *Variations of the thickness of the lipid bilayer (d_{mem})*

Fig. 4-15 shows the dependence of the angle of minimum reflectivity θ_{min} on the cleft width d_{cleft} for different thicknesses of the lipid bilayer. d_{mem} is increased and decreased relative to the reference value (d = 4 nm). All curves share a monotonic exponential decay with increasing cleft height d_{cleft}. The differences observed for different membrane thicknesses are minor. For the reference membrane thickness d_{mem} = 4 nm the minimum angle falls from 61.8° to a final value of 61.3° when the cleft height amounts to 300 nm. The simulation of thinner bilayers (min 3.5 nm) are slightly shifted to lower values but describe the same curve shape and converge at 61.3 ° with the reference curve at d_{cleft} = 300 nm. Bigger bilayers (max 4.5 nm) are slightly shifted to higher values compared to the reference value and converge similarly to a minimum angle value of 61.3° at d_{cleft} = 300 nm.

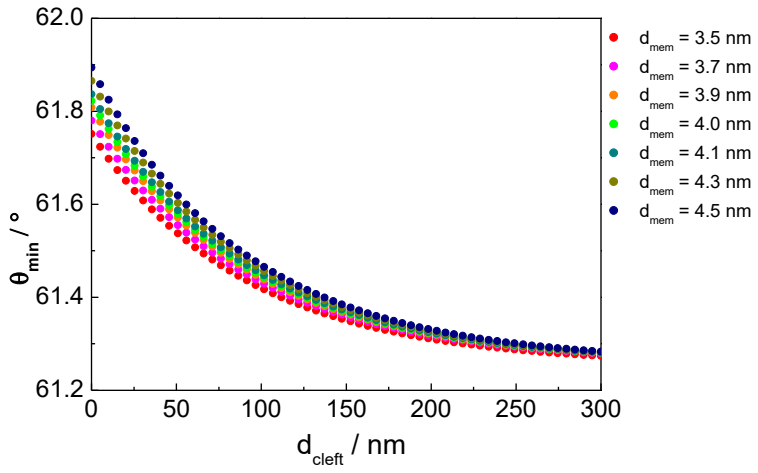

Fig. 4-15 Angle of minimum reflectivity θ_{min} as a function of cleft height d_{cleft} between the gold surface and the cell membrane (d_{cleft} / nm). The seven lines simulate different thicknesses of the plasma membrane (d_{mem}).

Fig. 4-16 shows the reflectivity $R_{62°}$ as a function of cleft height d_{cleft} when the thickness of the cellular plasma membrane is systematically varied. All curves share a monotonic increase and converge with the reference curve at d_{cleft} = 300 nm. The reference curve (d = 4 nm) in this simulation produces a reflectivity of 0.01 at d_{cleft} = 0 nm and increases to 0.07 for d_{cleft} = 300 nm. Curves with bigger membrane thickness are shifted below the reference curve and describe a very similar pattern. Thinner membranes are shifted to slightly higher values of the reflectivity compared of the reference curve.

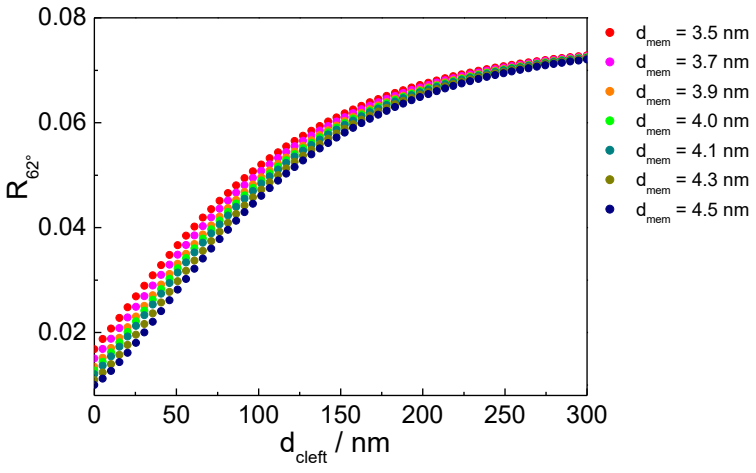

Fig. 4-16 Reflectivity $R_{62°}$ at a constant angle of incidence of θ=62 ° as a function of distance between membrane and surface d_{cleft}. The series of curves represents different thicknesses of the basal membrane (d_{mem}).

Fig. 4-17 combines the previous two graphs in one plot. The reference curve (d = 4 nm) starts at one percent reflectivity and an angle of 61.8°. When the distance between plasma

membrane and substrate d_{cleft} is gradually increased, the curve increases to a reflectivity of 7 % and while the minimum angle is reduced to a value of 61.3°. All curves converge with the reference curve for at d_{cleft} = 300 nm.

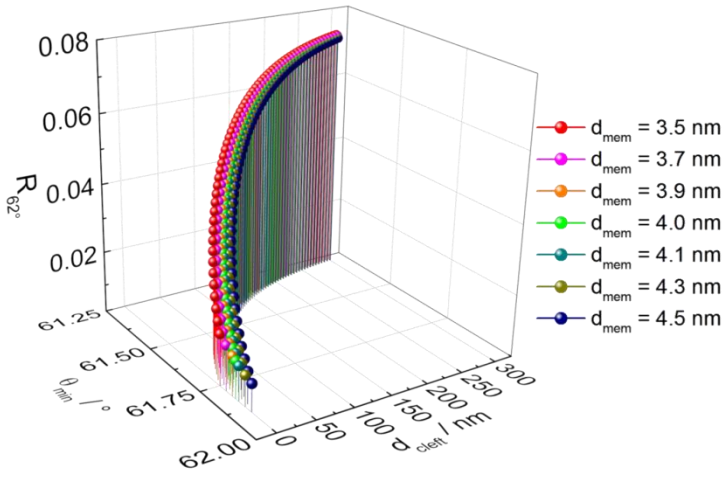

Fig. 4-17 is a combination of **Fig. 4-15** and **Fig. 4-16** and shows the 3 dimensional plot. The series of curves represents different thicknesses of the lipid bilayer (d_{mem}).

4.2.1.5 *Discussion*

The cell model for SPR simulation was established in order to have a comparable base for simulations as provided by the ECIS cell model [66, 92]. Reference values (Table 4-1) (n_{cleft}, n_{cyt}, n_{mem}, d_{mem}, d_{cleft}) were taken from literature analysis of cell models [89, 91].

The parameters that were included in the optical model (n_{cyt}, n_{mem}, n_{cleft}, d_{cleft}, d_{mem}) demonstrated a very different and individual impact on the two readout parameters $R_{62°}$ (reflectivity) and θ_{min} (angle of minimum reflectivity). Two main categories can be defined with respect to the individual impact of the parameters.

Category one – low impact: The parameters of the plasma membrane (d_{mem}, n_{mem}) show only a minor influence on the changes of reflectivity and the corresponding angel of minimum reflectivity. Varying the refractive index (n_{mem}) of the lipid bilayer induces maximal changes in the range of up to 0.06 in reflectivity $R_{62°}$ and changes in the angle of minimum reflectivity θ_{min} to a maximum of 0.75 °. The thickness of the membrane d_{mem} has approximately the same minor influence on the two observables as the refractive index of the membrane. The

maximum changes in reflectivity amount to 0.06 and the maximum changes of the minimum angle amount to 0.75 ° when the cleft height is increased from 0 nm to 300 nm.

Category 2 high impact: According to the calculations the model parameters n_{cyt}, n_{cleft} and d_{cleft} have a considerable impact on the two observables. Refractive indices of the cleft (n_{cleft}) have a big influence on reflectivity and resonant angle changes. The impact of the refractive index of the cleft is visible immediately when the distance between lower membrane and SPR sensor is altered. When the distance between cell and surface increases, the material in contact to the chip is more homogeneous and resembles more a bulk phase within the evanescent field. Once the cell membrane has left the evanescent field the medium in contact with the chip is supposedly close to medium that is not affected by the cellular parameters. The impact of the cytosol is tremendous as well. At the beginning of every simulation (d_{cleft} = 0 nm) the cytosol is the main part of the cell within the evanescent field. The membrane itself has minor influence on $R_{62°}$ and θ_{min} and acts like a separation layer. The influence of the cleft (n_{cleft}) and the cytosol (n_{cyt}) depend mainly on the cleft size (d_{cleft}). Fig. 4-18 shows a comparative presentation of the various simulations with the changes in refractive indices expressed on a normalized scale. The graphs combine the influence of the cleft (n_{cleft}), cytosol (n_{cyt}) and membrane (n_{mem}) for individual cleft sizes (d_{cleft}) in one plot.

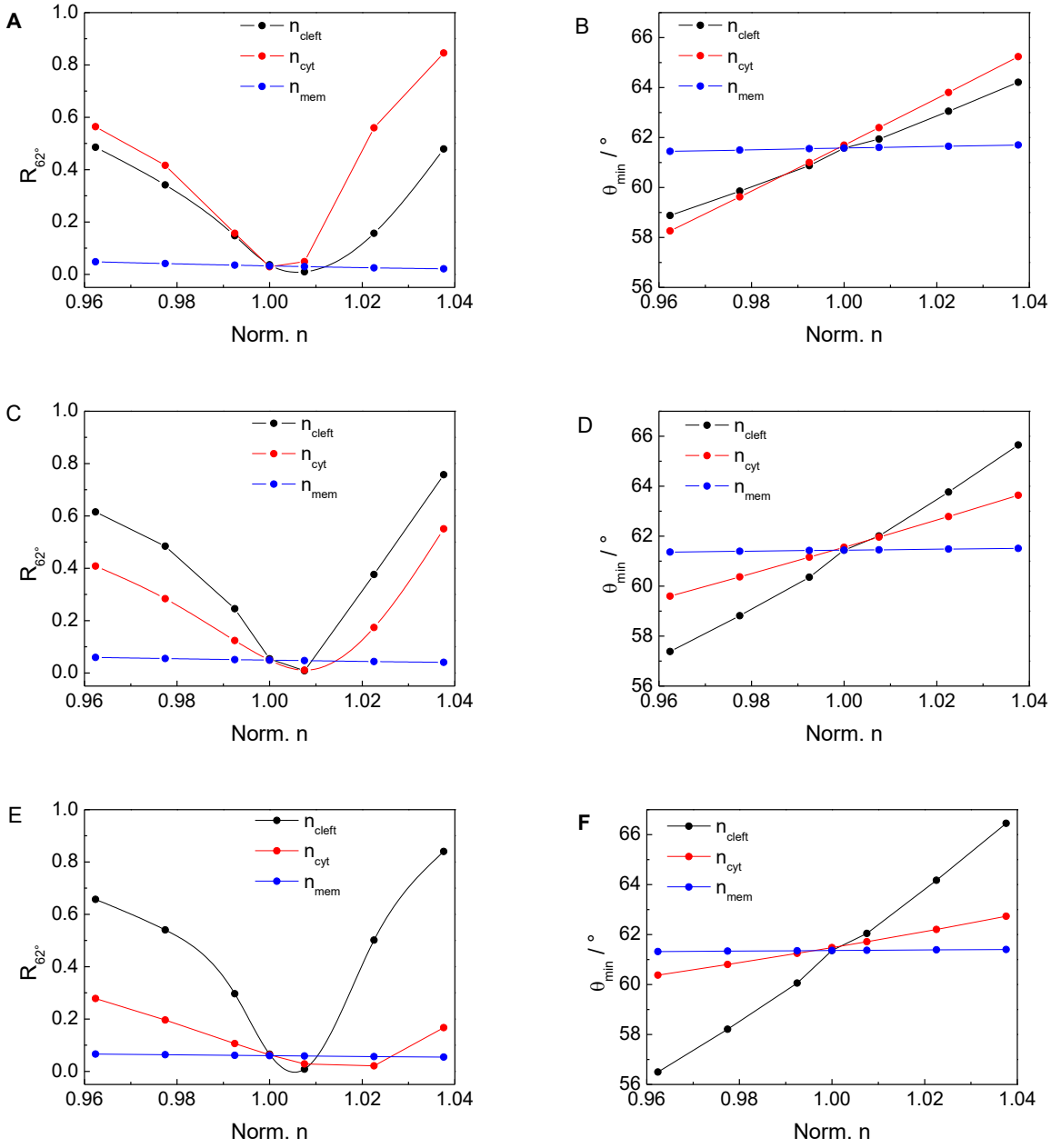

Fig. 4-18 Comparison of the impact of optical parameters of the cell-surface junctions on SPR measured for different cleft widths: d_{cleft} = 50nm (**A, B**), d_{cleft} = 100 nm (**C,D**) and d_{cleft} =150 nm (**E, F**). Reflectivity at θ = 62 ° and angle of minimum reflectivity (θ_{min}) as function of the different refractive indices n normalized to the reference values of n_{cleft}, n_{cyt}, n_{mem} (Norm. n = 1). Lower refractive indices are <1 while bigger n is >1.

Fig. 4-18 shows reflectivity $R_{62°}$ at a constant angle of incidence θ = 62° and angle of minimum reflectivity θ_{min} as function of the various refractive indices normalized to the reference values of the cleft, cytosol and membrane. Reflectivity and angle of minimum reflectivity are plotted for three cleft sizes: 50 nm (Fig. 4-18; A, B), 100 nm (Fig. 4-18; C, D) and 150 nm (Fig. 4-18; E, F). For d_{cleft} = 50 nm the cleft and the cytosol show similar changes for lower n values while for bigger n values the cytosol shows a bigger change of reflectivity compared to the cleft. The membrane does not show a significant influence on $R_{62°}$. Angle of minimum reflectivity θ_{min} gets lower for smaller n_{cleft} and n_{cyt} values compared to the reference while for bigger n values

the angle gets increased and the cytosol show a bigger shift of θ_{min} as the cleft. For d_{cleft} = 100 nm changes within the cytosol have a smaller impact on changes of $R_{62°}$ and θ_{min} compared to the cleft. The cell is hovering 100 nm above the gold surface and changes of the n_{cleft} show bigger impact on $R_{62°}$ and θ_{min}. For d_{cleft} = 150 nm the n_{cleft} is the major determinant of $R_{62°}$ and θ_{min} changes for different refractive indices as the cell is getting lifted out of the evanescent field.

This simulation has the approach of analysing the impact of (i) the layer of medium above the substrate (n_{cleft}), (ii) the plasma membrane (n_{mem}) and (iii) the cytosol (n_{cyt}). With an evanescent field of 100 – 200 nm, the basal region of a cell is the main determinant on the reflectivity and the angle of incidence. Studies have shown specific refractive indices for specific cell types (liver cells n=1.38-1.395 [93, 94]; fibroblast (n=1.358-1.374 ([95, 96]); mammalian tissue (n=1.38-1.41 [97]; smooth muscle n=1.36 [98]; neurons n=1.375-1.384 [99]. Microscopic studies have determined different refractive indices in different cellular regions [98]. Changes of refractive indices have been measured by phase microscopy in conjunction with confocal microscopy to measure refractive indices of cultured muscle cells [98]. Applying hypertonic solution to confluent cells (MDCK II) on a SPR gold substrate was described as refractive index increase while hypotonic solution caused reflectivity decrease. [100]. This backs the simulations as a change of cytosol composition has a major influence on reflectivity change. The organelles inside of cells have specific refractive indices by themselves [101], but this fact was not considered in this simulation.

This SPR simulation shows the big influence of the refractive index by the cytoplasm and the cleft between substrate and basal side of the cell, separated by a membrane, as these are the major cellular structures within the evanescent field. Reflectivity and angle of minimum reflectivity are directly influenced by the changes of specific refractive indices in a cell (n_{cyt}) and the medium layer between substrate and cell membrane (n_{cleft}).

4.2.2 Analysis of the Cell-Surface Junction in ECIS-Recordings

4.2.2.1 *Simulated Impedance Spectra of Cell Monolayers grown on Gold-Film Electrodes*

In the previous chapter, the cell-surface junction was simulated for optical recordings by means of surface plasmon resonance spectroscopy. The critical parameters were found to be the distance between cell and surface d_{cleft} and the optical properties in the interfacial region. The height of the electrolyte-filled channel underneath the cells d_{cleft} is particularly critical since

it may exceed the penetration depth of the evanescent field. Under these conditions, the cells become invisible for SPR recordings. Similarly, d_{cleft} is also one out of three parameters related to cell structure that impacts the impedance of cell–covered electrodes A dielectric model of a cell monolayer hovering in a distance d_{cleft} from the surface allows calculating the impact of this parameter on the overall impedance readout. Besides $d_{cleft,}$ the cell layer is further modelled by a capacitance C_m that represents the dielectric properties of the plasma membrane as well as a resistor R_b that accounts for the resistive pathway around the cells.

4.2.2.2 *Variation of the cleft between cell and surface (d_{cleft})*

In the simulations, the parameters R_b and C_m were fixed to reasonable values and the parameter α that describes the impedance of the cell-surface junction including the cleft height d_{cleft} was systematically varied (Table 4-2). The parameter α is defined as follows (1.3.1):

$$\alpha = r_c(\rho/d_{cleft})^{\frac{1}{2}} \qquad \text{(Eq. 15)}$$

The parameter r_c (fixed) stands for the radius of the cell, ρ_{bulk} (fixed) describes the specific resistivity of the electrolyte in the cleft. The distance between cell and electrode is d_{cleft}. R_b (fixed) represents the resistance between cells. C_m is the membrane capacitance (fixed).

Table 4-2 Values used to calculate frequency dependent impedance spectra for cell-covered electrodes. The α value depends directly on the distance between cell and electrode (Eq. 15). All other parameters R_b, c_m, r_c and the ρ_{bulk} are fixed to reasonable values for cells with a non-epithelial phenotype (low barrier, no microvilli). Electrode parameters are: $A_{Electrode}$ = 0.0064 cm², A_{CPE} =1.5*10^{-5} F·s^{n-1}·cm^{-2}, n_{CPE} = 0.96, R_{bulk}= 1000 Ω.

No.	R_b [Ωcm²]	c_m [µF/cm²]	r_c [µm]	d_{cleft} [nm]	ρ [Ωcm]	α [Ω$^{0.5}$cm]
1	10.0	1	10.0	5	55	10.49
2	10.0	1	10.0	15	55	6.06
3	10.0	1	10.0	25	55	4.69
4	10.0	1	10.0	50	55	3.32
5	10.0	1	10.0	75	55	2.71
6	**10.0**	**1**	**10.0**	**100**	**55**	**2.35**
7	10.0	1	10.0	150	55	1.91
8	10.0	1	10.0	200	55	1.66
9	10.0	1	10.0	250	55	1.48
10	10.0	1	10.0	300	55	1.35

The parameter of interest, the cleft height d_{cleft}, is constantly increased beginning with a cleft size of 5 nm. The directly corresponding α-values decrease constantly according to Eq. 15. The upper limit for d_{cleft} in this simulation is identical to the SPR simulation provided by 300 nm cleft size. The frequency scans for the individual values of d_{cleft} are plotted in Fig. 4-19. The simulation software Virtual-*ECIS* was written by Prof. Wegener (University of Regensburg) using the software packages LabView and Matlab. The impedance spectrum of the cell free electrode (w/o c) is the lowermost curve (black). Cell-covered electrodes show higher impedance values at all frequencies. The smaller the distance from the substrate to the cell (d_{cleft}), the bigger the impedance values across the frequency range and the bigger the gap between cell free and cell covered electrode. The smallest values for d_{cleft} = 5 nm show the biggest impedance values. The next bigger values for d_{cleft} produce significantly smaller values for impedance. For cleft heights d_{cleft} of 100 nm and above all the curves are almost identical and converge.

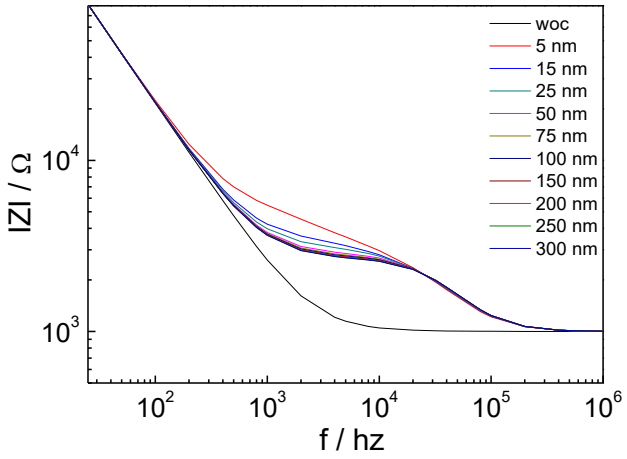

Fig. 4-19 shows the frequency-dependent impedance calculated for cell covered electrodes using the ECIS model and the parameter values as detailed in **Table 4-2**. The black curve describes impedance spectrum of the cell free electrode (woc).The legend indicates the height of the cleft **d_{cleft}** between lower cell membrane and electrode surface.

The sensing AC frequency for time resolved impedance measurement in subsequent studies addressing the signal transduction of GPCRs was empirically set to 32 kHz in all experiments. Accordingly, the impact of the cleft height d_{cleft} on the impedance at this monitoring frequency is of interest. The graph below shows the impedance at a monitoring frequency of 32 kHz when the cell height is varied according to Table 4-2. This relationship will be used later to interpret the GPCR assays.

Fig. 4-20 shows impedance calculated at 32 kHz as function of distance between substrate and cell (d_{cleft}). For the starting value d_{cleft} = 5 nm the impedance has a value of 1938 Ω. The next higher value shows an increase of 22 Ω (d_{cleft} = 15 nm; IZI = Ω 1960). The next higher

value shows an increase of 9 Ω (d_{cleft} = 25 nm; IZI = Ω 1969). The impedance increase gets smaller with a rising d_{cleft}, and reaches a value of 1985 Ω for a distance d_{cleft} = 100 a value. Further increase of d_{cleft} show no more significant impedance change till the last value (d_{cleft} = 300 nm; IZI = 1986 Ω). The increase of d_{cleft} between 5 – 100 nm shows a significant increase of the impedance, further increase of d_{cleft} shows no significant change for the impedance value.

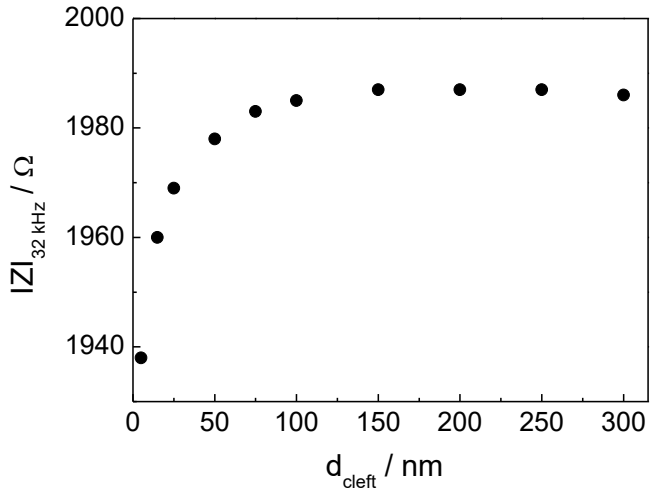

Fig. 4-20 shows the impedance magnitude at a monitoring frequency of 32 kHz plotted against substrate to cell distance (d_{cleft}). d_{cleft} indicates the distance from substrate to the lower side of the cell. Impedance data was simulated for the parameter sets that are detailed in **Table 4-2**.

Fig. 4-21 shows impedance calculated at 32 kHz as function of α. According to Eq.15, increasing distances d_{cleft} correspond to reduced values of α. The first 4 values of α describe nearly a plateau till α = 2.35 $\Omega^{0.5}$cm with an impedance value of 1987 in average. For α values of 2.35 $\Omega^{0.5}$cm (IZI = 1985 Ω) and bigger the impedance declines nearly linear to the final value of α (α = 10.49 $\Omega^{0.5}$cm) with a corresponding impedance of 1938 Ω. The rising value of α show for the first 4 values no significant change of the impedance value, as further increase of α leads continuously smaller impedance values.

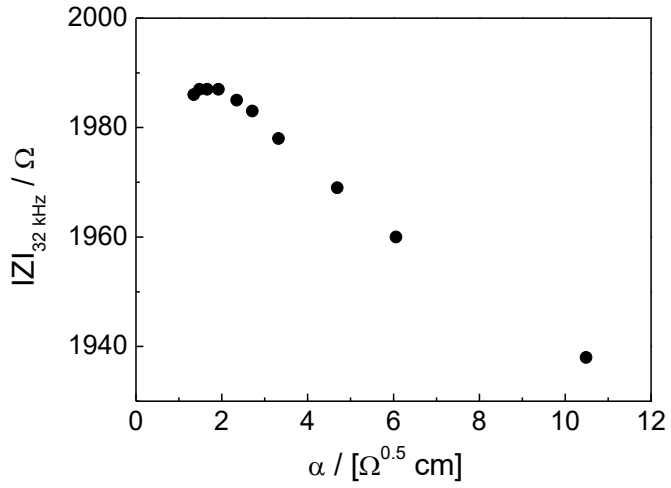

Fig. 4-21 shows the impedance magnitude at a monitoring frequency of 32 kHz plotted against α, when the distance cell to substrate (d_{cleft}) gets increased and therefore the α value gets smaller. The y-axis is calculated for α according to Eq. 15 and **Table 4-2**.

4.2.2.3 *Variation of the resistive pathway around the cell (R_b)*

The frequency scans for the individual values of R_b are plotted in Fig. 4-22. The parameter of interest R_b accounts for the resistive pathways around the cells. The parameter α is fixed with the corresponding d_{cleft} (d_{cleft} = 100 nm, α = 2.35 $\Omega^{0.5}$cm, Table 4-2, row No. 6) and the C_m value is also fixed to C_m = 1 µF/cm² (Table 4-2). The impedance spectrum of the cell free electrode (w/o c) is the lowermost curve (black). Cell-covered electrodes show higher impedance values at all frequencies. An Increase of the R_b value produces continuously higher impedance values at all frequencies.

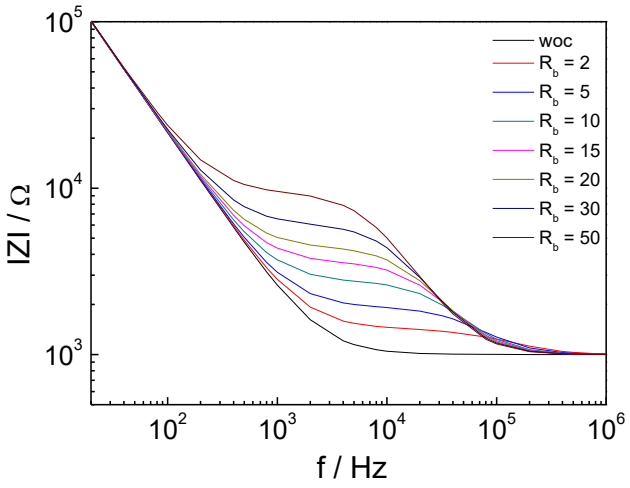

Fig. 4-22 shows frequency-dependent impedance magnitude calculated for cell covered electrodes using the ECIS model and the parameter values as detailed in **Table 4-2**. The black curve describes impedance of the cell free electrode scan (w/o c). The legend indicates the R_b value that accounts for the resistive pathway between the cells.

Fig. 4-23 shows the impedance magnitude calculated for an AC sensing frequency of 32 kHz as function of value of R_b. For the starting value of R_b = 2 Ωcm², the impedance has a value of 1380 Ω. The next higher R_b-value increases the impedance by 331 Ω (R_b = 5 Ωcm²; IZI = 1711 Ω). The third value leads to an impedance increase of 274 Ω (R_b = 10 Ωcm²; IZI = 1985 Ω). The impedance increases further with an increase of R_b to a value of 2073 Ω (R_b = 15 Ωcm²; IZI = 2073 Ω) and reaches with the next data point a maximum of impedance (R_b = 20 Ωcm²; IZI = 2098 Ω). Impedance gets then smaller and decrease with a further increase of R_b to the last point (R_b = 50 Ωcm²; IZI = 2045 Ω). Increasing the value of R_b (R_b = 2 - 20 Ωcm²) shows significant increase of the impedance, as further increase of R_b leads to a slightly decrease of impedance.

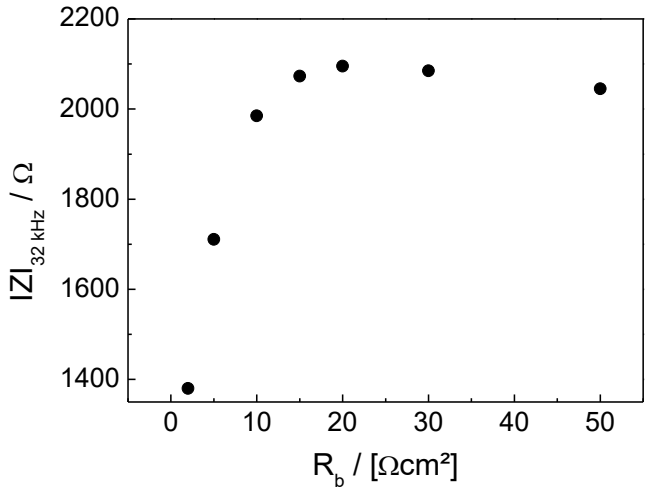

Fig. 4-23 shows the impedance magnitude at a monitoring frequency of 32 kHz plotted against R_b. R_b indicates the resistive pathway between the cells. The parameters used in the simulation are summarized in **Table 4-2**.

4.2.2.4 *Variation of the dielectric properties of the plasma membrane (C_m)*

The frequency scans for different values of C_m are plotted in Fig. 4-24. The capacitance C_m expresses the dielectric properties of the plasma membrane in quantitative terms. The parameter α (α = 2.35 $\Omega^{0.5}$ cm) is fixed with the corresponding d_{cleft} = 100 nm (Table 4-2 row No. 6) and the R_b value is also fixed to (R_b = 10 Ωcm²). The impedance spectrum of the cell free electrode (w/o c) is the lowermost curve (black). Cell-covered electrodes show higher impedance values at all frequencies. The bigger the C_m value, the smaller the impedance value for frequencies bigger than 10 kHz. The smallest values for C_m = 0.75 µF/cm² show the biggest impedance value at all frequencies. Increasing the C_m value produce a decreases off the impedance value.

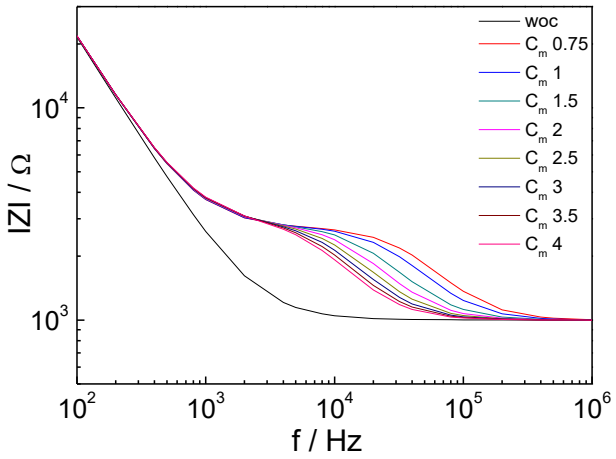

Fig. 4-24 Frequency-dependent impedance magnitude calculated for cell-covered electrodes using the ECIS model and the parameter values as detailed in **Table 4-2**. The black curve describes the impedance of the cell free electrode (w/o c). The legend indicates the capacitance C_m that represents the dielectric properties of the plasma membrane.

Fig. 4-25 shows impedance calculated at 32 kHz as function of the plasma membrane capacitance C_m. For the starting value C_m = 0.75 µF/cm² the impedance has a value of 2187 Ω. For the next higher value of C_m the impedance shows a decrease of 202 Ω (C_m = 1 µF/cm²; IZI = 1985 Ω). For the third value of C_m impedance shows a decrease of 305 Ω (C_m = 1.5 µF/cm²; IZI = 1985 Ω). For the fourth value of C_m impedance shows a decrease in impedance of 305 Ω (C_m = 2 µF/cm²; IZI = 1485 Ω). Any further increase of C_m leads continuously to smaller impedance values, but the slope of the relationship declines, to the last value of C_m (C_m = 4 µF/cm²; IZI = 1181 Ω).

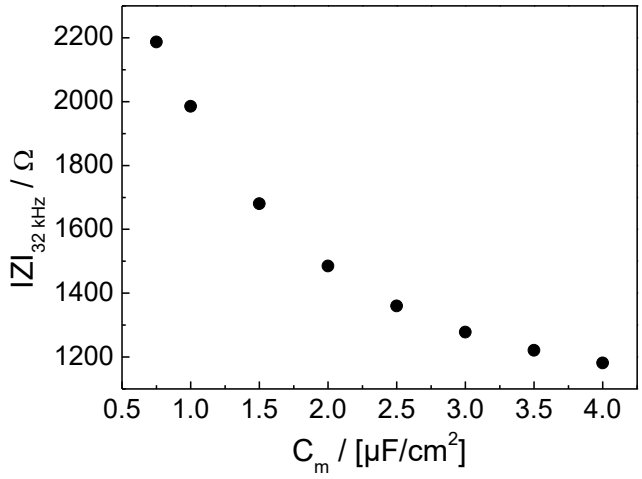

Fig. 4-25 shows the impedance magnitude at a monitoring frequency of 32 kHz plotted against C_m. C_m indicates the dielectric properties of the plasma membrane of the cell. The parameters used in the simulation are summarized in **Table 4-2**.

4.2.2.5 *Discussion*

Fig. 4-26 summarizes three parameters of the ECIS model which have been varied in this calculation. The parameter α represents the impedance of the cleft between substrate and cell including the parameter d_{cleft} (Table 4-2, Eq. 15). The parameter C_m indicates the capacitance of the cell membrane and R_b indicates the resistive pathway between the cells. Fig. 4-26 shows the impedance magnitude at a monitoring frequency of 32 kHz plotted against the values of the three model parameters α, C_m and R_b that have been normalized to their reference values, according to Table 4-2 (row No. 6). Variation of parameter α shows on either side a minimal influence on the impedance value. Increasing the α value (indicates decreased d_{cleft}) or decreasing α (indicates increased d_{cleft}) induces no significant impedance change at a monitoring frequency of 32 kHz. The parameter C_m indicates for increasing values a continuously declining impedance value. The maximum impedance change from the first to last value of C_m is 1006 Ω. C_m indicating the biggest impedance change observed for the for the three model parameters. The plot for R_b shows for reduced values (compared to the normalized standard value 1, blue curve) an intensive impedance decrease, while increasing R_b induces only a minor impedance increase.

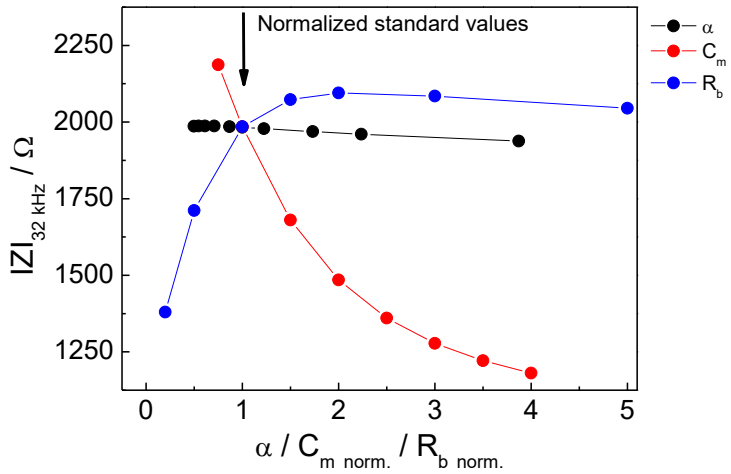

Fig. 4-26 shows a combination of Fig. 4-21, Fig. 4-23 and Fig. 4-25. It summarizes the dependence of the impedance at an AC frequency of 32 kHz for the model parameters α, C_m, R_b normalized to their individual reference values (**Table 4-2** row No. 6). The full set of parameters as used in this study is summarized in Table 4-2.

This simulation of a cell layer adhered to a noble metal electrode was simulated using the ECIS model. Results indicate minor effects of the cell to substrate cleft (α). Increasing the value of C_m in this simulation indicates a higher capacitance of the membrane according to this simulation, what causes a smaller impedance value. Changing the R_b value to lower numbers, referring to the normalized standard value, indicates less tight cell-cell contacts and thus

smaller impedance values. Increasing the R_b value relative to the reference state normalized does not lead to significant impedance increase.

4.2.3 Discussion

Comparing SPR and ECIS simulation provides an overview of which cellular structures may contribute to either signal. It has been the idea of this chapter to theoretically analyse the cellular contributions to the readout parameters in order to interpret the GPCR studies which are the core of the current thesis. By recording and analysing time series recorded with both techniques, the extra information acquired by using two readouts may help to deconvolute the holistic signals. As the SPR reaches into the system under study with a penetration depth of maximum 100-200 nm, the information in the SPR channel is limited to those parts of the cell body that are close to the growth surface including the cell-surface junction. The main influences are the composition of the electrolyte-filled cleft between lower cell membrane and surface and all structural components inside this interfacial region. Changes within the cell induced by an outside stimulus like media exchange or receptor activation are only visible in SPR as long as they affect any structure or composition in the lower part of cell body including the cell-surface junction. The SPR simulation has shown that the main effect on reflectivity change and the value of the angle of minimum reflectivity are induced by n_{cleft} and n_{cyt} within 50-150 nm from the surface (Fig. 4-18) while n_{mem} has only a minor influence. Changes within the cytosol of the cell and the composition of the cleft between substrate and cell membrane have major influence on the signal when the cell is close to the substrate within 10 – 200 nm. Literature studies on SPR simulations, with constant sample layers thickness (10 nm) within the evanescent field, have shown influence on reflection intensity and the angel of minimum reflection intensity by splitting the refractive index into a real and imaginary part. Increasing the real part of the refractive index for the sample layer within the evanescent field shifts the angle of minimum reflection intensity to higher values but has no effect on the reflection intensity. On the other hand an increase of the imaginary part of the refractive index of the sample layer has no effect on the angle of minimum reflection intensity but induces a loss in reflection intensity [89]. The main SPR peak angular position and intensity are highly sensitive to the optical properties of the medium within the evanescent field [71, 102].

In contrast to SPR, the ECIS signal is not confined to the surface but integrates over the entire cell body including the apical membrane. Accordingly, the simulation of impedance data included dielectric parameters of the cell beyond the cell-surface junction. The parameter in the ECIS model that gets closest to the SPR sensitivity is the parameter α which describes the impedance contributions of the cell-surface junction and which is directly correlated with the height of the cleft between lower cell membrane and surface. The ECIS simulation for a

sampling frequency of 32 kHz indicates a minor effect on the impedance magnitude for a variation of α, as seen in Fig. 4-26. The α value and the corresponding distance between substrate and cell (d_{cleft}) show the biggest frequency-dependent influence on impedance within a distance of 0 – 100 nm above the substrate and at low frequencies. A small d_{cleft} corresponds to a higher α value and does not show major effects on impedance at the frequency (f = 32 kHz) that was used in the calculations. Lower frequencies indicate a bigger influence on impedance change for d_{cleft} 100 nm and smaller (Fig. 4-19). The major effect on impedance magnitude at 32 kHz has the membrane capacitance C_m. Increasing the C_m value leads directly to a decrease of impedance (Fig. 4-25), which is proven by laws of physics, as the impedance of a capacitor is decreased with a higher capacitance of the capacitor. In the ECIS model the cell is viewed as a fixed capacitor and higher frequencies lead to a decrease of impedance as lower frequencies lead to increase of impedance as seen in Fig. 4-24. The simulation shows a big influence of the parameter R_b, which represents the resistance between the cells (cell-cell junction) on the impedance magnitude, while low frequencies show higher impedance values and high frequencies show lower impedance values (Fig. 4-22). At a frequency of 32 kHz, increasing R_b beyond the reference value shows only a minor effect on impedance readings, while lowering the R_b value leads to big impedance drop (Fig. 4-26). At a frequency of 32 kHz the biggest influences on impedance are caused by C_m and R_b but the influence of the two parameters is contrary. As the α value has a minor effect on the impedance, the influence of the cell substrate area in the ECIS simulation, at monitoring frequency, is also very small. According to this simulation the main influence on the impedance change are caused by changes in cell-cell contacts represented by the resistance between the cells (R_b). Former simulations have shown similar results where α has minor and R_b and C_m show bigger influence on impedance change [103].

The two readout approaches SPR and ECIS have their individual sensitivities and report about different aspects of the cell body. According to the results of the simulations SPR provides information of the cell-substrate area while ECIS provides information on the whole cell body, most notable from the cell-cell junctions. In this sense, they are indeed complementing each other. The combination of both techniques may provide significantly more and complementing information to interpret the time series data more thoroughly and beyond a purely descriptive perspective. When realized on one common culture substrate, they provide information of the self-same cell monolayer. The dual system provides two different readouts from one substrate and shows individually different sensitivities to the different parts of the cell body and the cell-surface junction.

4.3 Time-Resolved Analysis of Cell Adhesion

Next to the theoretical analysis, it is instructive to study the time course of cell adhesion with both readout approaches that are in the focus of this thesis: ECIS and SPR individually or in a combined setup. These studies will assist in the later analysis of GPCR-mediated response profiles.

4.3.1 SPR-Based Monitoring of Cell Adhesion

Fig. 4-27 shows continuously repeated angle scans (Fig. 4-4) with the SPR device while adhesion of MDCK II cell on an SPR gold substrate. The three dimensional plot shows the angle scans as function of time. During adhesion of MDCK II cells both, the reflectivity minimum and corresponding angle of incidence for minimum reflectivity change. The minimum angle shifts towards higher values during cell adhesion. At the start of the experiment the angle of minimum reflectivity amounts to 63.2 ° and shifts to higher values. The last angle scan shows an angle of minimum reflectivity of 65.3. The reflectivity minimum increases within the first half hour from 20 R.U. to a maximum of 185 R.U. and returns back to its starting point within 6 h. For slope mode measurements the angle of incidence is set to a fixed angle that corresponds to the biggest negative slope of the reflectivity. The full spectral information provides several parameters to describe the time course of cell adhesion.

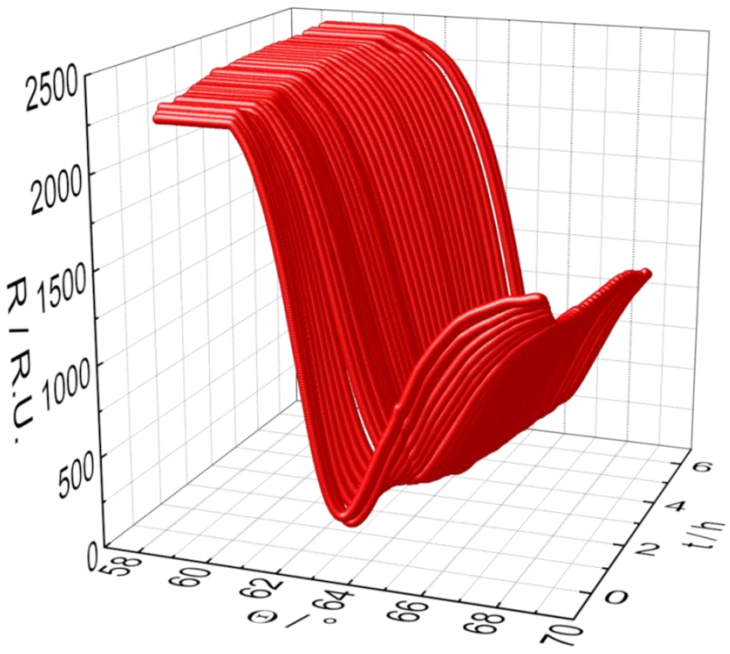

Fig. 4-27 shows a three dimensional plot of continuously repeated angle scans during adhesion and spreading of MDCK II cells that were seeded to confluence at a seeding density of 450.000 c/cm². (**Fig. 4-4**). The repeated single angle scans with the reflectivity (R / R.U.) recorded as a function of angle of incidence (θ / °) are plotted as function of time (t / h).

Fig. 4-28 shows the minimum reflectivity as extracted from repeated angle scans (Fig. 4-27) during adhesion and spreading of MDCK II cells. The graph shows the minimum of reflectivity as function of time. The data set was collected from single reflectivity scans. The minimum point of the curve combines the strongest evanescent field and largest plasmon activity and therefore a minimum of reflectivity. The reflectivity scan depends on the composition of the matter within 0 - 200 nm above the gold surface. Adhering cells on the gold surface influence the refractive index in the sensitive volume and therefore the reflectivity scan itself. The time course data is dynamic as long the cells aren't completely adhered and spread on the surface. Minimum reflectivity data starts at a minimum of 0 Δ R.U.. The intrusion of the cells into the sensitive volume of the evanescent field shifts the minimum of reflectivity upwards to a maximum of 163 R.U. 30 minutes after cell seeding (Fig. 4-28), the loss in reflectivity reaches its maximum (Δ R.U. = 163). Afterwards the reflectivity decreases continuously towards a new minimum (5 h, $R_{min.}$= -20 Δ R.U.) as the cell layer establishes on the surface. The spread cells define new static conditions within the sensitive field of the surface. After 5 h the cells show only minimal influence on the reflectivity minimum. The reflectivity is finally adjusted to a value nearly like without cells at the beginning of the experiment (Δ R.U. = 0) after complete cell adherence (7 h, R = - 12 Δ R.U.).

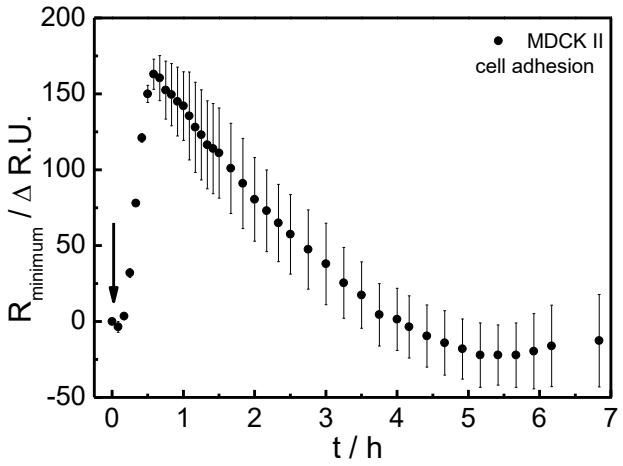

Fig. 4-28 shows the time course of the angle of minimum reflectivity during adhesion of MDCK II cells seeded at a density of 450.000 c/cm² (black arrow, cell addition) on an SPR substrate (n=2; ± SD).

Fig. 4-29 shows the angle of incidence of minimum reflectivity ($\theta_{minimum}$) as a function of time during adhesion and spreading of initially suspended MDCK II cell. At the beginning of the experiment the minimum angle amounts to 63.2 °. The angle increases within the first hour after cell seeding from 63.2 to 64.7° (Δ = 1.5°) and reaches a plateau after this time period (1 h, θ = 64.7°). Afterwards the minimum angle increases slowly by another 0.5° within the next 5 h (θ = 65.5, t = 6h). Six hours after seeding, the cells are spread and form a confluent cell

monolayer on the gold surface. When the cells are adherent, the monolayer describes a static system and the angle of incidence stays within a constant range (65.25 – 65.5 °, t = 7 h)).

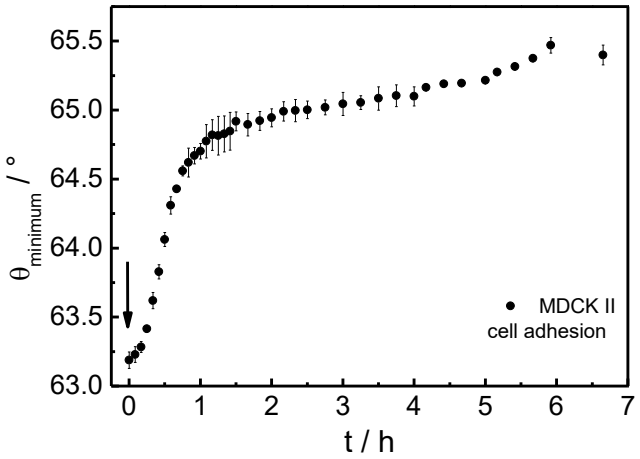

Fig. 4-29 The plot shows the angle of minimum reflectivity ($\theta_{minimum}$) as function of time during adhesion and spreading of initially suspended MDCK II cells (black arrow, cell addition) seeded in a cell density of 450.000 c/cm² (n=2; ± SD).

Fig. 4-30 shows the reflectivity at a fixed angle of 62 °during attachment and spreading of MDCK II cells seeded at time zero. The reflectivity for an angle of incidence of 62 ° starts at 1067 R.U. at time zero and reaches a value of 1775 R.U. within the first hour of recording describing the biggest gradient of the plot (t = 0-1 h, Δ R = 1067 R.U.). One hour after cell seeding the R_θ values continue to increase but at lower rates. For the next 5 hours (1 – 6 h) the reflectivity increases slightly but continuously to a value of 2227 R.U. (t = 1-6 h, Δ R = 452 R.U.) and stays nearly constant till the end (7 h, R = 2251 R.U.).

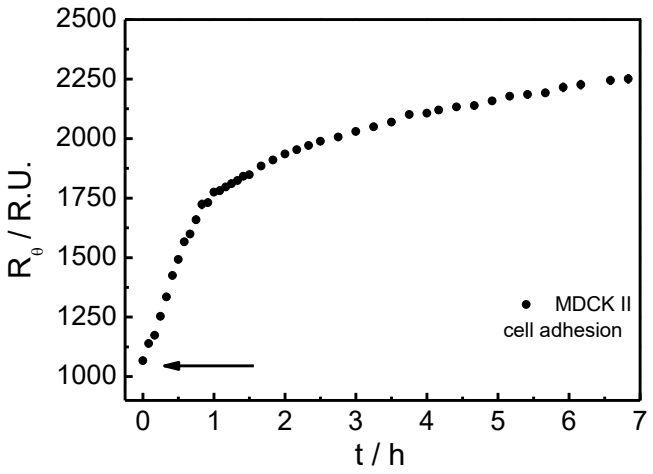

Fig. 4-30 shows the time course of the reflectivity R_θ theta during attachment and spreading of initially suspended MDCK II cells on SPR device as extracted from repeated reflectivity scans**.** Cells were seeded in a density of 450.000 c/cm² at time zero (n=2; ± SD).

4.3.2 ECIS-Based Monitoring of Cell Adhesion

Fig. 4-31 shows a 3D plot of the impedance magnitude |Z| as a function of frequency and time during adhesion of initially suspended MDCK II cell on an ECIS electrode (ECIS-SPR sensor chip $A_{Electrode}$ = 0.64 mm²). The three dimensional plot shows the impedance as function of time over the frequency range of 10 – 1000000 Hz. The cell adhesion over the recorded time period provides, depending on the frequency, different impedance values. For the lower most frequencies the impedance shows the biggest values over the whole time period (f = 10 Hz, IZI > 100000 Ω, red area of the plot). For the highest frequency values the impedance has the smallest values (f = 100000 – 1000000 Hz, IZI ≈ 265 Ω, dark blue area of the plot). The biggest change of impedance occurs in a time period between 200 – 500 minutes over the whole frequency range, with small impedance values for high frequencies and big impedance values for low frequencies. The biggest impedance change within this time period occurs mainly at a frequency of 100 – 50000 Hz. Dependent on the frequency (f = Hz) the full spectral information provides several parameters to describe the time course of cell adhesion.

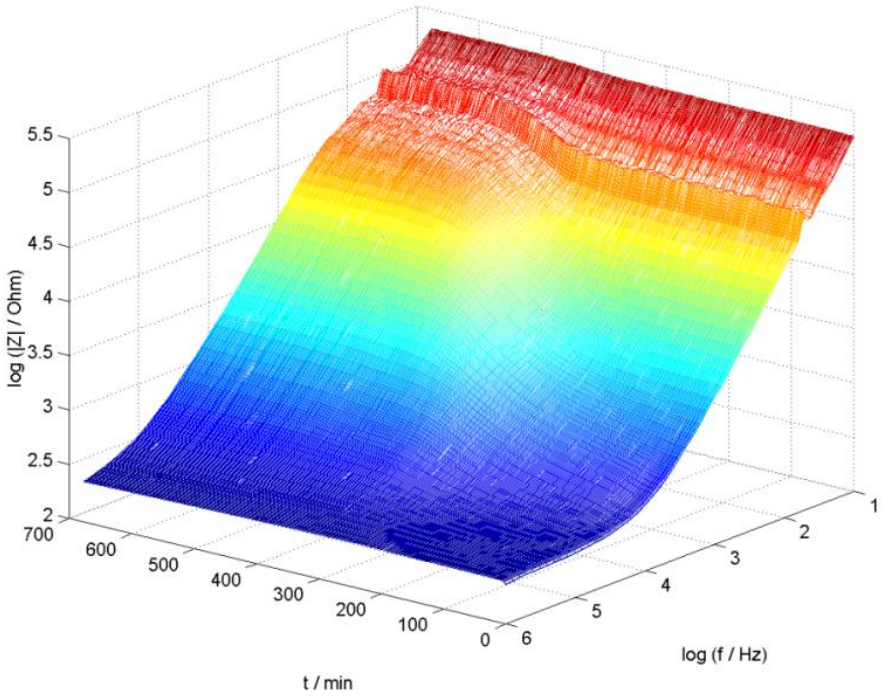

Fig. 4-31 3D plot impedance magnitude |Z| as a function of frequency and time during attachment and spreading of initially suspended MDCK II seeded upon an ECIS electrode (ECIS-SPR sensor chip $A_{Electrode}$ = 0.64 mm²) at time zero in a cell density of 450.000 c/cm². Impedance is plotted as function of time (x-axis) and frequency (y-axis).

Fig. 4-32 shows the time course of the impedance Δ |Z| at an AC frequency of 400 Hz during MDCK II cell adhesion on a gold-film electrode. The black arrow describes the cell addition on

to the electrode (ECIS-SPR sensor chip $A_{Electrode}$ = 0.64 mm²). The impedance is recorded at a frequency of 400 Hz. The recording frequency (400 Hz) monitors mainly the formation of cell-cell contacts on the gold substrate when cell adhesion on the substrate is nearly complete. At low frequencies the current has to flow around the cells as the membrane is insulating at these frequencies [104]. The time course starts at Δ $IZI_{400\ Hz}$ = 0 kΩ and doesn't change within the first 4 hours. For the next 2 hours the impedance increases by 8.4 kΩ (4–6 h). The plot describes the most intense gradient from 6 to 8 hours with an impedance increase to 32.5 kΩ (Δ $IZI_{400\ Hz}$ = 23.7 kΩ). The next hour the impedance increase slightly and rises further to a value of 35 kΩ (t = 8-9 h, Δ $IZI_{400\ Hz}$ = 2.5 kΩ) The last 3 hours of measurement (9-12 h) describe a plateau and the plot ends after 12 hours at a final value of 35 kΩ and show only minimal value changes.

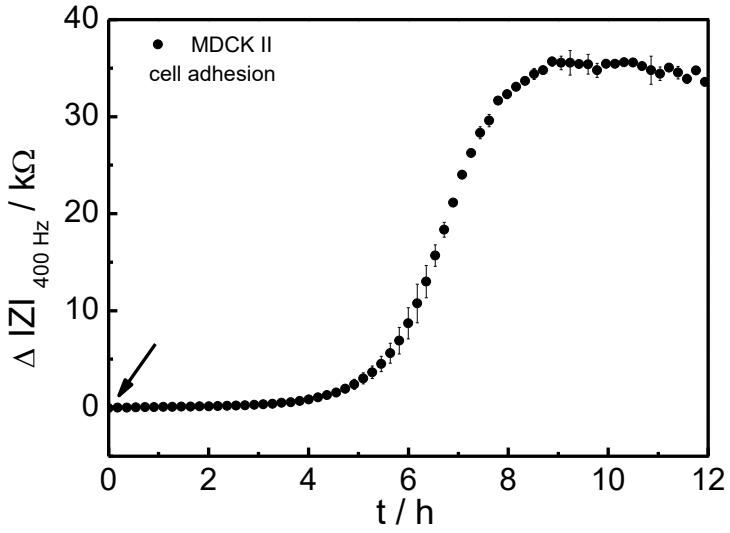

Fig. 4-32 shows the time course of the impedance magnitude Δ $|Z|_{400\ Hz}$ during attachment and spreading of MDCK II cells (n=2; ± SD) seeded in a density of 450.000 c/cm² on ECIS electrode (ECIS-SPR sensor chip $A_{Electrode}$ = 0.64 mm²) The impedance was monitored at a frequency of 400 Hz. The plot shows impedance as function of time.

Fig. 4-33 shows the time course of impedance Δ $|Z|_{32\ kHz}$ at an AC frequency of 32 kHz during MDCK II cell adhesion on a gold–film electrode (ECIS-SPR sensor chip $A_{Electrode}$ = 0.64 mm²). The black arrow describes the cell addition on to the ECIS electrode. The impedance is recorded at a frequency of 32 kHz. The recording frequency (32 kHz) monitors mainly the cell-substrate adhesion to the gold electrode. High frequencies monitor mainly the *de novo* formation of cell-matrix contacts during cell attachment and cell spreading of initially suspended cells on the substrate [104]. The time course starts at a value of zero Ω and increases within the first 3 hours by 150 Ω. For the next 2.5 hours the impedance describes the biggest gradient of the plot and increases to an impedance value of 513 Ω. (t = 3 – 5.5 h, Δ $IZI_{32\ kHz}$ = 363 Ω). The gradient gets then reduced and the impedance increases within the next 2.5 hours for further 130 Ω (t = 8; Δ $IZI_{32\ kHz}$ = 645 Ω). The signal stays then for 4 h at a nearly constant value till the end of recording (t = 12; Δ $IZI_{32\ kHz}$ = 668 Ω).

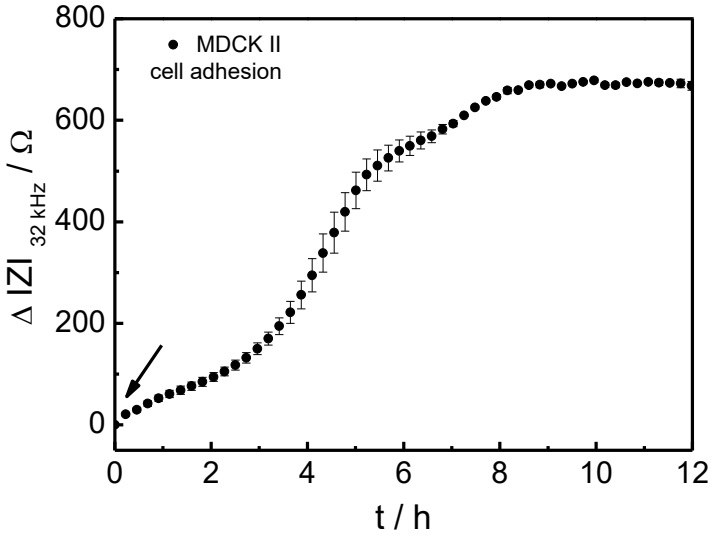

Fig. 4-33 shows the time course of the impedance magnitude at an AC frequency of 32 kHz during attachment and spreading of initially suspended MDCK II seeded in a density of 450000 c/cm² (n=2; ± SD) on a ECIS electrode (ECIS-SPR sensor chip $A_{Electrode}$ = 0.64 mm²) at time zero.

4.3.3 Monitoring Cell Adhesion by Simultaneous Recording of SPR- and ECIS- Data in one Setup

Fig. 4-34 shows the adhesion of MDCK II cells on the dual ECIS-SPR sensor. The ECIS data set (black curve) is shown at a monitoring frequency of 400 Hz and the SPR data set (red curve) is recorded in slope mode (R_θ). The measurement is a simultaneous recording by the two readouts from one ECIS-SPR sensor surface, plotted with normalized values ($IZI_{norm.}$ and $R_{norm.}$) as the maximum values are considered as 1 (100%). The signal of the SPR readout (red curve) decreases within the first half hour of baseline recording before the cell addition (black arrow) by 0.04 $R_{norm.}$. After cell addition (t = 0.5 h; $R_{norm.}$ = 0.002; black arrow) the reflectivity starts increasing immediately for 1.5 h with a rather constant rate describing a reflectivity increase of 0.6 $R_{norm.}$. After 2 hours the signal increases more slowly for the next 3.5 h (t = 2 - 5.5 h); the slope is almost constant and the reflectivity increases for further 0.28 $R_{norm.}$ ($R_{norm.}$ = 0.88; t = 5.5 h). The cells have nearly completely adhered at the sensor surface. For the rest of the recording time (t = 5.5 – 12 h) the signal increases by further 0.1 R_{norm} till the end data recording (t = 12 h; $R_{norm.}$ = 0.98). The ECIS recording of MDCK II cell adhesion (f = 400 Hz, black curve) has a stable baseline for the first half hour of recording. When the cells are added onto the sensor (t = 0.5 h; black arrow) the impedance is almost constant at zero and doesn't change within the first 3.5 hours. For the next 2 hours the impedance increases for 0.25 $IZI_{norm.}$ (t = 4–6 h). The plot describes the most intense gradient from 6 to 8 hours with a signal increase to a value off 0.89 (Δ $IZI_{norm.}$ = 0.64). The last four hours of measurement (8-12 h) describe nearly a plateau and a signal increase of further 0.07 Δ $IZI_{norm.}$. The plot ends

after 12 hours at a final value of 0.94 $IZI_{norm.}$ and show only minimal value changes. The datasets complement each other as the SPR readout records any changes within the cell-substrate junction 0 – 200 nm above the gold surface while the ECIS readout at 400 Hz records mainly the formation of cell-cell contacts on the substrate after cell adhesion and spreading on the surface.

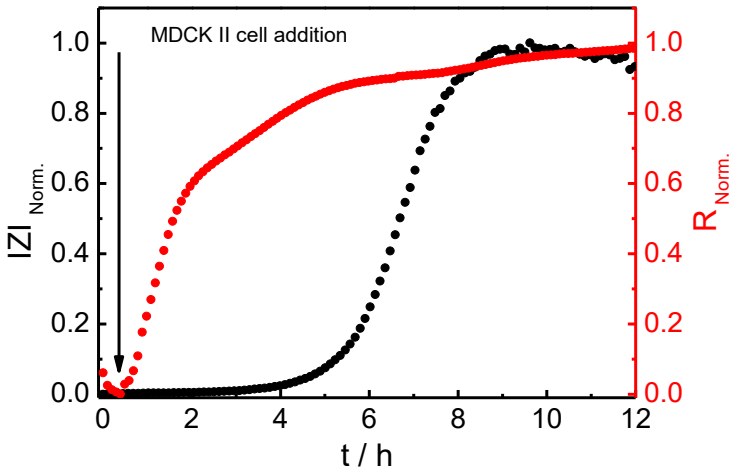

Fig. 4-34 shows the readout of the dual ECIS-SPR sensor for MDCK II cell adhesion on a combined ECIS-SPR sensor surface. Cells were seeded at a density of 450.000 c/cm².The monitoring frequency for the ECIS readout is 400 Hz while the SPR data's are recorded in slope mode.

Fig. 4-35 shows the adhesion of MDCK II cells on the dual ECIS-SPR sensor. The ECIS data set (black curve) is shown at a monitoring frequency of 32 kHz and the SPR data set (red curve) is recorded in slope mode (R_{sm}). The measurement is a simultaneously recording by the two readouts from one sensor substrate. The time course of the SPR readout has been described above. The ECIS recording of MDCK II cell adhesion (f = 32 kHz, black curve) has a minor shift in baseline for the first half hour of recording ($IZI_{norm.}$ =0.02). When the cells are added onto the sensor (t = 0.5 h; black arrow) the value the impedance starts increasing constantly for 2.5 hours (t = 3h; $IZI_{norm.}$ = 0.2). For the next 2.5 hours the impedance describes the biggest slope and increases for 0.53 Δ $IZI_{norm.}$ (t = 3–5.5 h; $IZI_{norm.}$ = 0.76). The slope of the curve gets reduced and for the next 2 hours the impedance increases for further 0.2 Δ $IZI_{norm.}$ (t = 5.5 – 8 h; $IZI_{norm.}$ = 0.96). The last four hours of measurement (8-12 h) describe nearly a plateau and a signal increase by further 0.02 Δ $IZI_{norm.}$. The plot ends after 12 hours at a final value of 0.99 $IZI_{norm.}$ and shows only minimal value changes. The datasets confirm each other as the SPR readout records any changes within the cell-substrate adhesion zone within 0 – 200 nm above the gold surface. The ECIS readout at 32 kHz is also thought to record mainly the formation of cell-substrate adhesion and cell spreading. However, the impedance starts increasing with some delay compared to the SPR readout. The main signals increases are shifted but reach both a plateau at 8 h in average, when the cells have adhered at the gold

surface of the sensor as both readouts record the cell-substrate and cell spreading on the surface.

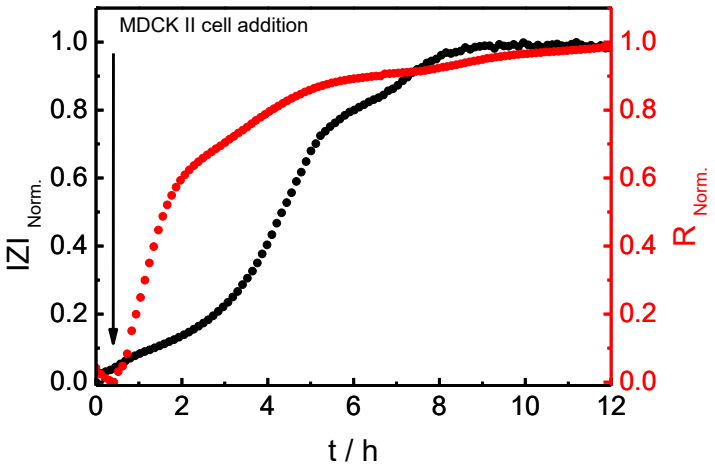

Fig. 4-35 shows the readout with the dual ECIS-SPR sensor for MDCK II cell adhesion on a combined ECIS-SPR sensor substrate. The monitoring frequency for the ECIS readout is 32 kHz while the SPR data's are recorded in slope mode. Cells were seeded in a density of 450.000 c/cm² at time 0.5 h.

Fig. 4-36 is a combined plot of Fig. 4-34 and Fig. 4-35 and shows clearly the difference for MDCK II adhesion recorded at different frequencies. The impedance at 32 kHz (blue curve) reports mainly the formation of cell-substrate adhesion and cell spreading while the impedance at 400 Hz (black curve) reports mainly the formation of cell-cell contacts on the substrate after cell adhesion and spreading on the surface. The plot shows a cross section of plot Fig. 4-31 at the two different frequencies and illustrates the differences for impedance recording at different frequencies.

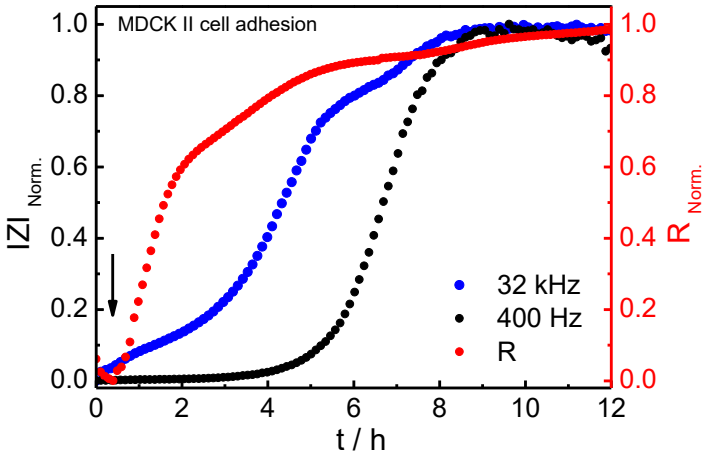

Fig. 4-36 is a combined plot **Fig. 4-34** and **Fig. 4-35** showing the impedance time course at two monitoring frequencies of 32 kHz (blue curve) and 400 Hz (black curve) while the SPR data's (red curve) are recorded in slope mode. Cells were seeded in a density of 450.000 c/cm² at time 0.5 h.

4.3.4 Discussion

The SPR device offers two different readout modes: (i) the slope mode in which the angle of incidence is determined with the first angle scan at the beginning of the measurement and is then fixed. The reflectivity is recorded at an angle of incidence that provides the biggest slope of the reflectivity for changing resonance angles (Fig. 4-4). (ii) Continuously recorded angle scans show the shift of the reflectivity minimum and the corresponding angle of incidence over the time during an experiment. The adhesion of MDCK II cells on the sensor surface show a shift of the reflectivity minimum and the corresponding angle of incidence as cell adhesion progresses. The full spectral information provides several parameters, and therefore it is possible to extract different time dependent courses of the cell adhesion (Fig. 4-27).

For continuously repeated angle scans the first possibility is to plot the reflectivity minimum ($R_{minimum}$) of the angle scan as function of time (Fig. 4-28). This plot shows the biggest increase of the reflectivity minimum within the first 30 minutes which indicates that the cells have reached the evanescent field within this time period. The reflectivity minimum then decreases for 4.5 hours after this maximum. The minimum reflectivity is considered as a measure for the inhomogeneity of the surface load. During cell attachment and spreading the ensemble of cells does not change their adhesion status in perfect synchrony so that inhomogeneity close to the surface increases and then decreases. This plot indicates that when the cells have built up a confluent monolayer no changes occur within the evanescent field anymore and therefore no changes for the reflectivity minimum are recorded. The next plot shows a similar result when the angle of minimum reflectivity is plotted against time while MDCK II cell adhesion on the surface (Fig. 4-29). Within the first hour the cells induce the biggest shift on the angle of incidence towards higher values, which indicates arrival of the cell bodies in the evanescent field and adhesion to the surface. For the rest of the recording time the angle increase only slowly to little higher values, which indicates cell spreading. The time dependent plot of the angle of incidence show, that the main signal change happens when the cells reach the sensitive area of the evanescent field and attach on the surface while the cell spreading has minor influence on the shift of the angle of incidence to higher values. The biggest increase of the angle of incidence is also supported by the results of the SPR simulations (Fig. 4-18, B, D, F), which indicate the biggest influence of the refractive index change in the cleft (n_{cleft}) between substrate and cell. The volume flooded by the evanescent field experiences the biggest changes while cell adhesion on the substrate. The next plot, extracted from continuously repeated angle scans, support these results. When the reflectivity is extracted at a fixed angle (R_θ) the corresponding reflectivity can be plotted against time (Fig. 4-30). The results show the biggest reflectivity increase within the first hour followed by slight increase of reflectivity for the rest of the recording time. The repeated angle scan mode provides mainly

two pieces of information. Reflectivity minimum plotted as function of time has the advantage to record at the most sensitive angle and the reflectivity scan indicate therefore how fast the cells reach the sensitive area of the surface and change the refractive index within the evanescent field which is supported by the result of the SPR simulation (Fig. 4-18, A, C, E). The cell adhesion and spreading goes along with a changes reflectivity minimum. The plot of the R_θ against time and the plot $\theta_{minimum}$ against time show a slower signal answer to the cell adhesion compared to the $R_{minimum}$ plot against time. Studies have shown MDCK II cell adhesion on SPR devices in slope mode [78]. The recording with repeated angle scans confirms the results and ad further analysing possibilities. For both readout modes the cell adhesion does not show any further signal changes after 7 hours what indicates an established confluent cell monolayer on the surface with established cell-matrix contacts. The angle scan mode offers by different plotting methods additional time course of cell adhesion/spreading. The $R_{minimum}$ plot shows the fastest signal answer and indicates how fast the cells reach the evanescent field of the substrate, while the signal for R_θ and the θ/° plot indicate a slower answer of the cells reaching the surface. The SPR itself has no possibility to monitor specifically the cell-cell contact formation due to the small penetration depth of the evanescent field (0 – 200 nm).

The ECIS readout offers over the whole recorded frequency range different analytical possibilities to plot the impedance change on the substrate during cell adhesion and indicates different situations during cell adhesion, spreading and *de novo* building of a new confluent cell layer (Fig. 4-31).

Plotting the impedance against time at low frequencies (f = 400 Hz) shows mainly the formation of cell-cell contacts [104] and therefore impedance change/increase 4 hours after cell addition (Fig. 4-32) which have been reported by literature [78]. Plotting the impedance at high frequencies (f = 32 kHz) shows immediately changes of impedance as there are mainly cell-substrate contacts monitored [104]. The addition of suspended cells onto an ECIS substrate, induce an impedance increase compared to a cell free substrate at 32 kHz (Fig. 4-22, Fig. 4-24). The impedance plot and increase at high frequencies can be better understood by a look at the impedance plot at low frequencies. Fig. 4-33 (f = 32 kHz) shows a light increase while the first 3 hours, which can be related gradual coverage of the electrode with the cell bodies – not yet spread. The impedance increases then stronger for the next 3 hours which can be related to cell spreading and formation of a confluent cell layer. The R_b value contributes to the final slight impedance increase from 6-9 hours, which is supported by the plot of impedance against time at low frequencies which indicates the cell-cell contact formation. High frequency ECIS recordings therefore contain mainly information on cell-matrix contact formation during cell adhesion and to a lesser degree information on cell-cell

interaction. These differential sensitivities are the explanation for the stepwise impedance increase.

The readout with the dual ECIS-SPR sensor offers the readout from one substrate and an overlay of the signal patterns. The SPR signal is the same for the two plots (Fig. 4-34, Fig. 4-35) and shows within 1.5 hours the biggest signal increase followed by a smaller signal increase for the next 3.5 hours when the cells have settled on the substrate, as confirmed by literature data [78]. The majority of the signal increase happens within the first 5 hours. The signal increase can be described as adhesion (cell-matrix interaction) followed by cell spreading (cell-matrix and cell-cell interaction) on the substrate which has been described in detail before [59]. The plot in Fig. 4-36 illustrates the differences for the impedance recording at different frequencies (32 kHz and 400 Hz) and therefore the monitoring of different properties of a maturating cell layer. The SPR is blind for cell-cell contact formation as the penetration depth of the evanescent field is only 0 – 200 nm. The ECIS readout at 400 Hz is nearly blind for the cell matrix interactions and mainly shows cell-cell contact formation. The main impedance increase happens between 5 and 9 hours of recording. The impedance at both monitoring frequencies shows only minor signal changes after more than 9 hours. This plot shows that the two label-free readout systems are sensitive for different phases of cell adhesion/spreading on one substrate. The SPR signal in one plot with ECIS recording at 32 kHz provides similar signal pattern, since the ECIS signal shows cell-matrix interaction at high frequencies [104]. The impedance at 32 kHz shows the main signal increase from 0 – 6 hours, which reports on cell adhesion and spreading thus therefore cell-matrix interaction. The impedance increase at 32 kHz between 6-9 hours indicates cell-cell interaction and rearrangement of the cytoskeleton of the *de novo* built cell monolayer but contributes only small impedance increases to the whole signal. The SPR signal supports the signal interpretation for the high frequency recording but the signal increase of the impedance at 32 kHz occurs later compared to the SPR signal.

ECIS and SPR have different recording modes and depending on which recording mode is used the signal provides different information. The ECIS reports mainly on cell morphology while SPR indicates the cell-substrate interactions of a maturating cell layer on a combined substrate. The two label-free approaches differ with respect to their penetration depth into the cell body but a combination of the holistic techniques (ECIS-SPR) provides more opportunities on signal pattern interpretation.

4.4 Label-free Analysis of GPCR-Mediated Signal Transduction

Label-free analysis of GPCR-activation and GPCR-mediated signal transduction has received increasing acceptance in the scientific community. It provides unbiased, time-resolved analysis of the cell response to receptor activation and it allows for in-depth signal transduction studies. It is the strength of these approaches to provide an integral readout of the cell response that is independent of the signalling cascade involved. This intrinsically wholistic nature is, however, also a big disadvantage since a deeper understanding of a particular GPCR's involvement in physiology and disease requires precise knowledge of the downstream processing. It is the aim of this chapter to identify the potential of label-free monitoring in the context of GPCR research on the example of two different GPCRs: the human histamine H1 receptor and the human dopamine D2 receptor. Whereas the former is expressed endogenously in the human glioblastoma cell line U-373MG, the latter has been stably transfected in CHO cells in two isoforms. From the methodological side, label-free analysis will be based on electrochemical impedance measurements on the one hand and evanescent field-based optical approaches (SPR and DMR) on the other.

4.4.1 Human Histamine H_1-Receptor (hH_1R)

Four different histamine receptor subtypes have been identified in the human genome that are consecutively numbered: H_1R to H_4R. This study addresses the pharmacology of the endogenously expressed $_hH_1$ receptor. U-373 MG cells express endogenously the $_hH_1$ receptor which is $G_{\alpha q/11}$-coupled. The activation of the receptor by the endogenous agonist histamine leads to an increase of the concentrations of cytosolic Ca^{2+}, inositol-1,4,5-triphosphate and diacylglycerol (DAG). The response of U-373 MG cells where studied under different assay conditions.

4.4.1.1 Dose-Response Analysis for Endogenous or Synthetic Receptor Agonists

The $_hH_1$ receptor has been studied by both, time resolved electrochemical impedance measurements and SPR analysis in slope mode.

Endogenous Agonist Histamine

Fig. 4-37 shows a recording during stimulation of U-373 MG cells with histamine on the dual ECIS-SPR sensor. Figure (A) shows the SPR response (slope mode) of U-373 MG cells to an increasing concentration of histamine and the corresponding ECIS (f = 32 kHz) (C) response is shown in (B). All results represent single experiments. The SPR signal shows for histamine concentration of 0.6 µM and higher a biphasic signal pattern. The first maximum peak occurs at 2 – 2.5 minutes with increasing Δ R.U. values (maximum peak) going along with increasing histamine concentrations. The second maxima / shoulders occur at 10 minutes in average. Maximum histamine concentrations of 3 and 10 µM reach a first maximum of 300 Δ R.U. Plotting the peak values for the time courses as a function of the logarithm of the histamine concentration, a sigmoidal curve is obtained providing an EC_{50} value of (0.54 µM ± 0.04) µM histamine (B). The impedance at an AC frequency of 32 kHz (C) shows a first signal drop with a minimum at 1.25 – 1.5 min for concentration of 0.6 µM histamine. The impedance decrease by a maximum of minus 20 Ω. The signal increases to values of 90 Ω for histamine concentration higher than 0.6 µM after 15 min, in average. The signal patterns are isomorphous and show higher Δ IZI values with increasing histamine concentrations. When the maximum impedance changes Δ IZI were determined and plotted as a function of the logarithm of the histamine concentration, a sigmoidal curve provided an EC_{50} value of (0.48 ± 0.05) µM histamine (Fig. 4 27 D).

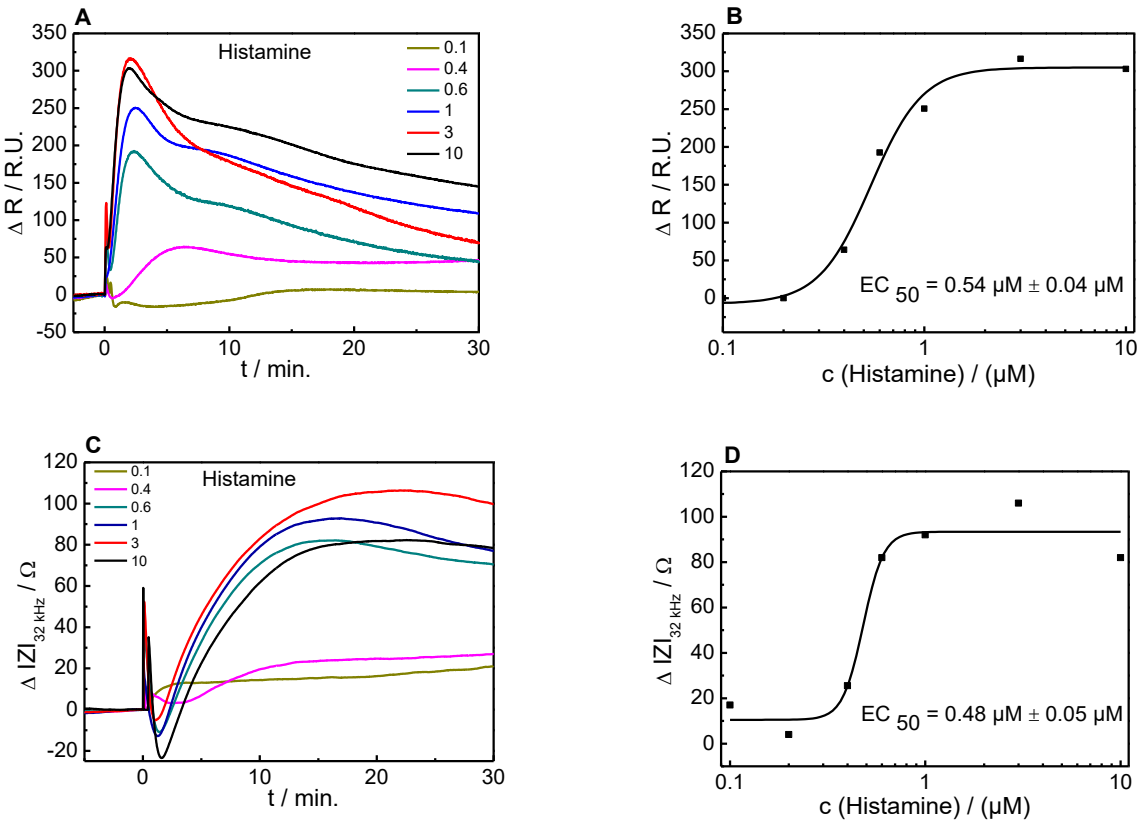

Fig. 4-37 shows the recording of confluent U 373 MG cells stimulated with histamine (c = µM) on the dual ECIS-SPR sensor. **A** shows the SPR recording (slope mode) with the corresponding EC_{50} value determination **B**. **C** shows the ECIS recording (f = 32 kHz) with the corresponding EC_{50} value determination **D**. The results represent single experiments.

SPR-based monitoring of GPCR assays is currently limited by a very low throughput in our laboratory. The instrumentation does not allow following more than two samples in parallel which makes it very tedious to establish dose-response relationships and it requires combining experiments that have been recorded on different days which is often associated with a different age of the cells. An alternative dosing protocol has been described just recently [105] and provides a massive improvement for the throughput. Instead of applying every single dose of a GPCR agonist to a fresh cell population, increasing concentrations are applied in series yielding to accumulation of the agonist in the experimental buffer. This protocol has been applied to both, impedance- and SPR-based monitoring of receptor activation. Fig. 4-38 shows the increasing histamine addition on one cell layer on the dual ECIS-SPR sensor. The duration of the experiment was 150 minutes and the histamine concentration was increased from 0.003 to 100 µM within 10 steps. The reaction chamber has an absolute volume of 300 µL. The cells where incubated in 250 µL L 15 medium before the experiment begun. 125 µl of L 15 media was aspirated out of the reaction chamber and 125 µl of L15 medium including the necessary histamine concentration was added. The histamine was added in twofold concentrations to establish the nominal concentration in the experimental buffer. The total volume amount in the chamber was 250 µL. 12 minutes after histamine addition 125 µL got aspirated out of the

reaction chamber to have space for the next addition of histamine in L15. Three minutes later, in sum 15 minutes after the first histamine dose, the next higher concentration was applied. The method development was performed using SRP readout only due to easier handling without the connecting wires for the ECIS readout on the sensor. After the ideal application method was discovered, the dual ECIS-SPR sensor was used to perform the experiment. Fig. 4-38 shows a single experiment and illustrates the continuous signal increase serial dosing of increasing histamine concentrations for the SPR readout (A, slope mode). Figure B shows the corresponding dose-response relationship including the resulting EC_{50} value of (0.96 ± 0.13) µM histamine. The reflectivity increased continuously from zero to 250 R.U. within 115 minutes which means 10 times increasing histamine (µM) addition. The final value after 150 minutes was Δ R=180 R.U. (addition of 10 increasing histamine concentrations). Fig. 4-38 C is the simultaneously recorded ECIS readout of the experiment. The aspiration of the medium showed a small signal increase every time. The medium removal had a small impact on the response pattern of the ECIS readout while the SPR signal showed no response during aspiration of the 125 µL before next histamine addition. The influence of the medium removal had no effect on the dose response determination. The Δ IZI value started at zero and increased to a value of 82 Ω after 10 times addition of increasing histamine concentration (115 min). The final value is 75 Ω after 150 min. D is the corresponding determination of the EC_{50} value (0.70 ± 0.10) µM histamine. The histamine induced signal increase was in both cases (ECIS and SPR) additive and provided meaningful EC_{50} values.

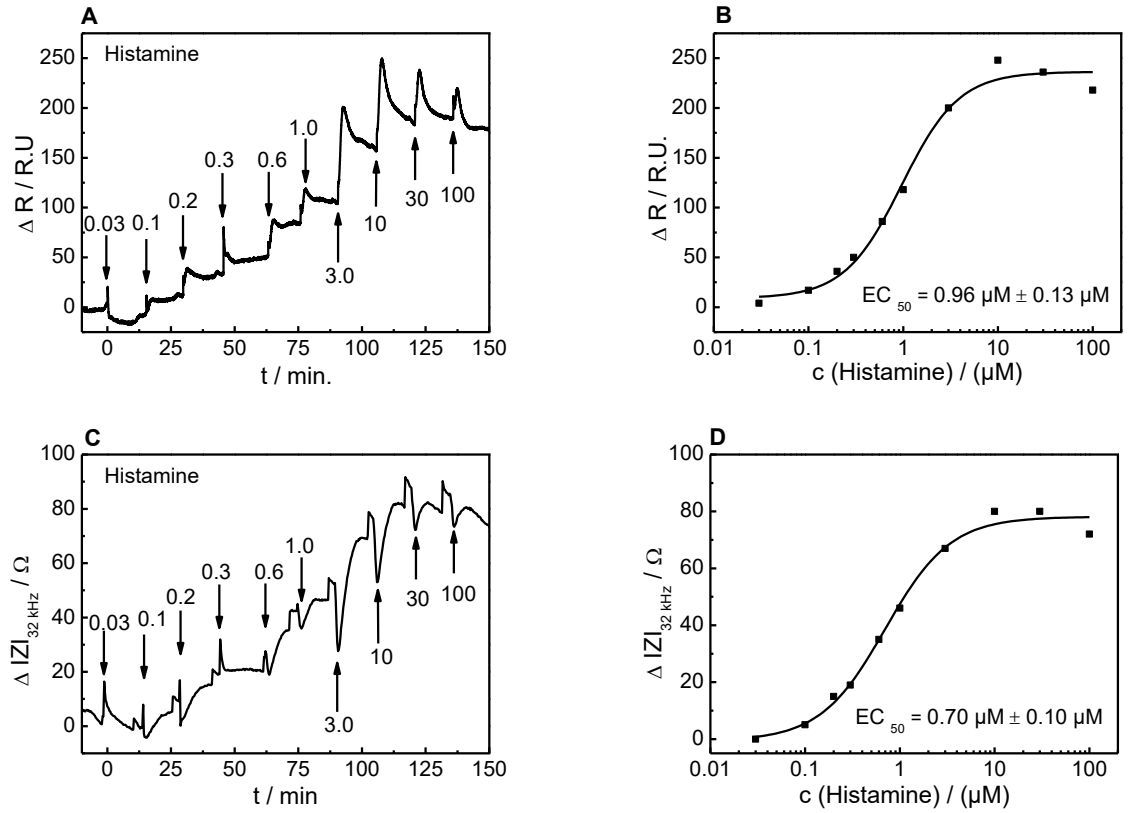

Fig. 4-38 shows the simultaneous readout of U-373 MG serially exposed to increasing histamine concentrations (c = µM) on the dual ECIS-SPR sensor. **A** shows the SPR answer (recorded in slope mode) and **C** shows the ECIS readout (f = 32 kHz). **B** (SPR) and **D** (ECIS) are the corresponding dose-response relationships used to calculate EC_{50} values. The results represent single experiments.

The experiment was repeated 4 times on the dual ECIS-SPR sensor and the corresponding EC_{50} values for SPR readout have been averaged to (1.08 ± 0.23) µM histamine (n=4) and to (0.79 ± 0.10) µM histamine (n=4) for the ECIS readout. Both approaches showed a reliable reproducibility.

Synthetic Agonist UR-KUM 530

Besides the endogenous agonist of the $_hH_1R$ the synthetic analogue KUM-530 has been studied by similar label-free assays. KUM-530 has been described as a superagonist, i.e. the response of the cell to receptor stimulation is even stronger compared to the endogenous histamine. Fig. 4-39 shows a recording during stimulation of U-373 MG cells with UR-KUM 530 on the dual ECIS-SPR sensor. The SPR response (slope mode) of U-373 MG cells to an increasing concentration of UR-KUM 530 is shown in (A) and the corresponding ECIS profile (f = 32 kHz) is shown in (C). The results represent single experiments. The SPR signal shows for UR-KUM 530 concentrations of 0.3 µM and higher a maximum peak at 2.5 minutes and increasing Δ R.U. values (maximum peak) with increasing UR-KUM 530 concentrations. Maximum UR-KUM 530 concentrations of 0.3, 1 and 3 µM induce a reflectivity increase from 0 to 270 R.U. (0.3 µM), 360 R.U. (1 µM) and 327 R.U. (3 µM). The peak values for the time

courses were extracted and plotted as a function of the logarithm of the UR-KUM 530 concentrations, providing a sigmoidal curve with an EC_{50} value of (0.12 ± 0.03) µM UR-KUM 530 (B). The time course of the ECIS response (C) shows an initial signal drop with a minimum at 1.9 min and an ΔIZI minimum of – 20 Ω for 0.03,1 and 3 µM UR-KUM 530 concentrations. The signal increases to values of IZI = 70 Ω for UR-KUM 530 concentration higher than 0.1 µM after 15 min, in average. The signal patterns are similar and show higher Δ IZI values with increasing UR-KUM 530 concentrations. When the maximum Δ IZI value were extracted and plotted as a function of the logarithm of the UR-KUM 530 concentration, a sigmoidal curve provided an EC_{50} value of (0.06 ± 0.03) µM UR-KUM 530 (D).

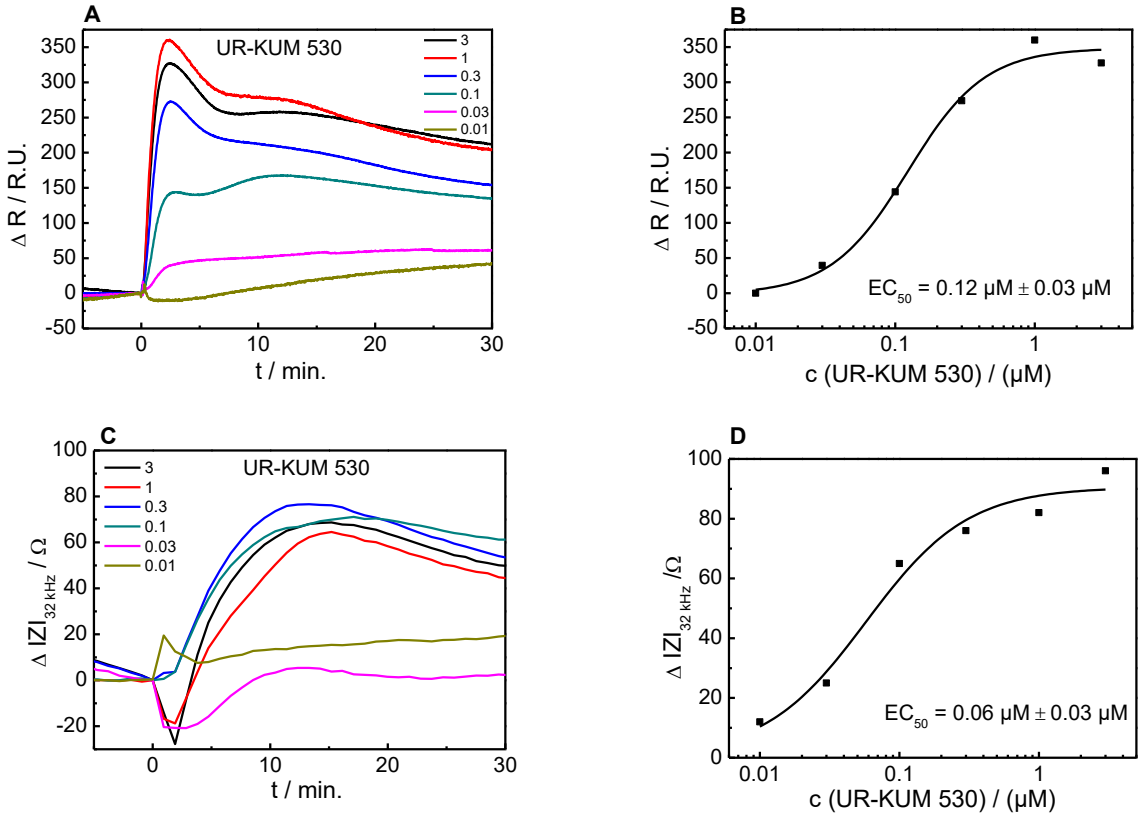

Fig. 4-39 shows the recording of U 373 MG cells during stimulation with UR-KUM 530 (c = µM) on the dual ECIS-SPR sensor. **A** shows the SPR recording (in slope mode) with the corresponding EC_{50} value calculation in **B**. **C** shows the ECIS recording (f = 32 kHz) with the corresponding EC_{50} value calculation in **D**. The results represent individual experiments.

4.4.1.2 *Deconvolution of the Signalling Cascade*

According to pharmacology textbooks, the $_hH_1$ receptor is intracellularly coupled to the $G_{\alpha q}$-dependent pathway that leads to an increase of cytosolic Ca^{2+} concentrations and the release of diacylglycerol. Both molecules are known to activate protein kinase C and the subsequent downstream signalling cascade. However, a paradigm shift has occurred throughout the last decade which is expressed in the concept of *functional selectivity* or *biased signalling*. According to this concept, a given receptor may not exclusively couple to one G-protein subtype, but it may also trigger the beta-arrestin pathway or others. The receptor's preference for any of these pathways depends on the ligand that binds to the receptor. It was therefore the aim of this study to verify by label-free means that the $_hH_1$ receptor induces an increase of intracellular Ca^{2+} concentration. This chapter aims to analyse the signalling pattern of the $_hH_1R$ using label-free cell observation.

Pharmacological Tool

The experimental strategy was based on raising the cytosolic Ca^{2+} concentration by receptor-independent means. In the subsequent experiments, the Ca^{2+} ionophore *A23187* or *Calcimycin* has been applied for this purpose. It makes the plasma membrane permeable for Ca^{2+} so that Ca^{2+} ions flush into the cells from the extracellular space and thereby mimic the release of the signalling cascade. Fig. 4-40 (A) shows the stimulation of U-373 MG cells with the agonist histamine (10 µM, black curve, n=3; ± SD) and the ionophor calcimycin (10 µM, red curve, n=3; ± SD) with the SPR device. The histamine-induced cell response increases the reflectivity from zero R.U. to a maximum peak at 2:15 min with a reflectivity of 280 R.U.. The signal decreases to 223 R.U. at 6.5 minutes and reaches after 13 minutes a second maximum of 246 R.U. The signal decreases to a value of 220 R.U. after 30 minutes. The addition of *Calcimycin* (red curve) shows a similar pattern as the histamine stimulation. The first signal increase has a smaller slope, the peak value occurs at 3:45 and maximum at 208 R.U.. The signal drops to a value of 190 R.U. after 7 minutes and increases then constantly to a value of 240 R.U. after 30 minutes. Fig. 4-40 B shows an enlargement of Fig. 4-40 A. The cell answer after *Calcimycin* addition shows a delay compared to the histamine signal. The *Calcimycin* is added to the cells and for the first 15 seconds the signal increases. The next 25 seconds the signal shows a plateau. After these 25 seconds of static behaviour the signal starts to increase and simulate the histamine signal with a delayed and smaller peak value, compared to the histamine stimulation.

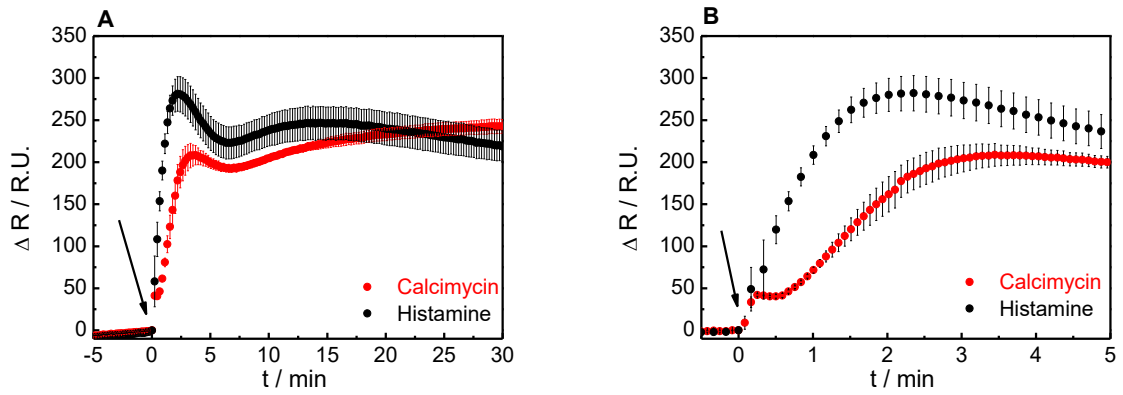

Fig. 4-40 A shows recording with the SPR device (slope mode) of U-373 MG cells stimulated with histamine (black, 10 µM) or *Calcimycin* (red; 10 µM), (n≥3; ± SD). **B** is an enlargement of **A** and shows the first 5 minutes of the plot **A**.

Fig. 4-41 (A) shows the stimulation of U-373 MG cells with the agonist histamine (10 µM, black curve) and the ionophor calcimycin (10 µM, red curve) as monitored by impedance recordings at a frequency of 32 kHz. The histamine-induced signal change starts at zero Ω for t=0 min. After histamine addition the signal increases first pointing to a dip (t = 1.1min., Δ IZI = -396 Ω). Impedance starts then increasing for the next 14 min reaching a maximum (t = 15 min, Δ IZI = 828 Ω). The signal decreases for the next 15 min till the end of recording (t = 30 min., Δ IZI = 596 Ω). The *Calcimycin* signal starts at zero Ω for t=0 min. After *Calcimycin* addition the signal increases first for 0.8 min and pointing to a dip (t = 2.8 min., Δ IZI = -194 Ω). Impedance starts then increasing and reaches a value of 539 Ω within 10 min. after *Calcimycin addition.* The signal increases slightly for the next 20 minutes till the end of data recording (t = 30 min.; Δ IZI = 860 Ω). The final impedance value of the *Calcimycin* stimulation is higher than the histamine value. Fig. 4-41 (B) shows an enlargement of Fig. 4-41 A. The cell response to *Calcimycin* addition shows a delay relative to the histamine response. The *Calcimycin* is added to the cells and for the first 45 seconds the signal increases. The next 2 minutes the signal decreases. The minimum dip occurs 2 minutes later with half of signal decrease compared to the histamine signal response. The *Calcimycin* signal shows a delay in cell response and the signal is increasing after the transient dip for the rest of recording time while the histamine answer reaches a maximum after 15 min and starts to decline afterwards.

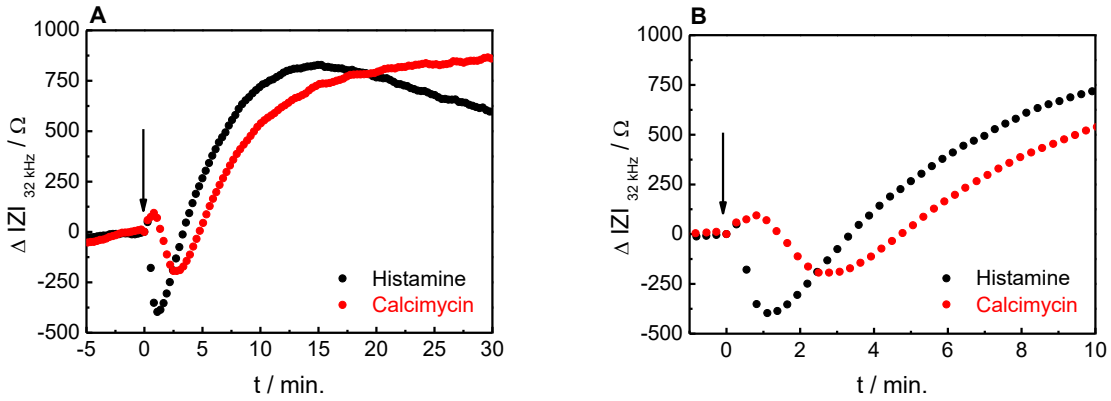

Fig. 4-41 shows impedance based recordings (8w1e, Applied BioPhysics Inc.) of U-373 MG cells stimulated with histamine (black, 10 µM) and *Calcimycin* (red; 10 µM), (single experiments). **B** is an enlargement of **A** and shows the first 10 minutes of plot **A**.

A different pharmacological tool that also addresses the involvement of intracellular Ca^{2+} in the signalling cascade is BAPTA AM, an intracellular chelator of Ca^{2+}. The acetoxymethyl-ester moieties (AM) will get cleaved off by intracellular esterases after diffusion across the plasma membrane so that the molecules accumulate inside the cell. In the presence of BAPTA the intracellular Ca^{2+}-concentration is efficiently buffered such that there is no burst-like rise that triggers any subsequent signalling cascade.

Fig. 4-42 shows SPR and ECIS time course data when confluent U-373 MG cells were first incubated for 20 minutes with three different solutions separately (n=3; ± SD):(1) L 15 medium with 2 % (v/v) DMSO (blue curve, L 15) which was used as solvent for the chemicals sulfinpyrazone, Pluronic® F-127 and BAPTA-AM. 20 minutes later the cells were exposed to histamine (1 µM). (2) L 15 medium including 2 % (v/v) DMSO with the sulfinpyrazone (250 µM) / Pluronic® F-127 (0.05 %) mix (red curve). 20 minutes after pre-incubation, histamine (1 µM) was added (blind control for the chemical cocktail without BAPTA-AM, red curve, control). (3) L 15 medium containing 2 % (v/v) DMSO with sulfinpyrazone (250 µM), Pluronic® F-127 (0.05 %) and BAPTA AM (20 µM) (intracellular chelator of Ca^{2+}) for 20 minutes (black curve, with the whole chemical cocktail including BAPTA AM, BAPTA AM). Fig. 4-42 (A SPR; B ECIS) shows the results of the dual ECIS-SPR sensor readout. In Fig. 4-42 (A, SPR, slope mode) the signal of the L 15 / DMSO control (blue curve) shows a dip (t = 0.5, Δ R= -21 R.U.) after histamine addition (black arrow, starting point t = 0; Δ R = 0 R.U.). Thereafter the signal increases by 87 R.U. to a maximum value (t = 2.8 min; Δ R = 66 R.U.). The signal decreases for 3 minutes to a minimum (t = 6 min; Δ R = 53 R.U.). The next 10 minutes the signal increases again for further 15 R.U. (t = 16 min; Δ R = 67 R.U.). The signal increase minimal till the end of data recording (t = 30 min; Δ R = 74 R.U.). The signal of the blind control as represented by Fig. 4-42 (A, SPR, slope mode) for the chemical cocktail (red curve) shows a dip (t = 0.5, Δ R = -32 R.U.)

after histamine addition (black arrow, starting point t = 0; Δ R = 0) and increases then for 69 R.U. to a maximum value (t =2.5 min; Δ R = 37 R.U.). The signal decreases for 3.5 minutes before the signal changes less fast (t= 6 min; Δ R = 7 R.U.). The next 24 minutes the signal decreases slightly, below the starting point, till the end of data recording (t = 30 min; Δ R = -51 R.U.). Fig. 4-42 (A, SPR, slope mode) the signal of the experiment with BAPTA-AM, (black curve) shows a dip (t = 0.7, Δ R = -52 R.U.) after histamine addition (black arrow, starting point t = 0; Δ R = 0 R.U.) and increases then for 1.5 minutes and 12 R.U. (t =2.2 min; Δ R = -40 R.U.). The signal decreases then till the end of data recording (t = 30 min; Δ R = -122 R.U.). Fig. 4-42 summarizes the corresponding ECIS experiment (B, ECIS, f = 32 kHz). The impedance of the blind control (blue curve) shows a dip (t = 1.8, Δ IZI = -43 Ω) after histamine addition (black arrow, starting point t = 0; Δ IZI = 0 Ω) and increases then for 13 minutes by 96 Ω to a maximum value (t =14.8 min; Δ IZI = 53 Ω). The signal stays nearly constant for 8 min. (t = 22.8 min; Δ IZI = 55 Ω). The signal then decreases till the end of recording (t = 30 min; Δ IZI = 45 Ω). The signal of the control for the chemical cocktail without BAPTA-AM (red curve) shows a dip (t = 1.8, Δ IZI = -33 Ω) after histamine addition (black arrow, starting point t = 0; Δ IZI = 0 Ω) and then increases for 13 minutes by 80 Ω to a maximum value (t =14.8 min; Δ IZI = 47 Ω). The signal then decreases till the end of data recording (t = 30 min; Δ IZI = 32 Ω). Time course data of the experiment with BAPTA-AM, (black curve) a dip (t = 2 min, Δ IZI = -12 Ω) shows after histamine addition (black arrow, starting point t = 0; Δ IZI = 0 Ω) and then increases for 13 minutes by 30 Ω to a maximum value (t =15 min; Δ IZI = 18 Ω). The signal stays almost constant till the end of recording (t = 30 min; Δ IZI = 16 Ω).

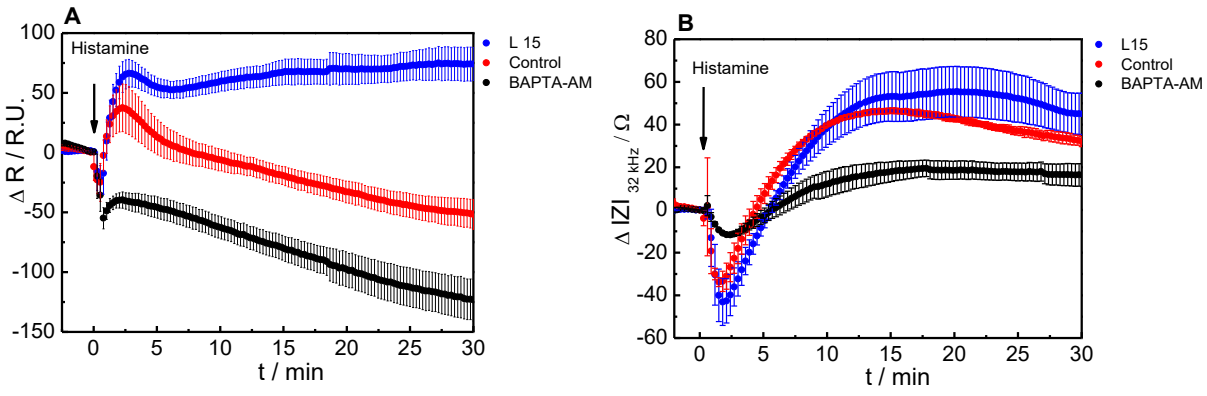

Fig. 4-42 shows the histamine (1 µM) induced response of U-373 MG cells recorded with the dual ECIS-SPR sensor (n=3; ± SD). Cells have been pre-treated for 20 minutes prior to histamine addition: 1.) L 15 medium with a corresponding amount of DMSO (2 % (v/v)) (blue curve) 2.) Control with sulfinpyrazone/Pluronic® F-127 dissolved in L 15/DMSO (red curve) 3.) BAPTA-AM / sulfinpyrazone/Pluronic® dissolved in L 15/DMSO. Reflectivity (slope mode) and impedance (f = 32 kHz) are plotted as a function of time.

The results for the histamine-*Calcimycin* (Fig. 4-40 SPR readout and Fig. 4-41 ECIS readout) and histamine-BAPTA-AM (Fig. 4-42) experiments lead to the conclusion that $_{h}H_{1}$ receptor is

$G_{\alpha q}$ coupled. The histamine stimulation of the U-373 MG cells lead to a similar response profile as *Calcimycin* does which increases the intracellular Ca^{2+} level. The BAPTA-AM treatment of the U-373 MG cells suppresses the histamine induced signal pattern more distinct for ECIS than for SPR readout. The results indicate that histamine activates by $_hH_1$ receptor activation the $G_{\alpha q}$-dependent signalling pathway.

Correlation of ECIS and SPR readouts

Since impedance- and SPR-readouts report on different physical properties of the cell layer under study in real time, it is straightforward to compare the time courses in detail. Such a correlation is possible by using datasets that have been recorded independently with the two techniques or by using the combined ECIS-SPR approach as described above. It is the idea to find characteristic features in the time course data of either technique and identify changes that occur in synchrony. Performing such a correlation analysis for activation of the receptor in absence or presence of specific pharmacological tools might provide deeper insight into the molecular basis for the time-resolved response profile of the cells under study and might even help to identify a signalling pathway from label-free time course data in the future. Fig. 4-43 (A) shows a representative response of the dual ECIS-SPR sensor when U-373 MG cells were stimulated with histamine (10 µM, n≥5 recorded over a period of 3 month). The ECIS and SPR data have been normed to one. The values (ECIS and SPR) at the time point of histamine addition have been normalized by division with the specific impedance value (IZI = Ω) and reflectivity value (R=R.U.) at time zero (histamine addition). The SPR response (red curve) shows a massive signal increase after histamine addition (t = 0 min., $R_{norm.}$ = 1) reaching a first maximum (maximum 1: t = 2.0 min; $R_{norm.}$ = 1.25) followed by a signal decrease (minimum 1: t = 5.5 min; $R_{norm.}$ = 1.21). The signal increases again describing a second maximum, smaller than the first maximum (maximum 2: t = 7.5 min.; $R_{norm.}$ = 1.22). The signal decreases till the end of data recording continuously (t = 30 min.; $R_{norm.}$ = 1.15). The impedance-based readout (black curve) a minor signal increase (t = 0.1 min.; $IZI_{norm.}$ = 1.02) shows after histamine addition (t = 0 min.; $IZI_{norm.}$ = 1) followed by a signal drop describing a signal minimum (minimum 1: t = 0.9 min. $IZI_{norm.}$ = 0.91). The signal increases for the next 15 minutes but the slope of the curve (black curve) is reduced continuously. The first point of slope change is 3.4 min after minimum 1 (t = 4.5; $IZI_{norm.}$ = 1.06) and the second point of slope change is 10.4 min after minimum 1 (t = 11.5; $IZI_{norm.}$ = 1.16). The signal (black curve) reaches a maximum 16.5 minutes after minimum 1 (t = 17.5; $IZI_{norm.}$ = 1.18). The signal starts decreasing till end of the recording time (t = 30 min; $IZI_{norm.}$ = 1.15). Fig. 4-43 (B) shows an enlargement of Fig. 4-43 A with a time section of 15 min. Comparing the signals of the two readouts, the first maximum of

the SPR readout (red curve) and the minimum of the impedance based readout (black curve) occur at different time points. The SPR readout (red curve) describes a biphasic signal while the impedance-based signal (black curve) shows a minor signal increase after histamine addition followed by a dip, starting a signal increase and reaching one maximum, followed by a signal increase till the end of data recording. The signals show extreme points at different time points, the extreme points don't overlap in time. The two different label-free readout systems complement each other because of their different physical basis, but report on different processes in the cells as characteristic points of the curve are not synchronous. The dual ECIS-SPR sensor offers the exactly overlay of the cell responses as the readout is recorded from one and the same cell population.

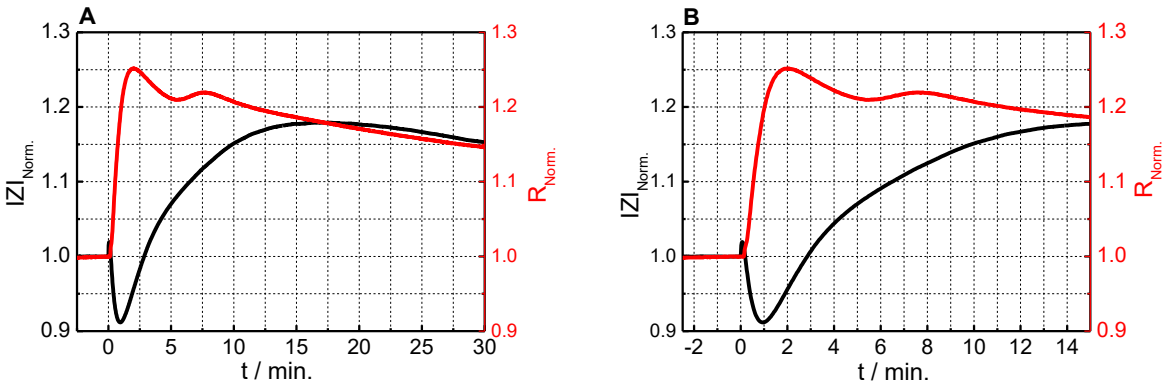

Fig. 4-43 **(A)** shows the histamine (10 µM, mean, n≥5; replicates have been recorded over a period of 3 month) induced response of U-373 MG cells, recorded with the dual ECIS-SPR sensor. Impedance-based data set (black curve, f=32 kHz) and SPR based readout (slope mode, red curve). Impedance and reflectivity plotted as function of time. **B** shows the first 15 minutes of plot **A**.

4.4.1.3 *Analyzing the Temperature-Dependent Cell Response*

Cell-based assays addressing GPCR-based signalling are often performed at different temperatures, with suspended or adherent cells and with or without any chemical probes for sensing. In particular temperature might be an important factor since the phase transition temperature of cell membrane is just around 30 °C. Accordingly, assays performed at room temperature may study the cellular model systems with a remarkably different membrane fluidity compared to physiological conditions. Since label-free assays are easily performed at different temperatures, the time-resolved response profiles have been recorded and analysed for different experimental temperatures. Fig. 4-44 shows the stimulation of U-373 MG cells with histamine (10 µM) as recorded with the SPR device (slope mode, Fig. 4-44, A and B) or the ECIS device (32 kHz, Fig. 4-44, C and D), respectively, at three different temperatures (27 °C blue curve, 37 °C green curve, 42 °C red curve). Time course SPR data summarized in Fig. 4-44 A shows for standard conditions of 37 °C (green curve) a maximum peak value at 2:30

min (Δ 260 R.U.) after histamine addition, followed by a minimum at 6 min. (220 R.U.). A second maximum occurs at 13 min (233 R.U.) followed by a slight decrease to 190 R.U. after 30 minutes. The signal pattern for 42 °C (red curve) has its maximum at 2 min (250 R.U.) followed by a minimum at 4:30 min (230 R.U.). A second higher maximum occurs at 10 min (265 R.U.) followed by a slight decrease to 200 R.U. after 30 minutes. The experiments conducted at 27 ° (blue curve) show a peak value of 215 R.U. at 4:30 min which is followed by a slight decrease to a minimum at 15 min and 155 R.U. The signal increases after 30 min to 173 R.U.. Fig. 4-44 B is an enlargement of Fig. 4-44 A, the plot illustrates the shift of the characteristic points of the curve along the time axis. Compared to the standard conditions (37 °C) the lower temperature (27 °C) induces a slower cell response whereas higher temperatures (42 °C) induces a faster signal increase. The values for ECIS at the time point of histamine addition (t=0 min) have been normalized by division with the specific impedance value at time zero (t= 0 min, IZI = Ω).The ECIS readout for standard conditions of 37 ° C (green curve) show (Fig. 4-44 C, 8W1E, Applied Biophysics Inc.) a minimum (t = 1 min., $IZI_{Norm.}$ = 0.90) after histamine addition, followed by impedance increase to a maximum (t = 15 min. $IZI_{Norm.}$ = 1.25). The signal decreases slightly till the end of data recording (t = 30 min. $IZI_{Norm.}$ = 1.21). The stimulation at higher temperature (42 °C, red curve) shows first a minimum (t = 0.9 min., $IZI_{Norm.}$ = 0.94) followed by a signal increase reaching a maximum (t = 9.5 min. $IZI_{Norm.}$ = 1.22). The signal decreases for the next 20 minutes till the end of data recording (t = 30 min. $IZI_{Norm.}$ = 1.09). The experiment at 27 °C (blue curve) shows first a minimum (t = 2.4 min., $IZI_{Norm.}$ = 0.92) followed by a constant signal increase till the end of data recording (t = 30 min. $IZI_{Norm.}$ = 1.11). The impedance values increase continuously but don't show the characteristic signal decrease as observed in the other experiments. Fig. 4-44 D is an enlargement of plot C. The plot (D) illustrates also the shift of characteristic curve features along the time axis.

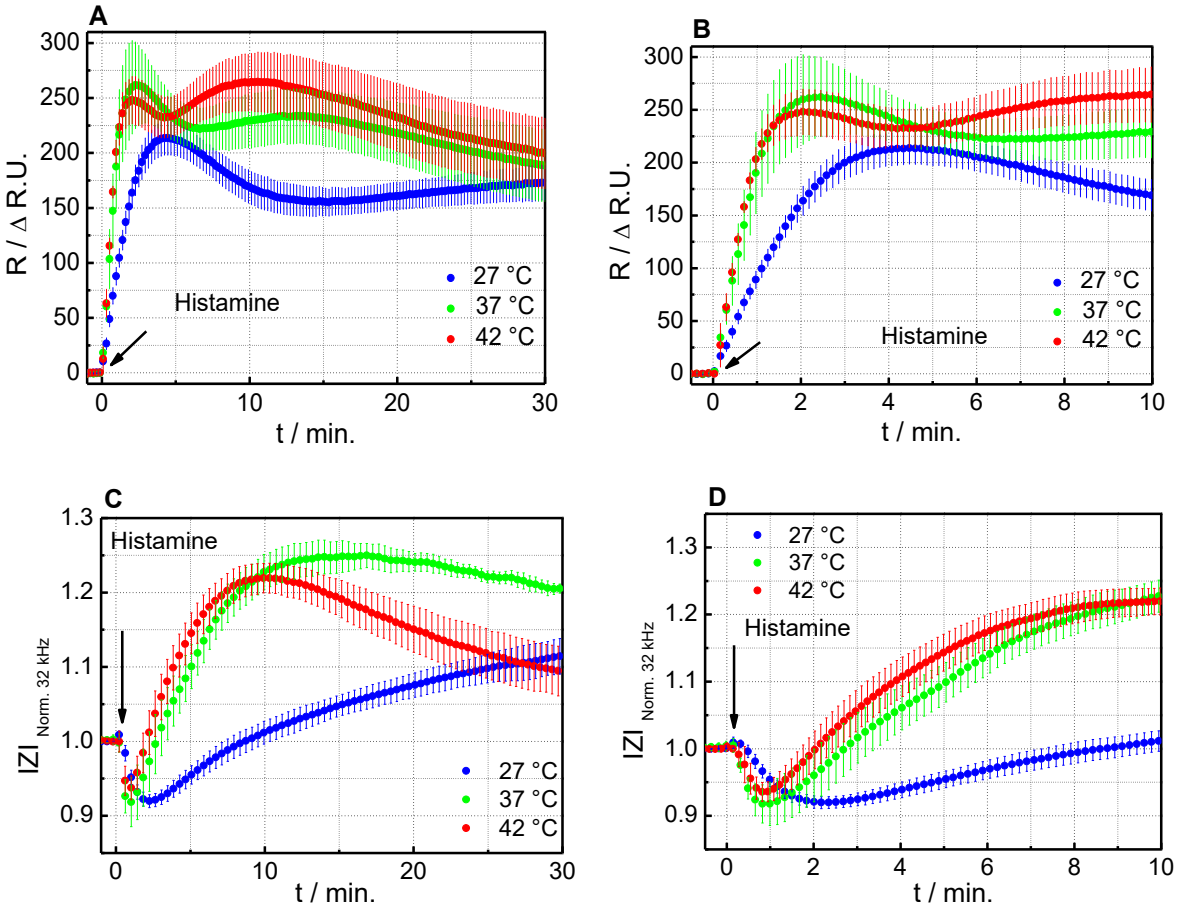

Fig. 4-44 **A** shows time course data recorded with the SPR device (slope mode) for U 373 cells when stimulated with histamine (10 µM) at three different temperatures (27 °C blue curve, 37 °C green curve, 42 °C red curve) (n≥4; mean ± SD). **B** shows the first 10 minutes of plot **A**. **C** shows the time course of impedance (8w1e Well, Applied BioPhysics inc.) (f = 32 kHz) for U 373 cells when stimulated with histamine (10 µM) at three different temperatures (27 °C blue curve, 37 °C green curve, 42 °C red curve) (n≥3; mean ± SD). **D** shows the first 10 minutes of plot **C**.

4.4.2 Human Dopamine D_2-Receptor (hD_2R)

The dopamine D_2 receptor is a member of the dopamine receptor family. Dopamine receptors are classified into D_1-like family, which activates the adenylate cyclase, and D_2-like family which inhibits the adenylate cyclase. The D_2 receptor is expressed in the genetically engineered model cell line CHO that was used in this thesis in two isoforms: the D_2L (long) and D_2S (short). The two receptor subtypes are not different with respect to the extracellular ligand binding site. However, the D_2S variant misses a cytosolic domain. The two isoforms are generated by alternative splicing [106]. According to pharmacology textbooks, the D_2-receptors are coupled to the G-protein $G_{\alpha i}$ which is known to inhibit the activity of the adenylate cyclase. The adenylate cyclase is an enzyme which converts ATP to cAMP. cAMP itself is a second messenger and is involved in further intracellular signal transduction.

4.4.2.1 *Dose-Response Analysis for Endogenous and Synthetic Receptor Agonists*

Endogenous Ligand Dopamine

The two isoforms of the D_2 receptor were first characterized by impedance-based cell monitoring with respect to a dose-response analysis when the endogenous ligand dopamine is used as a ligand. Fig. 4-45 shows the experimental data when CHO D_2S (short) (A) and CHO D_2L (long) (B) cells where exposed to increasing dopamine concentrations. Both receptors show dose dependent behaviour. The analysis of the impedance-based time courses provided EC_{50} values of (170 ± 60) nM for D_2S (short) (C) and an EC_{50} value of (72 ± 20) nM for D_2L (long) (D) when dopamine was used as ligand. D_2S cells (A) show signal maxima app. five minutes after dopamine addition for concentrations 0.1 µM dopamine and higher (Δ IZI = 30 Ω, for the maximum concentration of 3 µM). The signals stay then nearly constant afterwards and describe a plateau for the following 25 minutes. D_2L cells (B) show signal maxima for dopamine concentrations of 0.1 µM dopamine and higher app. 4 minutes after addition of the agonist (Δ IZI = 40 Ω, for maximum concentration of 3 µM) followed by a plateau phase of app. 3 minutes (t = 4-7 min.). The signals increase then for further 10 minutes to a new and higher maximum (t = 7-17 min, Δ IZI = 59 Ω, for the maximum concentration of 3 µM dopamine). Afterwards the impedance is stationary till the end of data recording (t= 30 min., Δ IZI = 62 Ω, for max concentration = 3 µM dopamine). The signals of the CHO isoforms (D_2S (A) and D_2L (B)) are distinguishable, the D_2L (B) has a more distinctive signal pattern, reaches maxima values faster with overall higher Δ IZI values.

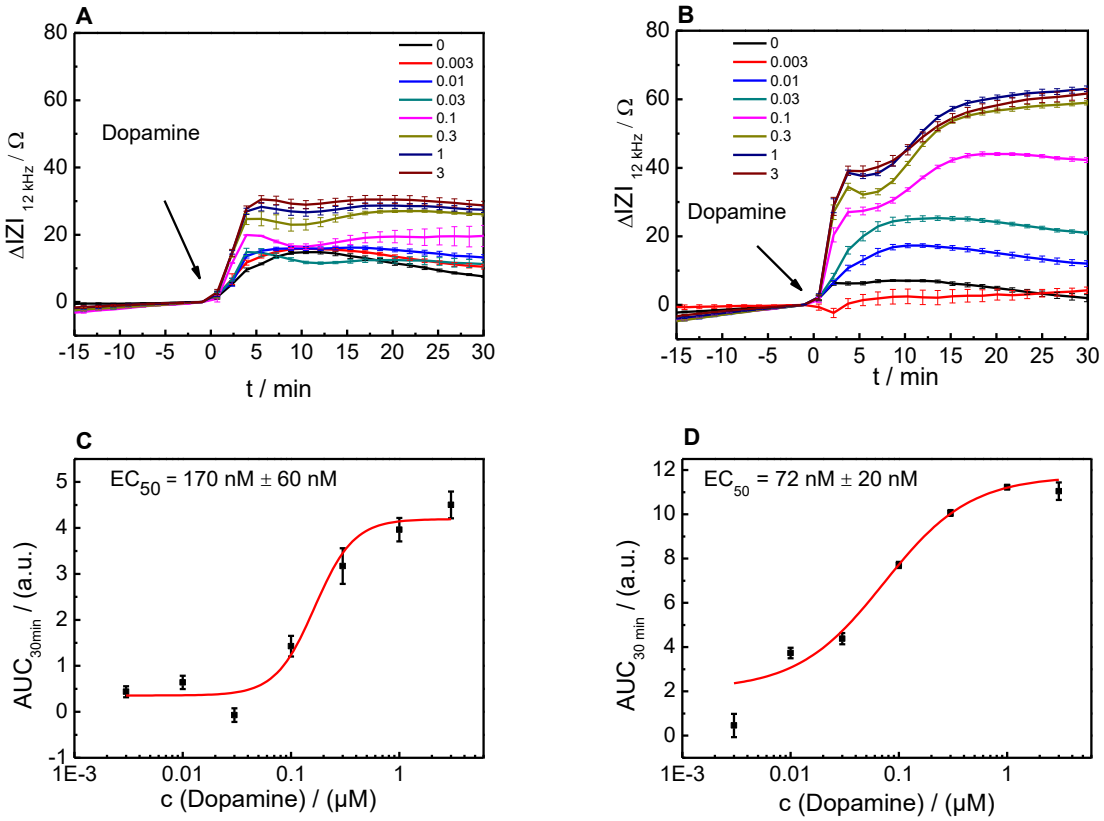

Fig. 4-45 Dopamine (c = µM) induced response of confluent CHO D_2S (short) (**A**) and CHO D_2L (long) (**B**) cells monitored by ECIS (96 W 20idf PET well array, Applied BioPhysics Inc.) (n ≥ 3; mean ± SE). Below are the corresponding concentration-response curves with the calculated EC_{50} value, **C** for CHO D_2S (short) (**A**) and **D** for CHO D_2L (long) (**B**).

Optical analysis of the D_2 receptor has been mainly performed by using the *dynamic mass redistribution* (DMR) technology instead of SPR to take advantage of much higher throughput. However, both methodologies are based on detecting subtle refractive index changes within the evanescent electric field that reaches into the bulk by about 100 nm – 200 nm. So both, SPR as well as DMR report on changes occurring at or close to the growth surface. DMR data, as recorded by the *Enspire* device marketed by Perkin Elmer, reflect the refractive index changes as a wavelength shift in units of pm rather than a reflectivity index. More details are given in chapter 1.3.4 and 3.5.

Fig. 4-46 shows DMR time course data when CHO D_2S (A) and CHO D_2L (B) cells were exposed to increasing dopamine concentrations. Both receptor subtypes show dose-dependent behaviour. Analysis of DMR data provided EC_{50} values of (48 ± 11) nM for D_2S (short) (C) and an EC_{50} value of (36 ± 19) nM for D_2L (long) (D) using dopamine as an agonist. D_2S cells (A) show a drifting baseline for 15 minutes by Δ λ = 125 pm. After dopamine addition all signal maxima are reached within 2 minutes (for maximum concentration of 10 µM dopamine, Δ λ = 190 pm), followed by a signal drop for 10 minutes (for max concentration of

10 µM dopamine, t = 12 min, Δ λ = 42 pm). The signals then become stationary at concentration-dependent individual values for rest of data recording. The signals show similar signal pattern for all concentrations, with concentration dependent maxima (t = 2 min.). D_2L cells (B) show a drifting baseline for 15 minutes by 75 pm on average. After dopamine addition all signal maxima are reached within 2 minutes in average, followed by a signal drop for 9 minutes (t = 2-11 min). High concentrations of dopamine show bigger signal drop than low concentrations (for maximum concentration of 10 µM dopamine; max. Δ λ = 295 pm and drop within 9 min. to 92 pm, t = 11 min.). The signals then become stationary at concentration-dependent values for the rest of data recording. The signals show a similar signal pattern for all concentrations, with concentration-dependent maxima followed by an individual signal decrease. The signal patterns of the two CHO isoforms (D_2S (A) and D_2L (B)) are similar but differ in signal maxima after dopamine addition.

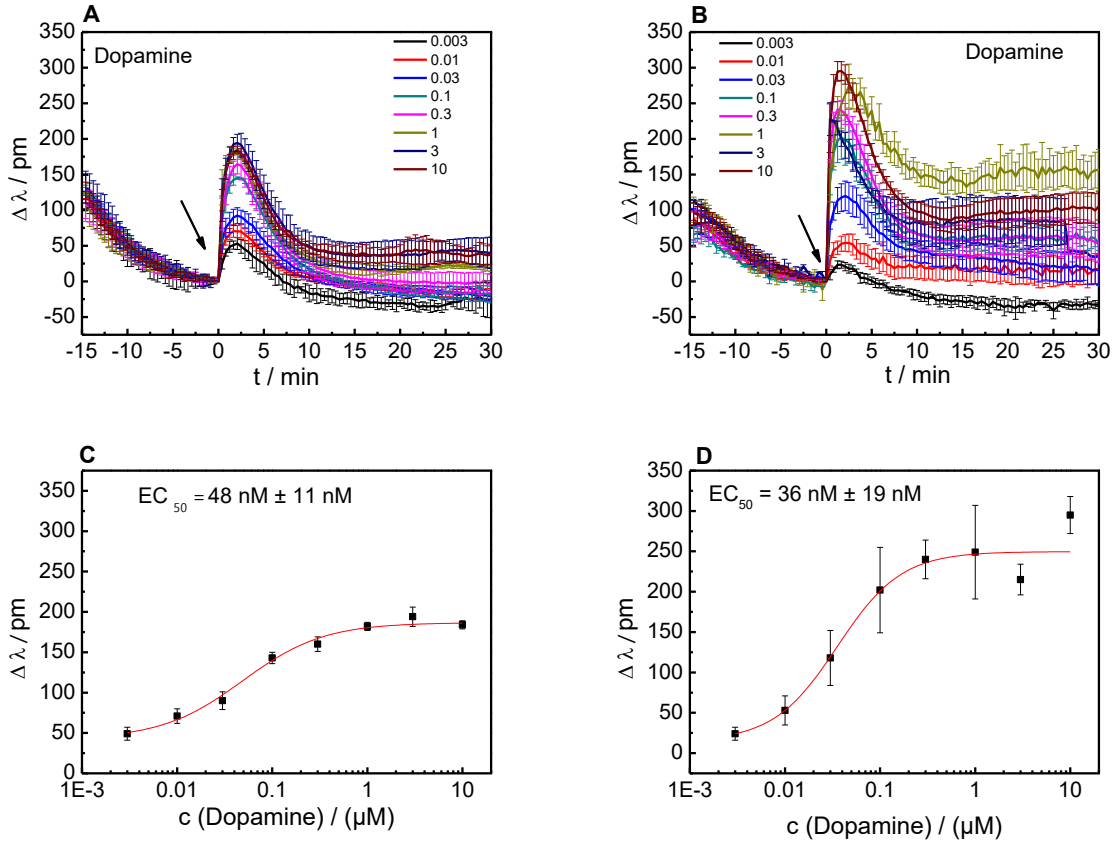

Fig. 4-46 Dopamine (c = µM) induced response of CHO D_2S (short) (**A**) and CHO D_2L (long) (**B**) cells monitored by DMR (n ≥ 3; mean ± SE). Below are the corresponding concentration-response curves with the calculated EC_{50} value, **C** for CHO D_2S (short) (**A**) and **D** for CHO D_2L (long) (**B**).

Synthetic Ligand Quinpirole

Similar experiments as described above have been performed with the synthetic D_2R/D_3R specific agonist quinpirole with both label-free monitoring approaches in order to characterize

the cell response to this non-endogenous agonist as well. Impedance-based monitoring provided the dose-dependent time course data as summarized in Fig. 4-47. Fig. 4-47 summarizes the impedance-based (ECIS) analysis when CHO D_2S (A) and CHO D_2L (B) cells were exposed to increasing quinpirole concentrations. Both receptors show dose-dependent behaviour. Analysis of the impedance-based data provided EC_{50} values of (14 ± 5) nM for D_2S (short) (C) and an EC_{50} value of (24 ± 4) nM for D_2L (long) (D) when quinpirole was used as a ligand. D_2S cells (A) show for quinpirole concentrations of 0.01 µM and higher signal maxima at app. 3.5 minutes after quinpirole addition (Δ IZI = 0.55 kΩ, for maximum concentration of 3 µM quinpirole), followed by a signal decrease for 4 minutes (t= 8 min, Δ IZI = 0.37 kΩ, for the maximum concentration of 3 µM quinpirole). The signal increased again for 7 minutes with a second and lower maximum (t= 15 min, Δ IZI = 0.46 kΩ, for the maximum concentration of 3 µM quinpirole). The signal decreases to a smaller value till the end of data recording (t = 30 min, Δ IZI = 0.41 kΩ, for the maximum concentration of 3 µM quinpirole). D_2L cells (B) show signal maximum for quinpirole concentrations of 0.1 µM and higher app. 2 minutes after stimulation (Δ IZI = 0.53 kΩ, for the maximum concentration of 3 µM quinpirole) followed by a signal decrease for 5 minutes (t= 7 min, Δ IZI = 0.33 kΩ, for the maximum concentration of 3 µM quinpirole). The signals increased again for further 6 minutes (t = 7-13 min) and reached second higher maximum (t= 13 min, Δ IZI = 0.65 kΩ, for the maximum concentration of 3 µM quinpirole). The signals are then almost stationary till the end of data recording. The signals of the two CHO isoforms (D_2S (A) and D_2L (B)) are distinguishable; the D_2L (B) has a more distinctive signal pattern, reaches maximum values faster with overall higher Δ IZI values.

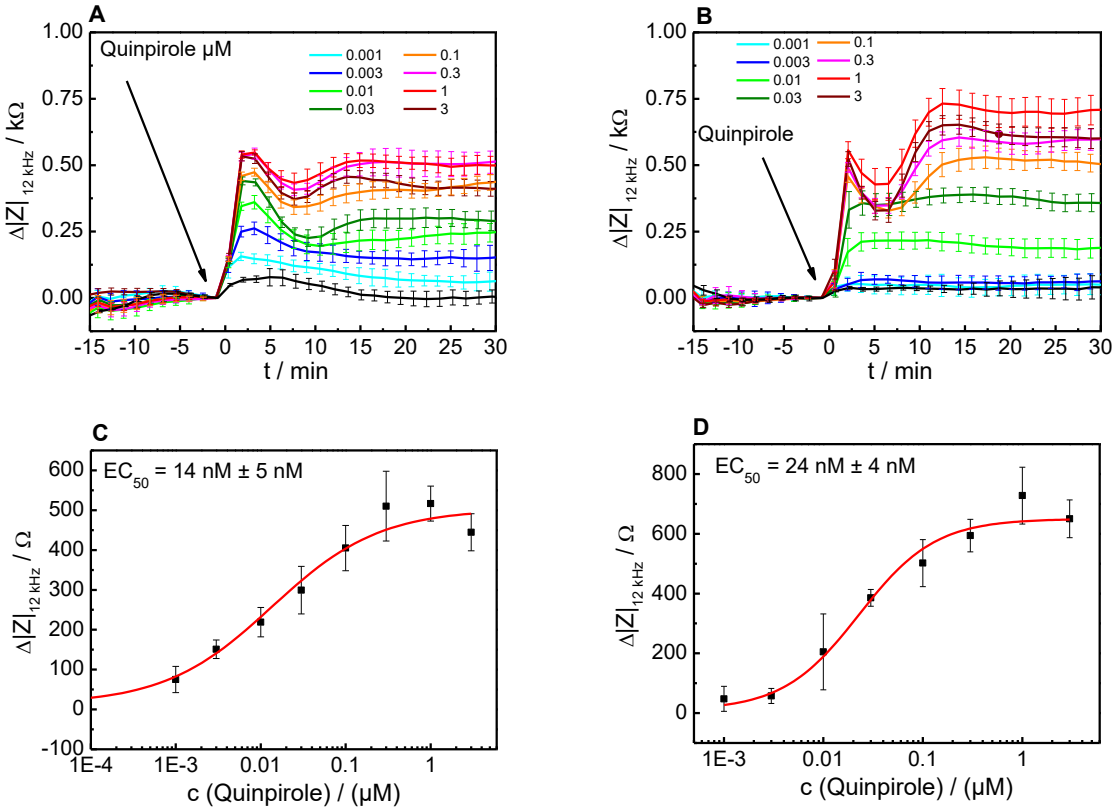

Fig. 4-47 Quinpirole (c = µM) induced response of CHO D_2S (short) (**A**) and CHO D_2L (long) (**B**) cells monitored by ECIS (96 W 20idf PET well array, Applied BioPhysics Inc.) (n ≥ 3; mean ± SE). Below are the corresponding concentration-response curves with the calculated EC_{50} values, **C** for CHO D_2S (short) (**A**) and **D** for CHO D_2L (long) (**B**). Data provided by Dr. Judith Stolwijk (University Regensburg).

Optical analysis for both isoforms using DMR technology provided the time courses summarized in Fig. 4-48. The data reflects a significant, transient and dose-dependent cell response which is, however, of smaller amplitude than observed for the endogenous ligand dopamine. Fig. 4-48 summarizes DMR time course data when CHO D_2S (A) and CHO D_2L (B) cells where exposed to increasing quinpirole concentrations. Both receptors show dose-dependent behaviour. Analysis of the DMR data provided EC_{50} values of (8 ± 2) nM for D_2S (short) (C) and an EC_{50} value of (66 ± 14) nM for D_2L (long) (D) when quinpirole is used as an agonist. D_2S cells (A) show a drifting baseline for 15 minutes of app 60 pm. After quinpirole addition all signal maxima are reached within 1.5 minutes (for max. concentration of 1 µM quinpirole, Δ λ = 160 pm), followed by a signal drop for 13 min (t = 14.5 min) which leads to DMR shifts below starting values for concentrations of 0.01 µM quinpirole and higher (for max. concentration of 1 µM quinpirole, Δ λ = -38 pm). Afterwards the signals become stationary with concentration-dependent values for the rest of data recording. The signals show for all concentrations similar signal patterns with concentration-dependent maxima (for max. concentration of 1 µM quinpirole, Δ λ = 160 pm). D_2L cells (B) show a drifting baseline for 15 minutes of 60 pm on average. After quinpirole addition all signal maxima are reached within 1.25 minutes in average (for max. concentration of 1 µM quinpirole, Δ λ = 180 pm), followed by

a signal drop for 8 minutes (t = 10 min) providing values slightly below starting values prior to stimulation (for max. concentration of 1 µM quinpirole, Δ λ = -13 pm). High concentrations of quinpirole show a bigger signal drop than lower concentrations. The signals become stationary then with concentration-dependent values for the rest of data recording. The signal shows for all concentrations a similar signal pattern with concentration-dependent maxima (for max. concentration of 1 µM quinpirole, Δ λ = 180 pm). The signals of the CHO isoforms (D_2S (A) and D_2L (B)) show similar signal pattern but differ in signal maxima after quinpirole addition.

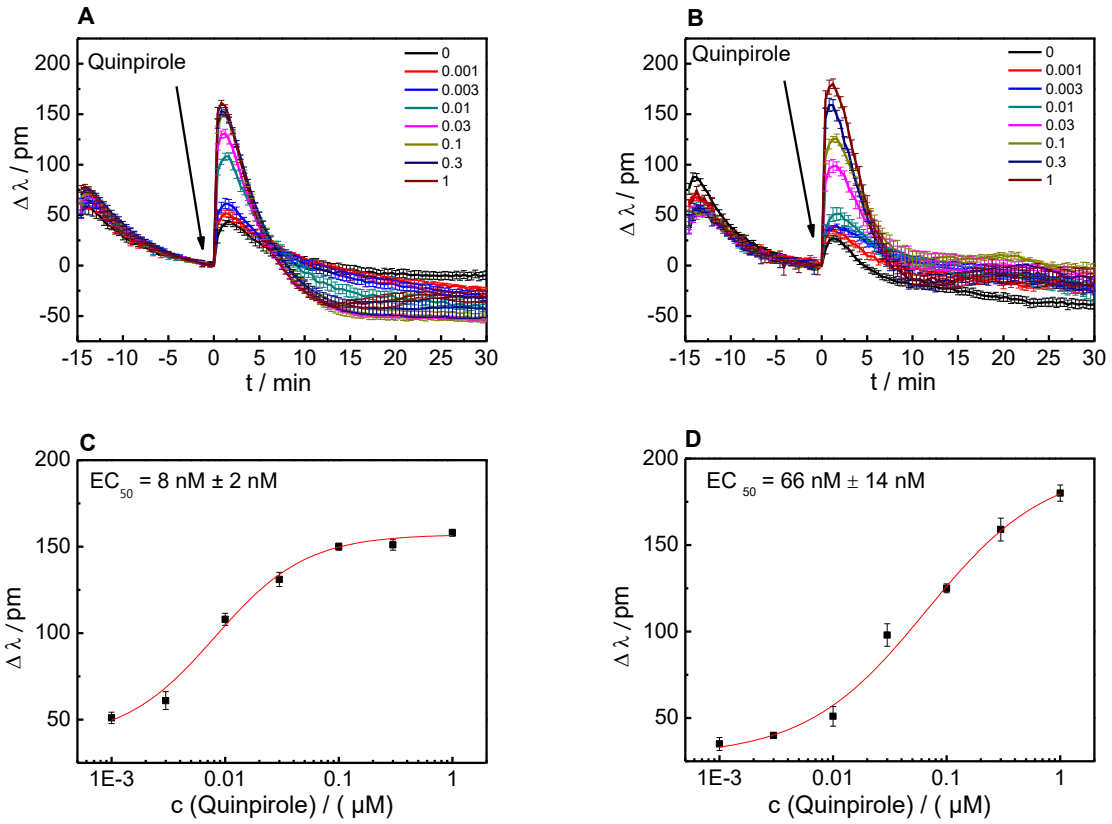

Fig. 4-48 Quinpirole (c = µM) induced response of CHO D_2S (short) (**A**) and CHO D_2L (long) (**B**) cells monitored by DMR (n ≥ 3; mean ± SE). Below are the corresponding concentration-response curves with the calculated EC_{50} value, **C** for CHO D_2S (short) (**A**) and **D** for CHO D_2L (long) (**B**).

4.4.2.2 *Deconvolution of the Signalling Cascade*

Pharmacological Tool

The D_2 receptors are preferably coupled to the $G_{\alpha i}$ pathway. Upon activation, $G_{\alpha i}$ inhibits adenylate cyclase that is responsible for producing the second messenger cAMP. However, under resting conditions the intracellular cAMP levels are rather low so that any inhibitory activity is hard to measure. This fact explains the rather small signal amplitudes that were observed in the preceding chapter for receptor activation using dopamine or quinpirole. A

pharmacological tool to probe the $G_{\alpha i}$ pathway is provided by Forskolin (FSK) that activates adenylate cyclase directly and thus independent of any receptor [107]. In a typical experiment the cells are pre-stimulated by Forskolin to increase basal cAMP levels before the agonist for $G_{\alpha i}$ coupled receptors is added. Compensation of the Forskolin-induced cell response by receptor activation indicates that the coupling scheme to $G_{\alpha i}$ is very likely correct. In this paragraph, experiments are described that probe the cell response to dopamine stimulation after the cells have been pre-treated with FSK using both label-free approaches. Initially the appropriate concentration of FSK for pre-stimulation has been assessed by DMR experiments.

Fig. 4-49 shows when CHO D_2S (short) and CHO D_2L (long) cells where exposed to increasing forskolin concentrations to determine the FSK EC_{80} value (n≥5; mean ± SE). The forskolin EC_{50} was separately determined for the isoforms CHO D_2S (A) and CHO D_2L (B). The forskolin activates the adenylate cyclase in the cells. The CHO D_2S isoform shows for the highest FSK concentration (6 µM FSK) a signal drop to a minimum value after 2 minutes with a $\Delta \lambda$ = -198 pm, followed by a slight signal increase till the end of the observation time (t = 30 min., $\Delta \lambda$ = -115 pm). The CHO D_2L isoform shows for the highest FSK concentration (6 µM FSK) a signal drop to a minimum value after 2 minutes with a $\Delta \lambda$ = -255 pm, followed by a slight increase to a maximum (t = 9 min., $\Delta \lambda$ = -211). The signal then decreases slightly till the end of the observation time (t = 30 min., $\Delta \lambda$ = -237 pm). Forskolin induces over the whole concentration range bigger signal drops for the CHO cells expressing the D_2L isoform compared to the CHO cells expressing the D_2S isoform. The EC_{80} value for the pre-stimulation are 2.3 µM FSK for the D_2S (short) (C) and 0.5 µM FSK for the CHO D_2L (long) (D) isoform.

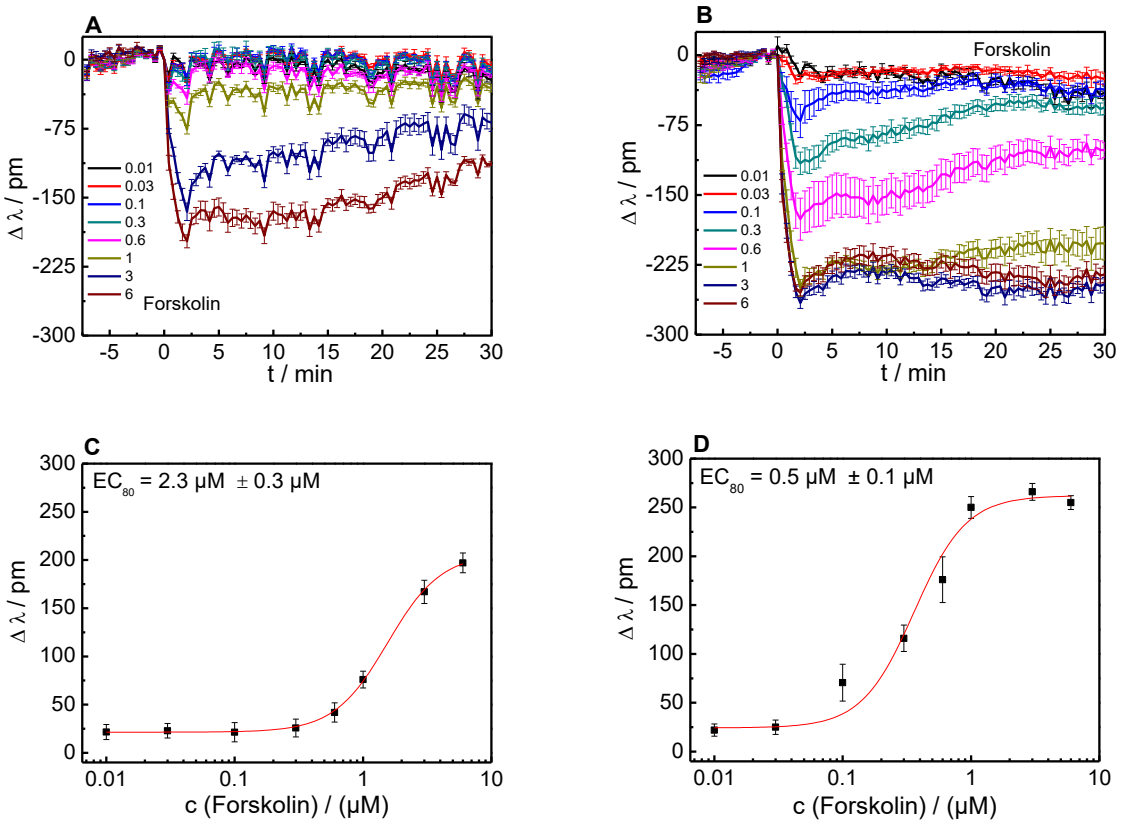

Fig. 4-49 **A** shows the stimulation of CHO D_2S (short) (n≥5; mean ± SE) cells with increasing forskolin concentrations (µM) recorded with DMR. The corresponding concentration-response curves provided an EC_{80} value of 2.3 µM forskolin (**C**, D_2S (short)). **B** shows the stimulation of CHO D_2L (long) (n≥5; mean ± SE) cells with increasing forskolin concentrations. The corresponding concentration-response curve provided an EC_{80} value of 0.5 µM forskolin (**D**, D_2L (long)).

Label-free readouts recorded for dopamine and quinpirole stimulation have been compared without (w/o) any pre-stimulation and with (w) a pre-stimulation with a fixed concentration of FSK 15 min prior to agonist addition. The direct comparison of both situations indicates the potential involvement of the $G_{\alpha i}$ pathway. First, impedance-based monitoring has been used to study the response of D_2R-transfected CHO cells upon dopamine stimulation.

CHO D_2S (short) / without (w/o) and with (w) FSK / Dopamine / ECIS and DMR readout

Fig. 4-50 shows an impedance-based (ECIS) analysis when CHO D_2S (short) cells without (A, w/o) and with 2.3 µM FSK pre-stimulation (B, w) were exposed to increasing dopamine concentrations. In both scenarios the cells show dose-dependent response profiles. Analysis of the impedance-based data provided EC_{50} values of (78 ± 15) nM for CHO D_2S (short) cells without (C, w/o) and an EC_{50} value of (54 ± 6) nM for CHO D_2S (short) cells with FSK pre-stimulation (D, w) when dopamine was used as an agonist. D_2S-expressing cells (A, w/o) show no signal perturbation when pure medium was added to the cells to have a control on

the cell reaction. Dopamine induced signal maxima 3 minutes after addition for concentrations of 0.1 µM dopamine and higher (Δ IZI = 0.40 kΩ, for max concentration of 10 µM dopamine). The signals run through a transient minimum (t = 7 min., Δ IZI = 0.34 kΩ, for max. concentration of 10 µM dopamine) followed by a second maximum (t = 15 min., Δ IZI = 0.43 kΩ, for max. concentration of 10 µM dopamine) and decrease slightly till the end of data akqusition (t = 30 min., Δ IZI = 0.41 kΩ, for max. concentration of 10 µM dopamine). CHO D_2S-expressing cells pre-stimulated with 2.3 µM FSK (B, w) show a massive signal drop of 1.8 kΩ within 5 minutes after FSK addition (2.3 µM). The next 5 minutes the signal decrease further by 0.17 kΩ. For the next 5 minutes and before dopamine addition the signals decrease slightly (t = 0, Δ IZI = 0.04 kΩ). Dopamine stimulation induced steep signal increases for concentrations of 0.1 µM dopamine and higher within 3 minutes after stimulation (Δ IZI = 1.6 kΩ, for max. concentration of 10 µM dopamine) followed by a further slight signal increase for 10 minutes (t = 13 min., Δ IZI = 2.2 kΩ, for max. concentration of 10 µM dopamine). The signals increase slightly till the end of data recording (t = 30 min, Δ IZI = 2.3 Ω, for max. concentration of 10 µM dopamine). The CHO isoform D_2S (short) shows significantly different signal patterns when the cells are pre-stimulated with FSK (2.3 µM) prior to dopamine stimulation compared to untreated cells.

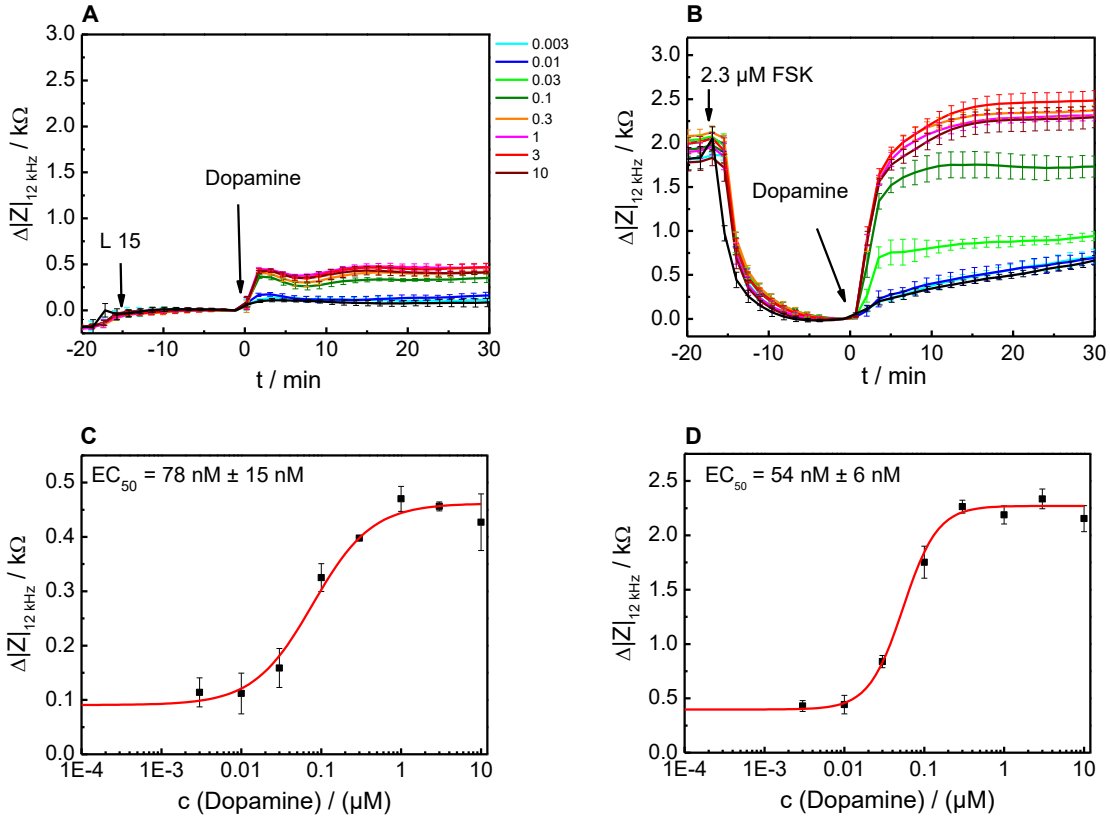

Fig. 4-50 Dopamine (c = µM) induced response of CHO D_2S (short) cells without (**A, w/o**) and with FSK pre-stimulation (2.3 µM) (**B, w**) monitored by ECIS (96 W 20idf PET well array, Applied BioPhysics Inc.) (n≥ 3; mean ± SE). Below are the concentration-response curves with the calculated EC_{50} values, **C (w/o)** for CHO D_2S (short) cells without and **D (w)** CHO D_2S (short) cells with FSK pre-stimulation (2.3 µM). Data provided by Dr. Judith Stolwijk (University Regensburg).

Fig. 4-51 shows DMR-based analysis when CHO D_2S (short) cells without (A, w/o) and with 2.3 µM FSK pre-stimulation (B, w) were exposed to increasing dopamine concentrations. In both scenarios time course analysis shows dose-dependent response profiles. Analysis of the DMR-based data provided EC_{50} values of (48 ± 11) nM for D_2S (short) cells without (C, w/o) and an EC_{50} value of (92 ± 23) nM for CHO D_2S (short) cells with FSK pre-stimulation (D, w) when dopamine is used as a ligand. CHO D_2S-expressing cells (A, w/o) not exposed to FSK show a drifting baseline for 15 minutes by app. Δ λ = 120 pm. After dopamine addition all signal maxima are reached within 2 minutes (for max. concentration of 10 µM dopamine, Δ λ = 190 pm), followed by a signal drop for 10 minutes (for max. concentration of 10 µM dopamine, t = 12 min, Δ λ = 42 pm). The signals then become stationary at concentration-dependent values for the rest of data recording. The signal show for all concentrations a similar signal pattern with concentration-dependent maxima (t = 2 min.). CHO cells expressing D_2S pre-stimulated with 2.3 µM FSK (B, w) show a drifting signal after FSK addition (2.3 µM) for 15 minutes by app. 125 pm. After dopamine addition all signal maxima are reached within 2 minutes (for max. concentration of 10 µM dopamine, Δ λ = 242 pm), followed by a signal drop for 13 minutes (t = 15 min, Δ λ = 86 pm, for max. concentration of 10 µM dopamine). High concentrations of dopamine show bigger signal maxima and bigger signal drop than low concentrations. The signals then become stationary at concentration-dependent values for the rest of data recording. The signal shows for all concentrations a similar signal pattern with concentration-dependent maxima (for max. concentration of 10 µM dopamine, Δ λ = 242). The signals of the CHO isoform D_2S (A, w/o) without FSK and (B, w) with FSK pre-stimulation differ in their individual signal maxima after dopamine addition but do not show significant differences in their signal patterns.

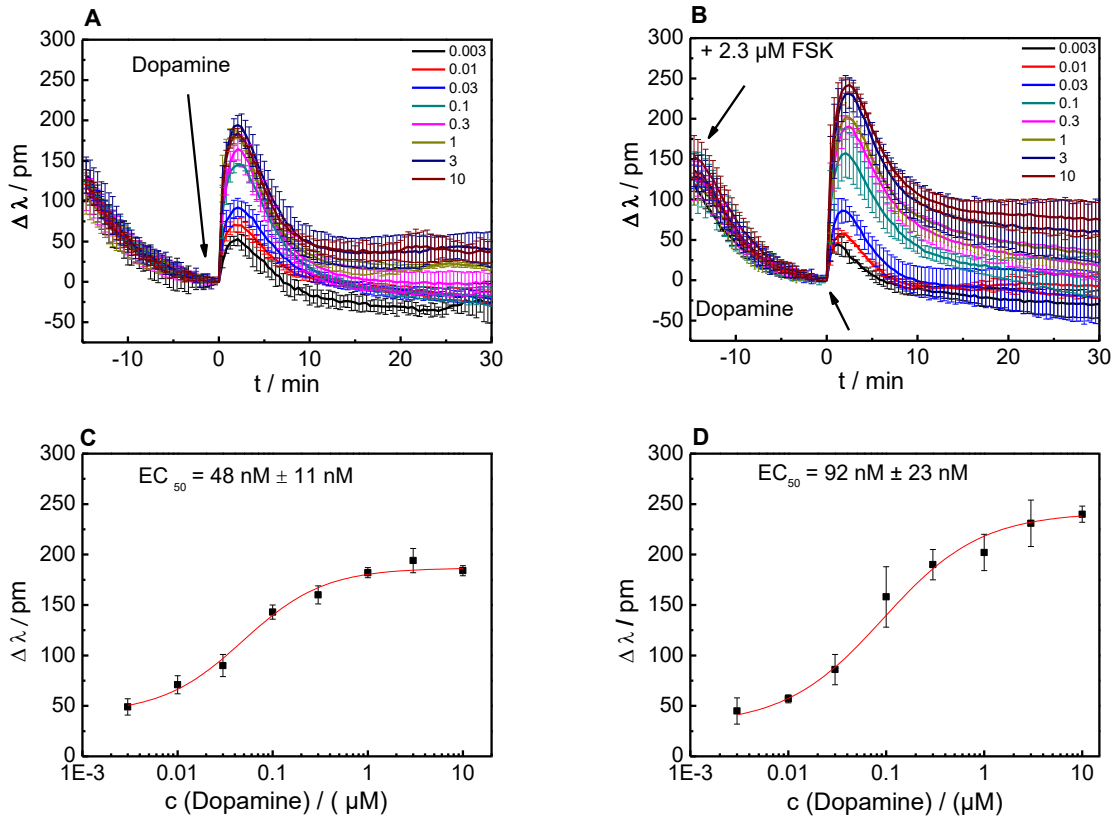

Fig. 4-51 Dopamine (c = µM) induced response of CHO D_2S (short) cells without (**A, w/o**) and with FSK pre-stimulation (2.3 µM) (**B, w**) monitored by DMR (n≥ 3; mean ± SE). Below are the concentration-response curves with the calculated EC_{50} values, **C (w/o)** for CHO D_2S (short) cells without and **D (w)** for CHO D_2S (short) cells with FSK pre-stimulation (2.3 µM).

CHO D_2L (long) / without (w/o) and with (w) FSK / Dopamine / ECIS and DMR readout

Fig. 4-52 summarizes the impedance-based (ECIS) analysis when CHO D_2L (long) cells without (A, w/o) and with 0.5 µM FSK pre-stimulation (B, w) were exposed to increasing dopamine concentrations. In both scenarios the cells show dose-dependent response profiles. Analysis of the impedance-based data provided EC_{50} values of (30 ± 2) nM for CHO cells expressing D_2L (long) without (C, w/o) and an EC_{50} value of (14 ± 1) nM for CHO D_2L (long) with FSK pre-stimulation (D, w) when dopamine was used as an agonist. D_2L-expressing cells (A, w/o) show no signal perturbation when pure medium was added to the cells to have a control on the cell reaction. CHO D_2L-expressing cells show signal maximum for dopamine concentrations of 0.03 µM and higher within 2.5 minutes after stimulation (Δ IZI = 0.7 kΩ, for max. concentration of 10 µM dopamine). The signals run through a transient minimum (t = 5.5 min, Δ IZI = 0.45 kΩ, for max concentration of 10 µM dopamine) followed by a second maximum (t = 12.5 min., Δ IZI = 0.91 kΩ, for max. concentration of 10 µM dopamine). The signals then become stationary at concentration-dependent values and decrease slightly till

the end of data recording (t = 30 min, Δ IZI = 0.85 kΩ, for max. concentration of 10 µM dopamine). CHO D_2L cells pre-stimulated with 0.5 µM FSK (B, w) show a massive signal drop of 1.4 kΩ within 5 minutes after FSK addition (0.5 µM). The next 5 minutes the signal decrease further by 0.15 kΩ. For the next 5 minutes and before dopamine addition the signals decrease slightly (t = 0, Δ IZI = 0.03 kΩ). Dopamine stimulation induced steep signal increases for concentrations of 0.03 µM dopamine and higher within 3 minutes after stimulation (Δ IZI = 1.6 kΩ, for max. concentration of 10 µM dopamine) followed by a further slight signal increase for 10 minutes (t = 13 min., Δ IZI = 2.6 kΩ, for max. concentration of 10 µM dopamine). The signals increase slightly till the end of data recording (t = 30 min., Δ IZI = 2.7 Ω, for max. concentration of 10 µM dopamine). The CHO isoform D_2L (long) shows significantly different signal patterns when the cells are pre-stimulated with FSK (0.5 µM) prior dopamine stimulation compared to untreated cells.

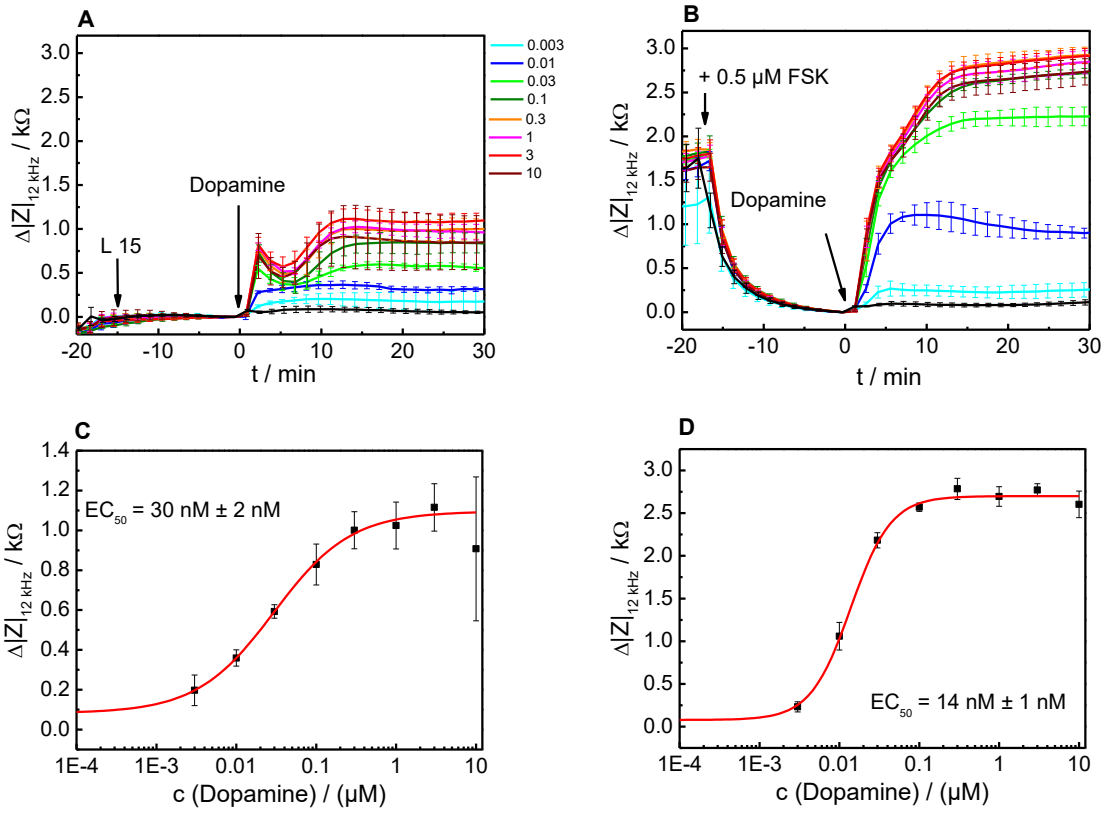

Fig. 4-52 Dopamine (c = µM) induced response of CHO D_2L (long) cells without (**A, w/o**) and with FSK pre-stimulation (0.5 µM) (**B, w**) monitored by ECIS (96 W 20idf PET well array, Applied BioPhysics Inc.) (n≥ 3; mean ± SE). Below are the concentration-response curves with the calculated EC_{50} values, **C (w/o)** for CHO D_2L (long) cells without and **D (w)** for CHO D_2L (long) cells with FSK pre-stimulation (0.5 µM). Data provided by Dr. Judith Stolwijk (University Regensburg).

Fig. 4-53 shows DMR based analysis when CHO D_2L (long) cells without (A, w/o) and with 0.5 µM FSK pre-stimulation (B, w) cells were exposed to increasing dopamine concentrations. In both scenarios time course analysis shows dose-dependent response profiles. Analysis of the DMR-based data provided EC_{50} values of (36 ± 19) nM for CHO D_2L (long) cells without

(C, w/o) and an EC_{50} value of (27 nM ± 14) nM for CHO D_2L (long) cells with FSK pre-stimulation (D, w) when dopamine is used as ligand. CHO D_2L-expressing cells (A, w/o) not exposed to FSK show a drifting baseline for 15 minutes by app. Δ λ = 90 pm. After dopamine addition all signal maxima are reached within 2 minutes (for max. concentration of 10 µM dopamine, Δ λ= 290 pm,), followed by a signal drop for 10 minutes (for max. concentration of 10 µM dopamine, t = 12 min, Δ λ = 90 pm). The signals then become stationary at concentration-dependent values for the rest of data recording (for max. concentration of 10 µM dopamine, t = 30 min, Δ λ = 100 pm). The signal show for all concentrations a similar signal pattern with concentration-dependent maxima (t = 2 min.). CHO D_2L cells pre-stimulated with 0.5 µM FSK (B, w) show after FSK addition (0.5 µM) for 5 minutes a signal drop of app. 170 pm before describing a kink (t = - 10 min, Δ λ = 47 pm) and decrease for the next 10 minutes with a further signal drop to 0 pm (t = 0 min). After dopamine addition all signal maxima are reached within 2 minutes (for max. concentration 10 µM dopamine, Δ λ = 500 pm), followed by a signal drop for 10 minutes (t = 12 min, Δ λ = 300 pm, for max. concentration 10 µM dopamine). The signals then become stationary at concentration-dependent values for the rest of data recording (for max. concentration 10 µM dopamine, t = 30 min, Δ λ = 320 pm). The signals recorded for the CHO D_2L cells without (A, w/o) and with FSK pre-stimulation (B, w) are distinguishable. FSK pre-stimulation of CHO D_2L (B, w) provides a remarkable signal drop compared to the cells without FSK (A, w/o). After dopamine addition differences in signal maxima, with almost two times higher Δ λ, are recorded for the FSK pre-stimulated CHO D_2L cells (B, w) compared to the cells without FSK (A, w/o). The signals of the CHO D_2L isoform without FSK (A) and with FSK pre-stimulation (B) are distinguishable dependent on a pre-stimulation with FSK or not

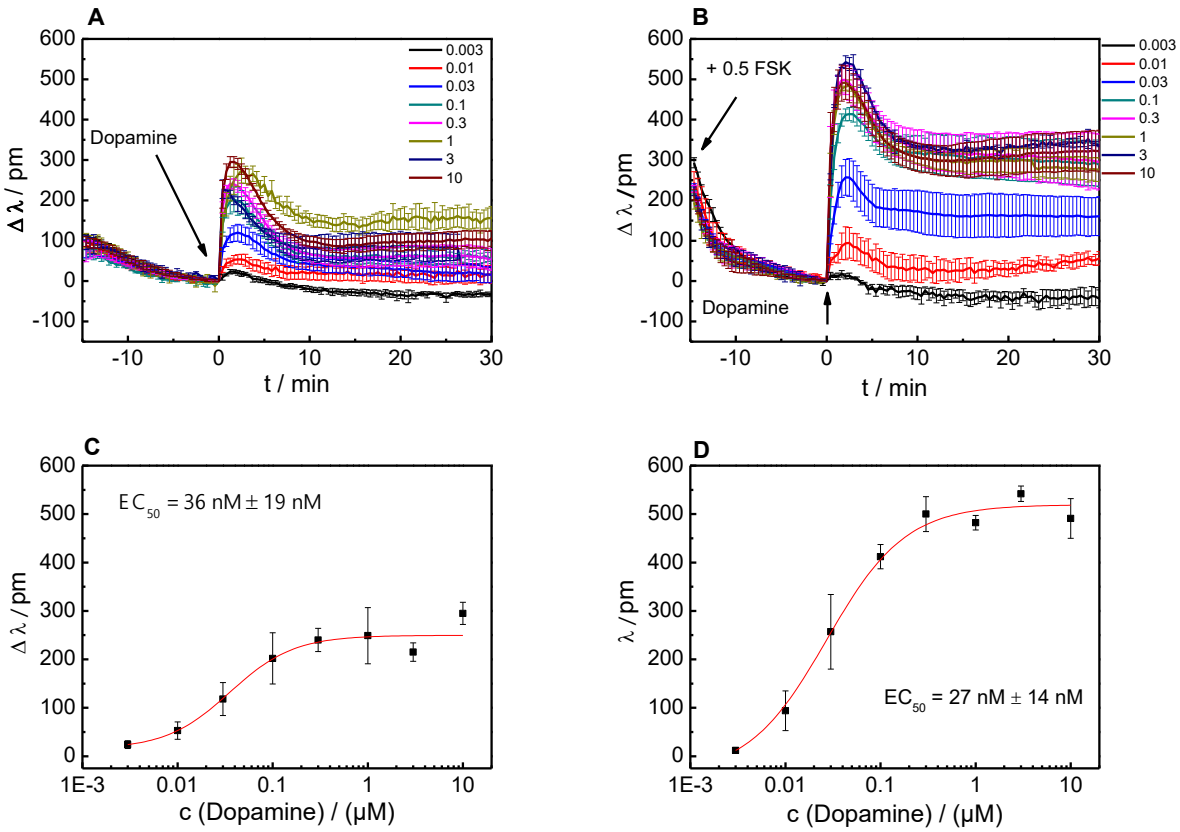

Fig. 4-53 Dopamine (c = µM) induced response of CHO D_2L (long) cells without (**A, w/o**) and with FSK pre-stimulation (0.5 µM) (**B, w**) monitored by DMR (n≥ 3; mean ± SE). Below are the concentration-response curves with the calculated EC_{50} values, **C (w/o)** for CHO D_2L (long) without and **D (w)** for CHO D_2L cells with FSK pre-stimulation (0.5 µM).

CHO D_2S (short) / without (w/o) and with (w) FSK / Quinpirole / ECIS and DMR readout

Fig. 4-54 shows an impedance based (ECIS) analysis when CHO D_2S (short) cells without (A, w/o) and with 2.3 µM FSK pre-stimulation (B, w) were exposed to increasing quinpirole concentrations. In both scenarios the cells show dose-dependent response profiles. Analysis of the impedance-based data provided EC_{50} values of (14 ± 5) nM for D_2S (short) without (C, w/o) and an EC_{50} value of (1.5 ± 0.1) nM for D_2S (short) with FSK pre-stimulation (D, w) when quinpirole was used as an agonist. D_2S expressing CHO cells (A, w/o) show no signal perturbation when pure media was added to the cells, to have a control on the cell reaction. Quinpirole induced signal maxima 3 minutes after addition for concentrations of 0.3 µM quinpirole and higher (Δ IZI = 0.5 kΩ, for max. concentration of 3 µM quinpirole). The signals run through a transient minimum (t = 7 min., Δ IZI = 0.42 kΩ for max. concentration of 3 µM quinpirole) followed by a second maximum (t = 15 min. Δ IZI = 0.45 kΩ for max. concentration of 3 µM quinpirole) and decrease slightly till the end of data recording (t = 30 min. Δ IZI = 0.41 kΩ). CHO D_2S cells pre-stimulated with 2.3 µM FSK (B, w) show a massive signal drop of 1.75

kΩ within 5 minutes after FSK addition. The next 5 minutes the signal decrease further by 0.20 kΩ. For the next 5 minutes and before quinpirole addition the signals decrease slightly (t = 30 min., Δ IZI = 0.03 kΩ). Quinpirole stimulation induced steep signal increases for concentrations of 0.01 µM quinpirole and higher within 3 minutes after stimulation (Δ IZI = 1.9 kΩ, for max concentration of 3 µM quinpirole) followed by a further slight signal increase for 10 minutes (t = 13 min, Δ IZI = 2.45 kΩ, for max. concentration of 3 µM quinpirole). The signals increase slightly till the end of data recording (t = 30 min., Δ IZI = 2.5 Ω, for max concentration of 3 µM quinpirole). The CHO cells expressing isoform D_2S (short) shows significantly different signal patterns when the cells are pre-stimulated with FSK (2.3 µM) prior to quinpirole stimulation compared to untreated cells.

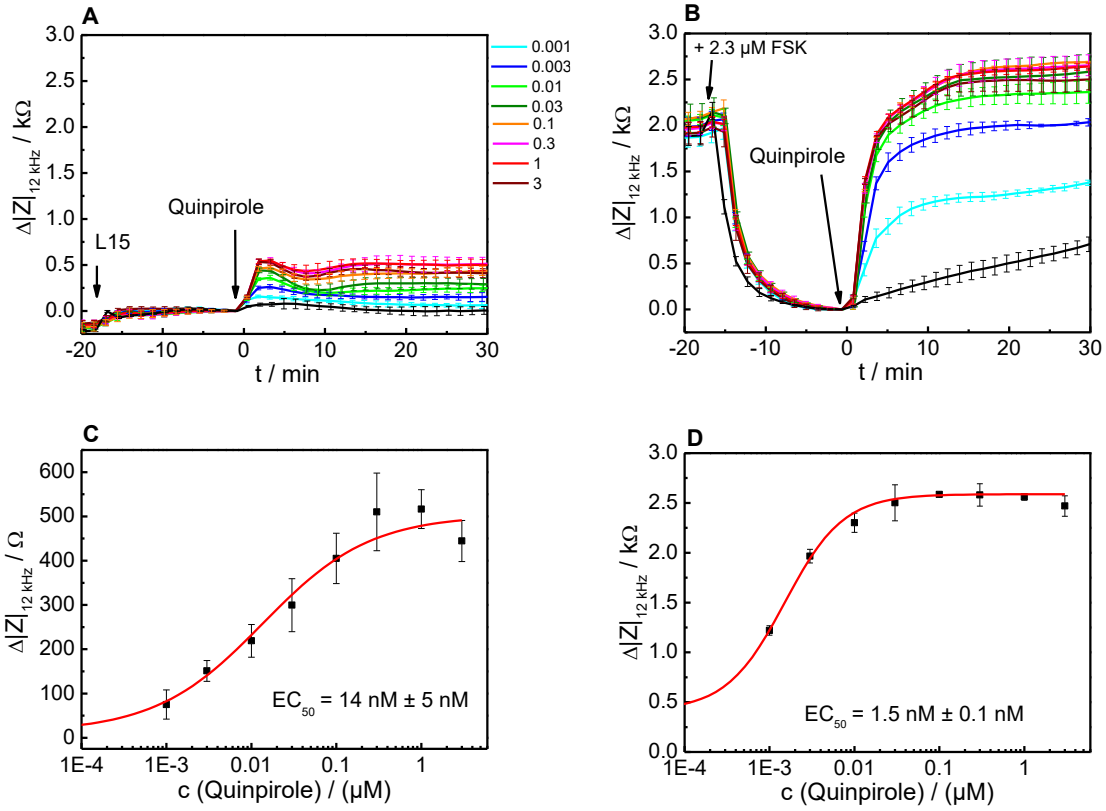

Fig. 4-54 Quinpirole (c = µM) induced response of CHO D_2S (short) cells without (**A, w/o**) and with FSK pre-stimulation (2.3 µM) (**B, w**) monitored by ECIS (96 W 20idf PET well array, Applied BioPhysics Inc.) (n≥ 3; mean ± SE). Below are the concentration-response curves with the calculated EC_{50} values, **C (w/o)** for CHO D_2S (short) without and **D (w)** for CHO D_2S (short) with FSK pre-stimulation (2.3 µM). Data provided by Dr. Judith Stolwijk (University Regensburg).

Fig. 4-55 shows DMR-based analysis when CHO D_2S (short) cells without (A, w/o) and with 2.3 µM FSK pre-stimulation (B, w) were exposed to increasing quinpirole concentrations. In both scenarios time course analysis shows dose-dependent response profiles. Analysis of the DMR-based data provided EC_{50} values of (8 ± 2) nM for D_2S (short) without (C, w/o) and EC_{50} value of (2 ± 1.6) nM for D_2S (short) cells with FSK pre-stimulation (D, w) when quinpirole is

used as a ligand. D_2S expressing CHO cells (A, w/o) not exposed to FSK show a drifting baseline for 15 minutes by app. $\Delta \lambda$ = 60 pm. After quinpirole addition all signal maxima are reached within 1.25 minutes (for max. concentration of 1 µM quinpirole, $\Delta \lambda$ = 160 pm), followed by a signal drop for 12 minutes (for max. concentration of 1 µM quinpirole, t = 13.5 min, $\Delta \lambda$ = -39 pm). The signals then become stationary at concentration-dependent values for the rest of data recording (for max. concentration 1 µM quinpirole, t = 30 min, $\Delta \lambda$ = -30 pm). The signal show for all concentrations a similar signal pattern with concentration dependent maximum (t = 1.25 min.). CHO cells expressing D_2S prestimulated with 2.3 µM FSK (B, w) show after FSK addition (2.3 µM) for 2.5 minutes a steep signal drop of app. 90 pm. The next 7.5 minutes the signal drops app. for further 45 pm (t = -5 min) and stay nearly at a constant signal level before quinpirole addition (t = 0, $\Delta \lambda$ = 0 pm). After quinpirole addition all signal maxima are reached within 1.25 minutes (for max. concentration of 1 µM quinpirole, $\Delta \lambda$ = 300 pm), followed by a signal drop for 13 min (for max. concentration of 1 µM quinpirole, t = 14.25 min, λ = 119 pm). High concentrations of quinpirole show bigger signal maxima and bigger signal drop than low concentrations. The signals then become stationary at concentration-dependent values for the rest of data recording (for max. concentration of 1 µM quinpirole, t = 30 min, $\Delta \lambda$ = 108 pm). The signal shows for all concentrations a similar signal pattern with concentration dependent maxima. FSK pre-stimulation of CHO D_2S (B, w) cells provides a remarkable signal drop compared to the cells without FSK (A, w/o). After quinpirole addition differences in signal maxima, with almost two times higher $\Delta \lambda$, are recorded for the FSK prestimulated CHO D_2S cells (B, w) compared to cells without FSK (A, w/o). The signals of the CHO D_2S isoform (A) without FSK and with FSK pre-stimulation (B) are distinguishable dependent on a pre-stimulation with FSK or not

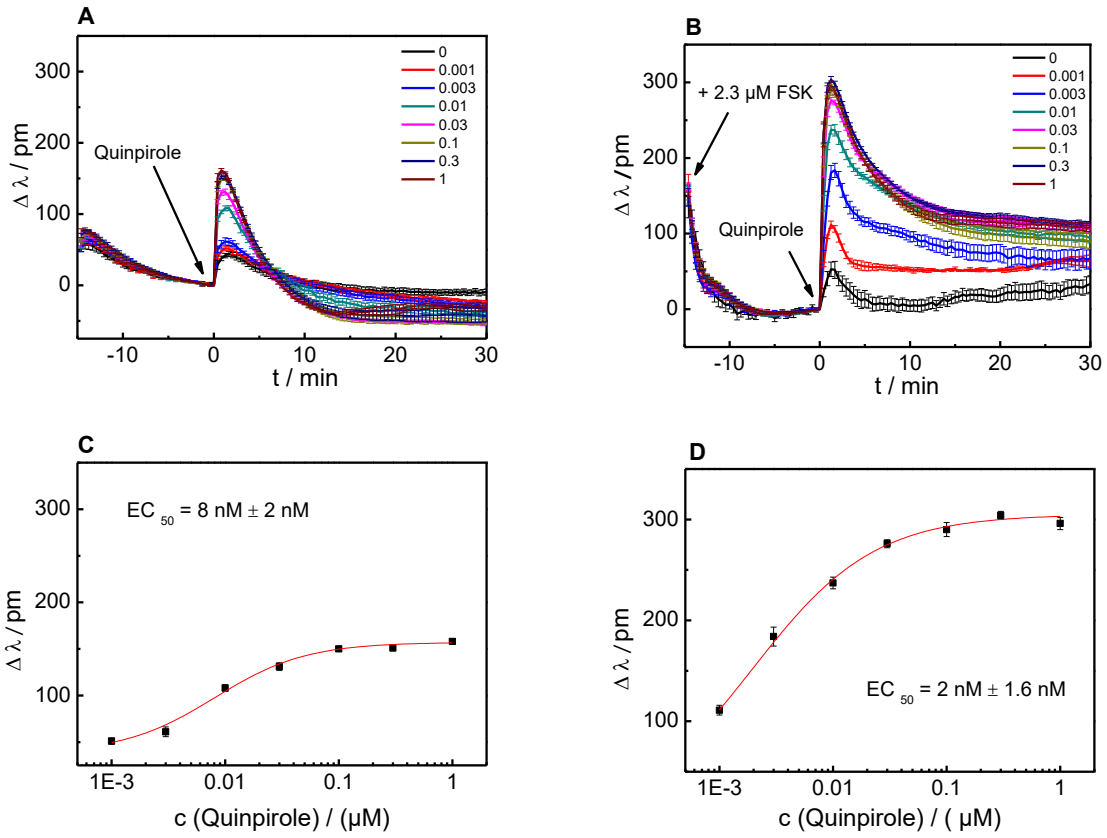

Fig. 4-55 Quinpirole (c = µM) induced response of CHO D_2S (short) cells without (**A, w/o**) and with FSK pre-stimulation (2.3 µM) (**B, w**) monitored by DMR (n≥3; mean ± SE). Below are the Concentration-response curves with the calculated EC_{50} values, **C (w/o)** for CHO D_2S (short) cells without and **D (w)** for CHO D_2S (short) with FSK pre-stimulation (2.3 µM).

CHO D_2L (long) / without (w/o) and with (w) FSK / Quinpirole / ECIS and DMR readout

Fig. 4-56 summarizes the impedance-based (ECIS) analysis when CHO D_2L (long) cells without (A, w/o) and with 0.5 µM FSK pre-stimulation (B, w) were exposed to increasing quinpirole concentrations. In both scenarios the cells show dose-dependent response profiles. Analysis of the impedance-based data provided EC_{50} values of (23 ± 4) nM for CHO cells expressing D_2L (long) without (C, w/o) and an EC_{50} value of (33 ± 7) nM for CHO D_2L (long) with FSK pre-stimulation (D, w) when quinpirole was used as an agonist. CHO D_2L-expressing cells (A, w/o) show no signal perturbation when pure medium was added to the cells to have a control on the cell reaction. CHO D_2L-expressing cells show signal maximum for quinpirole concentrations of 0.1 µM and higher within 2 minutes after stimulation (Δ IZI = 0.5 kΩ, for max. concentration of 3 µM quinpirole). The signals run through a transient minimum (t = 6 min., Δ IZI = 0.33 kΩ, for max. concentration of 3 µM quinpirole) followed by a second maximum (t = 12 min., IZI = 0.65 kΩ, for max. concentration of 3 µM quinpirole). The signals then become stationary at concentration-dependent values, forming a plateau till the end data akqusition (t =

30 min., Δ IZI = 0.60 Ω, for max. concentration of 3 µM quinpirole). CHO D_2L cells pre-stimulated with 0.5 µM FSK (B, w) show a massive signal drop of 0.8 kΩ within 5 minutes after FSK addition (0.5 µM). The next 5 minutes the signal decrease further by 0.20 kΩ. For the next 5 minutes and before quinpirole addition the signals decrease slightly (t = 0 min, Δ IZI = 0.02 kΩ). Quinpirole stimulation induced steep signal increase for concentrations of 0.1 µM quinpirole and higher within 4 minutes after stimulation (Δ IZI = 0.95 kΩ, for max. concentration of 3 µM quinpirole) followed by a further slight signal increases for 9 minutes (t = 13 min, with Δ IZI = 1.62 kΩ, for max. concentration of 3 µM quinpirole). The signals increase slightly till the end of data recording (t= 30 min., Δ IZI = 1.67 Ω, for max. concentration of 3 µM quinpirole). The CHO cells expressing isoform D_2L (long) shows significantly different signal patterns when the cells are prestimulated with FSK (0.5 µM) prior quinpirole stimulation compared to untreated cells.

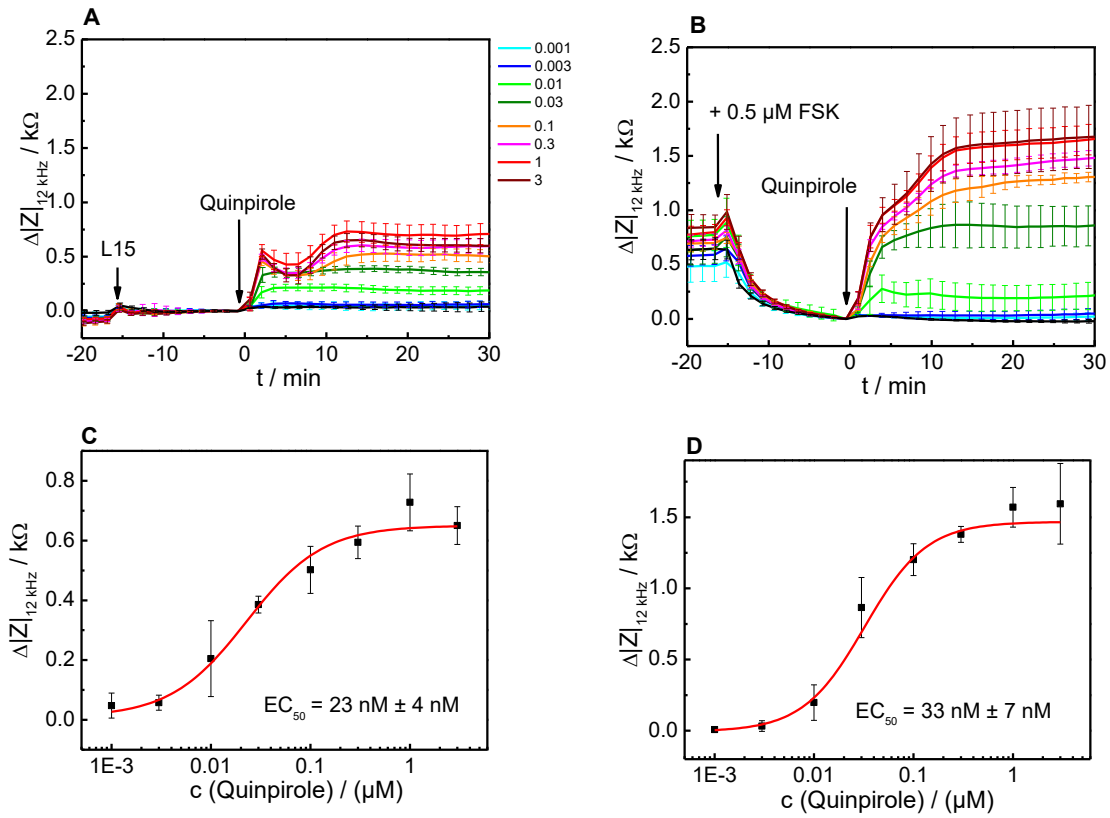

Fig. 4-56 Quinpirole (c = µM) induced response of CHO D_2L (long) cells without (**A, w/o**) and with FSK pre-stimulation (0.5 µM) (**B, w**) monitored by ECIS (96 W 20idf PET well array, Applied BioPhysics Inc.) (n≥ 3; mean ± SE). Below are the concentration-response curves with the calculated EC_{50} values, **C (w/o)** for CHO D_2L (long) cells without and **D (w)** for CHO D_2L (long) cells with FSK pre-stimulation (0.5 µM). Data provided by Dr. Judith Stolwijk (University Regensburg).

Fig. 4-57 shows DMR-based analysis when CHO D_2L (long) cells without (A, w/o) and with 0.5 µM FSK pre-stimulation (B, w) were exposed to increasing quinpirole concentrations. In both

scenarios time course analysis shows dose-dependent response profiles. Analysis of the DMR-based data provided EC_{50} values (66 ± 14) nM for D_2L (long) without (C, w/o) and EC_{50} values of (50 ± 7) nM for D_2L (long) cells with FSK pre-stimulation (D, w) when quinpirole is used as a ligand. D_2L expressing CHO cells (A, w/o) not exposed to FSK show for 15 minutes a drifting baseline of app. Δ λ = 60 pm. After quinpirole addition all signal maxima are reached within 1.25 minutes (for max. concentration of 1 µM quinpirole, Δ λ = 180 pm), followed by a signal drop for 12 min (for max. concentration of 1 µM quinpirole, t = 13.5 min, Δ λ = -18 pm). The signals then become stationary at concentration-dependent values for the rest of data recording. The signal show for all concentrations a similar signal pattern with concentration-dependent maximum (t = 1.25 min.). CHO expressing D_2L cells pre-stimulated with 0.5 µM FSK (B, w) show after FSK addition (0.5 µM) for 3 minutes a steep signal drop of app. 200 pm. The next 2 minutes the signal increases slightly for app. 10 pm. For the next 10 minutes the signal decrease again slightly for app. 60 pm (t = 0 min, Δ λ = 0 pm). After quinpirole addition all signal maxima are reached within 2 minutes (for max. concentration 1 of µM quinpirole, Δ λ = 415 pm,), followed by a signal drop for 10 min (for max. concentration 1of µM quinpirole, t = 12 min, Δ λ = 230 pm). High concentration of quinpirole show bigger signal maxima than low concentration. The signals shift then slightly, concentration-dependent, to smaller values till the end of data recording (for max. concentration of 1 µM quinpirole, t = 30 min., Δ λ = 210 pm). The signal shows for all concentrations a similar signal pattern with concentration-dependent maxima. FSK pre-stimulation of the CHO expressing isoform D_2L (B, w) cells provides a remarkable signal drop compared to the cells without FSK (A, w/o). After quinpirole addition differences in signal maxima, with two times higher Δ λ, are recorded for the FSK pre-stimulated CHO D_2L cells (B, w) compared to the cells without FSK (A, w/o). The signals of the CHO D_2L isoform (a) without FSK and (B) with FSK pre-stimulation are distinguishable dependent on a pre-stimulation with FSK or not.

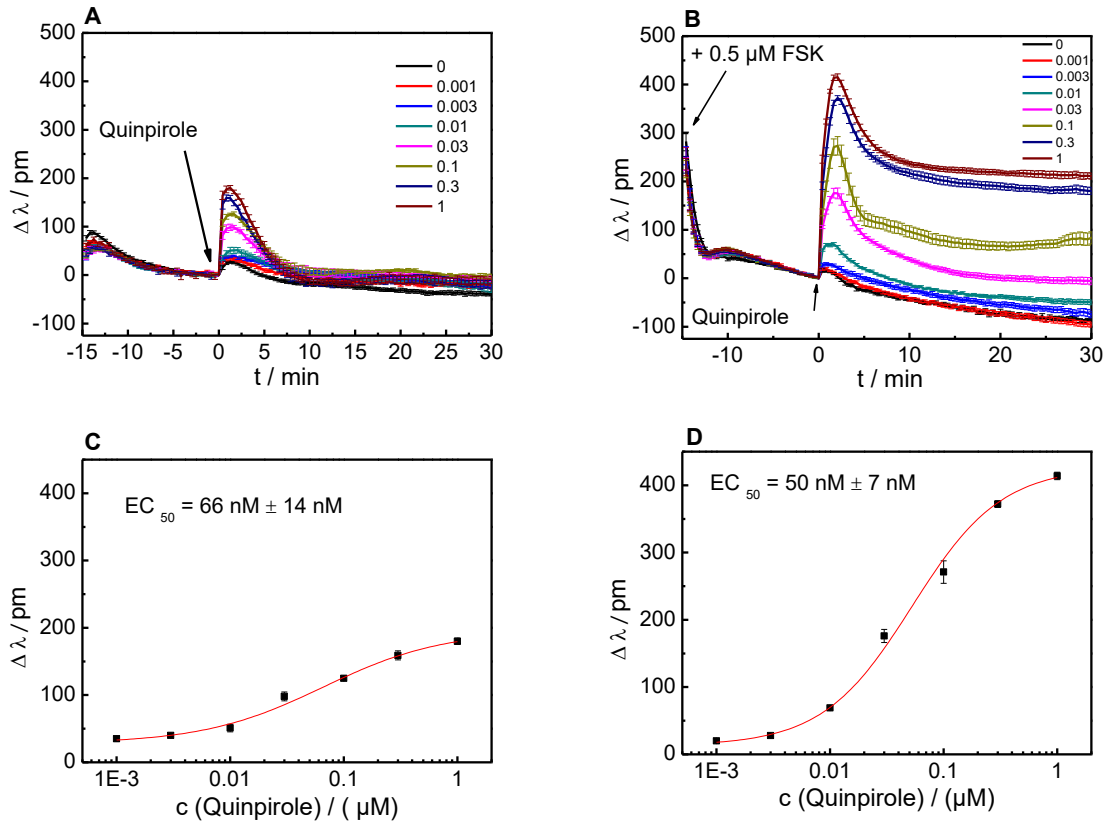

Fig. 4-57 Quinpirole (c = µM) induced response of CHO D_2L (long) cells without (**A, w/o**) and with FSK pre-stimulation (0.5 µM) (**B, w**) monitored by DMR (n≥ 3; mean ± SE). Below are the concentration-response curves with the calculated EC_{50} values, **C (w/o)** for CHO D_2L (long) cells without and **D (w)** for CHO D_2L (long) cells with FSK pre-stimulation (0.5 µM).

Agonist-Assay for D_2-Receptors: Correlating Label-Free readouts for the endogenous agonist Dopamine

It has been one of the major objectives of this thesis to check whether correlated datasets recorded with two entirely independent techniques may help to identify a signaling cascade just from label-free time response profiles. In order to check for the information content of such correlations, the ECIS and DMR data for the two receptor subtypes D_2R-S and D_2R-L are compared upon stimulation with the endogenous agonist dopamine. Similar to ECIS-SPR, the ECIS-DMR combination provides both, the dielectric signature of the signaling pathway which is mainly determined by cell shape (ECIS) and the dynamic mass redistribution signature (DMR) that goes along with that.

The following six data plots (Fig. 4-58 till Fig. 4-63) contain first original datasets (A and B in every Figure) and below the corresponding normalized data plots (C and D in every Figure) with agonist (dopamine, c = 1 µM) addition set to zero (0) and the maximum signal response set to one (1).

Fig. 4-58 compares the time-resolved response profiles of CHO cells expressing D_2S receptor (short) cells without pre-stimulation (A original dataset, below C normalized dataset) and the same CHO D_2S cells (short) with FSK pre-stimulation (2.3 µM) (B original dataset, below D normalized dataset) upon exposure to 1 µM dopamine. Black curves always show the ECIS readout while red curves show always the DMR readout.

Fig. 4-58 A ECIS, (black curve) shows a small impedance increase (t = -15 – 0 min, Δ IZI = 145 Ω) during baseline recording. Dopamine addition (t = 0, Δ IZI = 0 Ω) induces a signal increase reaching a maximum value (t = 3 min., Δ IZI = 448 Ω) followed by a signal decrease to a minimum (t = 8.5 min., Δ IZI = 380 Ω). The signal increases again slightly to a second and higher maximum till the end of data recording (t = 20 min, Δ IZI = 475 Ω). Fig. 4-58 A DMR (red curve) shows a signal drop (t = -15 – 0 min, Δ λ = 105 pm) during baseline recording. Dopamine addition (t = 0, Δ λ = 0 pm) induces a big signal increase reaching a maximum value (t = 2 min, Δ λ = 185 pm) followed by a massive signal drop to a minimum value (t = 16 min, Δ λ = 16 pm) and stays constant till the end of data recording (t = 20 min, Δ λ = 18 pm). Fig. 4-58 C shows the same plot as A but the maximum values are set to 1 (100%) and the minimum value to 0 (0 %) so that the signal changes are stretched. Fig. 4-58 B ECIS (black curve) shows a massive impedance decrease for 10 minutes (t = -15 – -5 min, Δ IZI = 1845 Ω) after FSK addition (2.3 µM) and reaches a stable baseline for the next 5 minutes. Dopamine addition (t = 0, Δ IZI = 0 Ω) induce a massive signal increase for 5 minutes that exceeds the value before FSK addition (t = 5 min., Δ IZI = 1860 Ω). The signal saturates and the impedance increases for just 220 Ω within the next 15 minutes till end of data recording (t = 20 min, Δ IZI = 2280 Ω). Fig. 4-58 B DMR (red curve) shows a baseline with a signal drop of 106 pm within 10 minutes after FSK addition (2.3 µM) and drifts towards a minimum (t = -15 – 0 min, Δ λ = 118 pm). Dopamine addition (t = 0, Δ λ = 0 pm) induces a big signal increase reaching a maximum value (t = 2 min, Δ λ = 202 pm) followed by a massive signal drop for 8 minutes (t = 10 min, Δ λ = 78 pm) which decreases further till the end of data recording (t = 20 min, Δ λ = 49 pm). Fig. 4-58 D shows the same plot as B but the maximum values are set to 1 (100%) and the minimum value to 0 (0 %) so the signal changes are stretched.

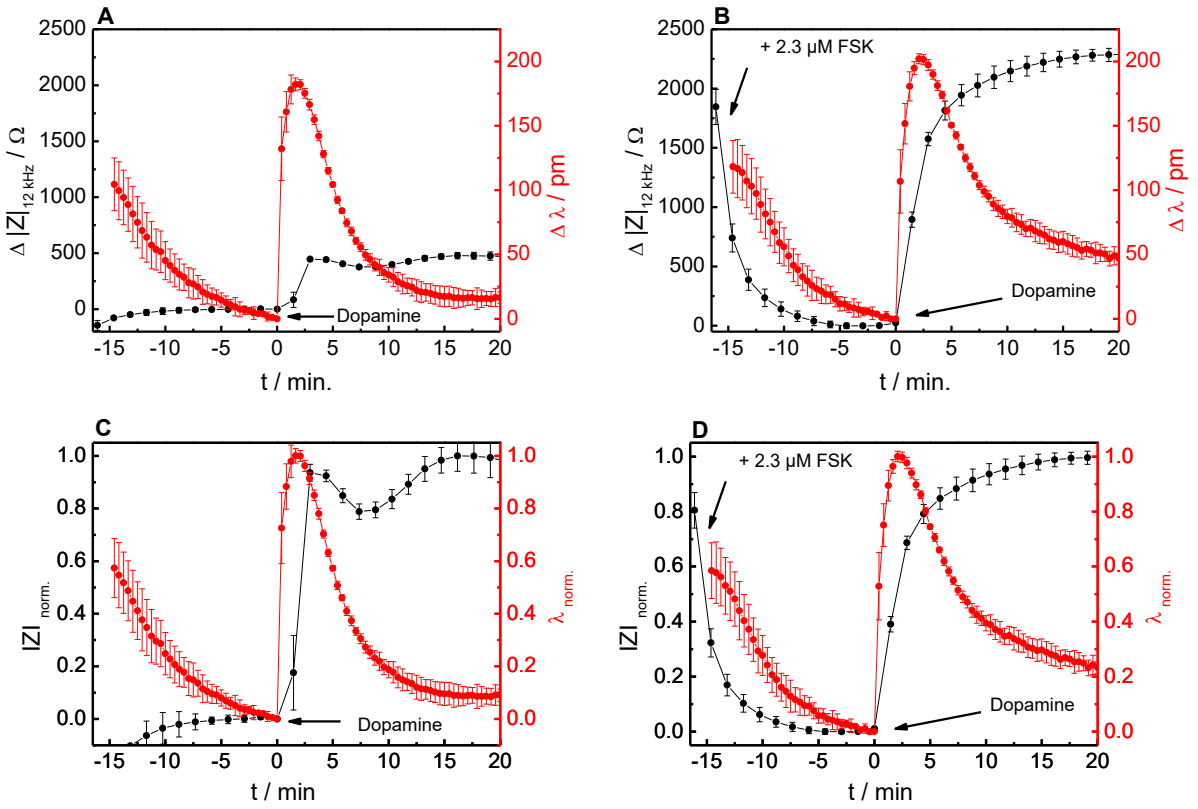

Fig. 4-58 (A, w/o) Dopamine (1 µM) induced response (black arrow t = 0 min) of CHO D_2S (short) cells without FSK pre-stimulation. Impedance-based (ECIS) readout (black curve, n≥3, mean ± SE, original dataset) and DMR based readout (red curve, n≥3, mean ± SE, original dataset) (ECIS black curve (from Fig. 4-50 A); DMR red curve (from Fig. 4-51 A)), without FSK (**C, w/o**) corresponding normalized datasets. **(B, w)** CHO D_2S (short) cells with FSK pre-stimulation (2.3 µM), followed by dopamine (1 µM, t = 0 min) stimulation (black arrow). Impedance-based (ECIS) readout (black curve, n≥3, mean ± SE) and DMR based readout (red curve, n≥3, mean ± SE, original dataset) (ECIS black curve (from Fig. 4-50 B); DMR red curve (from Fig. 4-51 B) with FSK prestimulation (2.3 µM) (**D, w**) corresponding normalized dataset.

Fig. 4-59 shows CHO D_2L (long) cells without pre-stimulation (A original dataset, below C normalized dataset) and CHO D_2L (long) with FSK pre-stimulation (0.5 µM) (B original dataset, below D normalized dataset) followed by 1 µM dopamine stimulation. Black curves always represent the ECIS readout while red curves show always DMR readout.

Fig. 4-59 A ECIS (black curve) shows a small impedance increase (t = -18 – 0 min, Δ IZI = 30 Ω) during baseline recording. Dopamine addition (t = 0, Δ IZI = 0 Ω) induces a signal increase reaching a maximum value (t = 1.5 min., Δ IZI = 799 Ω) followed by a signal decrease to a minimum (t = 5.5 min., Δ IZI = 515 Ω). The signal increases further to a second and higher maximum (t = 13.5 min, Δ IZI = 1024 Ω). The signal then decreases till the end of data recording (t = 20 min, Δ IZI = 986 Ω). Fig. 4-59 A DMR (red curve) shows a signal drop (t = -15 – 0 min, Δ λ = 98 pm) during baseline recording. Dopamine addition (t = 0, Δ λ = 0 pm) induces a big signal increase reaching a maximum value (t = 1.5 min, Δ λ = 295 pm) followed by a massive signal drop to a minimum value (t = 13.5 min, Δ λ = 85 pm) and increase slightly till the end of data recording (t = 20 min, Δ λ = 95 pm). Fig. 4-59 C shows the same plot as A but the maximum values are set to 1 (100%) and the minimum value to 0 (0 %) so the signal

changes appear stretched. Fig. 4-59 B ECIS (black curve) shows a massive impedance decrease for 13 minutes (t = -18 – -5 min, Δ IZI = 1751 Ω) after FSK addition (0.5 µM) that reaches a stable baseline for the next 5 minutes. Dopamine addition (t = 0, Δ IZI = 0 Ω) induces a massive signal increase for 5 minutes and exceeds the values before FSK addition (t = 5 min., Δ IZI = 1815 Ω). The signal increases by 850 Ω within the next 7 minutes (t = 12 min, Δ IZI = 2655 Ω). The signal then increases only slightly till the end of data recording (t = 20 min, Δ IZI = 2754 Ω). Fig. 4-59 B DMR (red curve) shows a baseline with a signal drop of 150 pm within 5 minutes (t = -15 – -10 min, Δ λ = 150 pm) after FSK addition (0.5 µM) and drifts towards a minimum (t = -10 – 0 min, Δ λ = 48 pm). Dopamine addition (t = 0, Δ λ = 0 pm) induces a big signal increase reaching a maximum value (t = 2.5 min, Δ λ = 484 pm) followed by a signal drop for 8 minutes (t = 10.5 min, Δ λ = 305 pm) and stays nearly constant till the end of data recording (t = 20 min, Δ λ = 300 pm). Fig. 4-59 D shows the same plot as B but the maximum values are set to 1 (100%) and the minimum value to 0 (0 %) so the signal changes appear stretched.

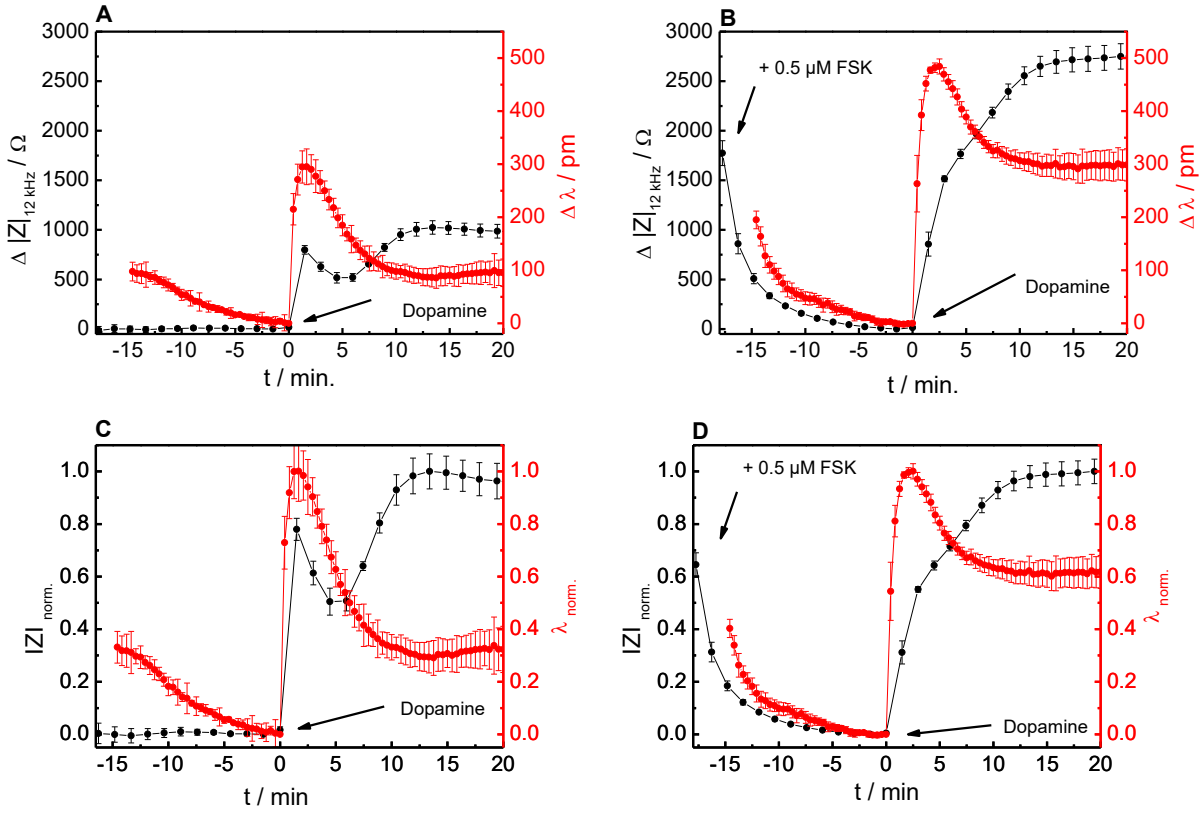

Fig. 4-59 (**A, w/o**) Dopamine (1 µM) induced response (black arrow t = 0 min) of CHO D_2L (long) cells without FSK pre-stimulation. Impedance based (ECIS) readout (black curve, n≥3, mean ± SE, original dataset) and DMR based readout (red curve, n≥3, mean ± SE, original dataset) (ECIS black curve (from Fig. 4-52 A); DMR red curve (from Fig. 4-53 A)) without FSK (**C, w/o**) corresponding normalized datasets. (**B, w**) CHO D_2L (long) cells with FSK pre-stimulation (0.5 µM), followed by dopamine (1 µM, t= 0 min) stimulation (black arrow). Impedance based readout (black curve, n≥3, mean ± SE) and DMR based readout (red curve, n≥3, mean ± SE, original dataset) (ECIS black curve (from Fig. 4-52 B); DMR red curve (from Fig. 4-53 B) with (**D, w**) corresponding normalized dataset.

Fig. 4-58 the signals of the impedance-based readout (ECIS, black curves) for CHO-expressing D_2S (short) cells without (A and C) and with FSK pre-stimulation (2.3 µM) (B and D) prior dopamine stimulation provide significantly different signal pattern dependent on FSK pre-stimulation or not. Fig. 4-58 the DMR-based readout (DMR, red curves) for CHO-expressing D_2S (short) cells without (A and C) and with FSK pre-stimulation (2.3 µM) (B and D) prior dopamine stimulation does not provide major differences for the recorded signal pattern independently on FSK pre-stimulation or not. Fig. 4-59 the signals of the impedance-based readout (ECIS, black curves) for CHO-expressing D_2L (long) cells without (A and C) and with FSK pre-stimulation (0.5 µM) (B and D) prior dopamine stimulation provide significantly different signal pattern dependent on FSK pre-stimulation or not. Fig. 4-59 the DMR-based readout (DMR, red curves) for CHO-expressing D_2L (long) cells without (A and C) and with FSK pre-stimulation (0.5 µM) (B and D) prior dopamine stimulation provide major differences for the recorded signal pattern dependent on FSK pre-stimulation or not.

Agonist-Assays for the D_2-Receptor: Comparing ECIS-DMR and ECIS-SPR Readouts

The final differentiation was to check separately recorded ECIS and DMR datasets for the two receptor subtypes D_2R-S and D_2R-L with pre-stimulation by FSK followed by stimulation with the endogenous agonist dopamine for correlations with identically but simultaneously performed experiments using the dual ECIS-SPR sensor platform.

Fig. 4-60 A and C shows CHO D_2S (short) cells with FSK pre-stimulation (2.3 µM) followed by dopamine stimulation (1 µM). Black curves always show ECIS readout while red curves show always DMR readout (A original dataset, below C normalized dataset). Fig. 4-60 (ECIS-SPR sensor) B and D shows CHO D_2S (short) cells with FSK pre-stimulation (2.3 µM) followed by dopamine stimulation. Black curves always show ECIS readout while red curves show always the simultaneously recorded SPR readout (B original dataset, below D normalized dataset).

In Fig. 4-60 A ECIS (black curve) shows a massive impedance decrease for 10 minutes (t = -15 – -5 min, Δ |Z| = 1845 Ω) after FSK addition (2.3 µM) before impedance reaches a stable baseline for the next 5 minutes. Dopamine addition (t = 0, Δ |Z| = 0 Ω) induce a massive signal increase for 5 minutes that exceeds the value before FSK addition (t = 5 min., Δ |Z| = 1860 Ω). The signal saturates and the impedance slightly increases for 220 Ω within the next 15 minutes till the end of data recording (t = 20 min, Δ |Z| = 2280 Ω). In Fig. 4-60 A the DMR (red curve) shows a baseline with a signal drop of 106 pm within 10 minutes after FSK addition (2.3 µM) and drifts towards a minimum (t = -15 – 0 min, Δ λ = 118 pm). Dopamine addition (t = 0, Δ

λ = 0 pm) induces a big signal increase reaching a maximum value (t = 2 min, Δ λ = 202 pm) followed by a massive signal drop for 8 minutes (t = 10 min, Δ λ = 78 pm) and a decrease describing a flattening curve till the end of data recording (t = 20 min, Δ λ = 49 pm). Fig. 4-60 C shows the same plot as A but the maximum values are set to 1 (100%) and the minimum value to 0 (0 %). In Fig. 4-60 B ECIS (black curve) shows a step signal increase after FSK addition (2.3 µM) within 20 seconds with an impedance increase of 12 Ω. The signal drops for the next 3.5 minutes for 65 Ω (t = -10.5, Δ IZI = 15 Ω) and describes then a flattening curve for 7 minutes (t= -3 min, Δ IZI = 0.2 Ω). The curve shows a small signal increase after aspirating medium out of the reaction chamber before dopamine addition (t = 0, Δ IZI = 3.8 Ω). Dopamine addition shows a minimal addition peak within 20 seconds with a impedance increase of 5 Ω, followed by a massive signal increase for 3.5 minutes and impedance increases of 83 Ω (t = 3.8 min, Δ IZI = 88.4 Ω). The signal describes then a flattening curve for rest of recording time, while impedance increases slightly till the end of data recording (t = 20 min., Δ IZI = 110 Ω). In Fig. 4-60 B SPR (red curve) shows a steep signal increase after FSK addition (2.3 µM) within 20 seconds with a reflectivity increase of 26 R.U.. The signal drops for the next 4 minutes for 135 R.U. (t = -10.5, Δ R = 7 R.U.) and describes then a flattening curve for 7 minutes, reaches a minimum (t = - 3 min, Δ R = -3.5 R.U.) and increases slightly till dopamine addition (t = 0 min, Δ R = 0 R.U.). Dopamine addition induces a steep signal increase and reaches a maximum value (t = 2.7 min, Δ R = 231.5 R.U.) followed by a signal decrease for 6.7 minutes and a signal drop of 69 R.U., and reaches a minimum (t = 9.4 min, Δ R = 162.2 R.U.). The signal increases slightly for the rest of data recording (t = 20 min, Δ R = 177 R.U.). Fig. 4-60 D shows the same plot as B but the maximum values are set to 1 (100%) and the minimum value to 0 (0 %).

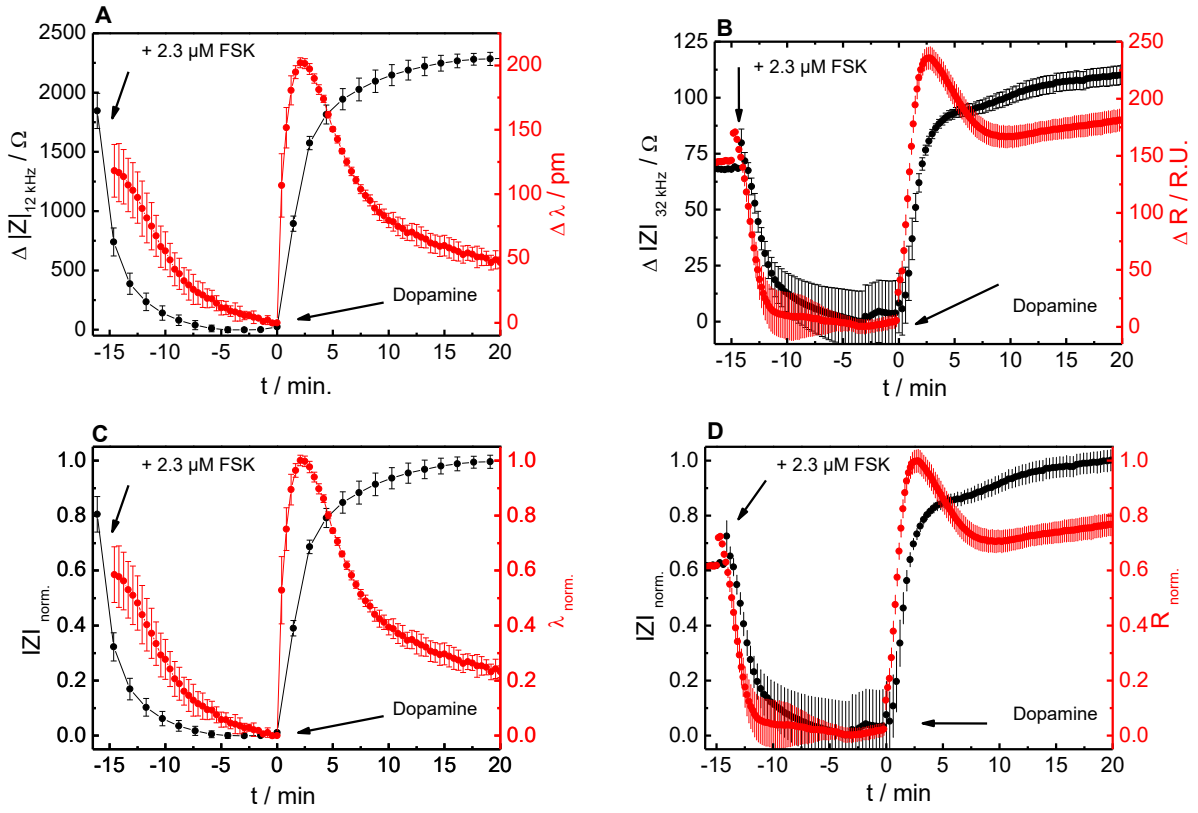

Fig. 4-60 (A) CHO D_2S (short) cells with FSK pre-stimulation (2.3 µM, black arrow) followed by dopamine (1 µM) stimulation (black arrow). Impedance-based (ECIS) readout (black curve, n≥3), mean ± SE and DMR-based readout (red curve, n≥3, mean ± SE) below (**C**) corresponding normalized datasets. (**B**) CHO D_2S (short) cells with FSK pre-stimulation (2.3 µM, black arrow) followed by dopamine (1 µM) stimulation (black arrow) recorded with the dual ECIS-SPR sensor. Impedance-based (ECIS) readout (black curve, n=4, mean ± SE) and SPR-based readout (red curve, n=4, mean ± SE) below (**D**) corresponding normalized datasets.

Fig. 4-61 A and C show CHO D_2L (long) cells with FSK pre-stimulation (0.5 µM) followed by dopamine (c = 1 µM) stimulation. Black curves always show ECIS readout while red curves show always DMR readout (A original dataset, below C normalized dataset). Fig. 4-61 B and D show CHO D_2L (long) cells with FSK pre-stimulation (0.5 µM) followed by dopamine (c = 1 µM) stimulation. Black curves always show ECIS readout while red curves show always simultaneously recorded SPR readout (B original dataset, below D normalized dataset).

In Fig. 4-61 A ECIS (black curve) shows a massive impedance decrease for 13 minutes (t = -18 – -5 min, Δ IZI = 1751 Ω) after FSK addition (0.5 µM) and reaches a stable baseline for the next 5 minutes. Dopamine addition (t = 0, Δ IZI = 0 Ω) induces a massive signal increase for 5 minutes and exceeds the value before FSK addition (t = 5 min., Δ IZI = 1815 Ω). The signal increases by 850 Ω within the next 7 minutes (t = 12 min, Δ IZI = 2655 Ω). The signal increases only slightly till the end of data recording (t = 20 min, Δ IZI = 2754 Ω). In Fig. 4-61 A DMR (red curve) shows a baseline with a signal drop of 150 pm within 5 minutes (t = -15 – -10 min, Δ λ = 150 pm) after FSK addition (0.5 µM) and it drifts towards a minimum (t = -10 – 0

min, Δ λ = 48 pm). Dopamine addition (t = 0, λ = 0 pm) induces a big signal increase reaching a maximum value (t = 2.5 min, Δ λ = 484 pm) followed by a signal drop for 8 minutes (t = 10.5 min, Δ λ = 305 pm) and stays nearly constant till the end of data recording (t = 20 min, Δ λ = 300 pm). Fig. 4-61 C shows the same plot as A but the maximum values are set to 1 (100%) and the minimum value to 0 (0 %). Fig. 4-61 B ECIS (black curve) shows a steep signal increase after FSK addition (2.3 µM) within 30 seconds with an impedance increase of 14 Ω. The signal drops for the next 3.5 minutes for 116 Ω (t = -10.5, Δ IZI = 20 Ω) and describes then a flattening curve for 7 minutes (t= -3 min, Δ IZI = -3 Ω). The curve shows a small signal increase after aspirating the media out of the reaction chamber before dopamine addition (t = 0, Δ IZI = 0 Ω). Dopamine addition shows an addition peak within 40 seconds with a impedance increase of 12 Ω, stays constant for further 40 seconds followed by a massive signal increase for 4.7 minutes and impedance increases by 114.5 Ω (t = 6 min, Δ IZI = 126.5 Ω). The signal increases for the next 6 minutes for further by 38 Ω (t = 12 min, Δ IZI = 164.5 Ω) and describes then a flattening curve for rest of recording time, while impedance increases slightly till the end of data recording (t = 20 min., Δ IZI = 172 Ω). Fig. 4-61 B SPR (red curve) shows a steep signal increase after FSK addition (2.3 µM) within 15 seconds with a reflectivity increase of 72 R.U.. The signal drops for the next 2.5 minutes for 342 R.U. reaching a minimum (t = -12, Δ R = 0 R.U.) The signal increases for the next 7 minutes and reflectivity increases by 75 R.U. (t = -5, Δ R = 75 R.U.) and describes then a flattening curve for 5 minutes increasing slightly till dopamine addition (t = 0 min, Δ R = 84 R.U.). Dopamine addition induces a steep signal increase and reaches a first maximum value (t = 2.3 min, Δ R = 318 R.U.), followed by a minimal signal dip with a minimum (t = 3.1 min, Δ R = 315 R.U.) and reaches a second maximum (t = 4.1 min, Δ R = 322 R.U.). The signal decreases for 4 minutes by 72 R.U. and reaches a minimum (t = 8 min, Δ R = 246 R.U.). The signal increase for 4 minutes again with a reflectivity increase by 24 R.U. (t = 12 min, Δ R = 270 R.U.). The signal increases slightly for the rest of data recording (t = 20 min, Δ R = 279 R.U.). Fig. 4-61 D shows the same plot as B but the maximum values are set to 1 (100%) and the minimum value to 0 (0 %).

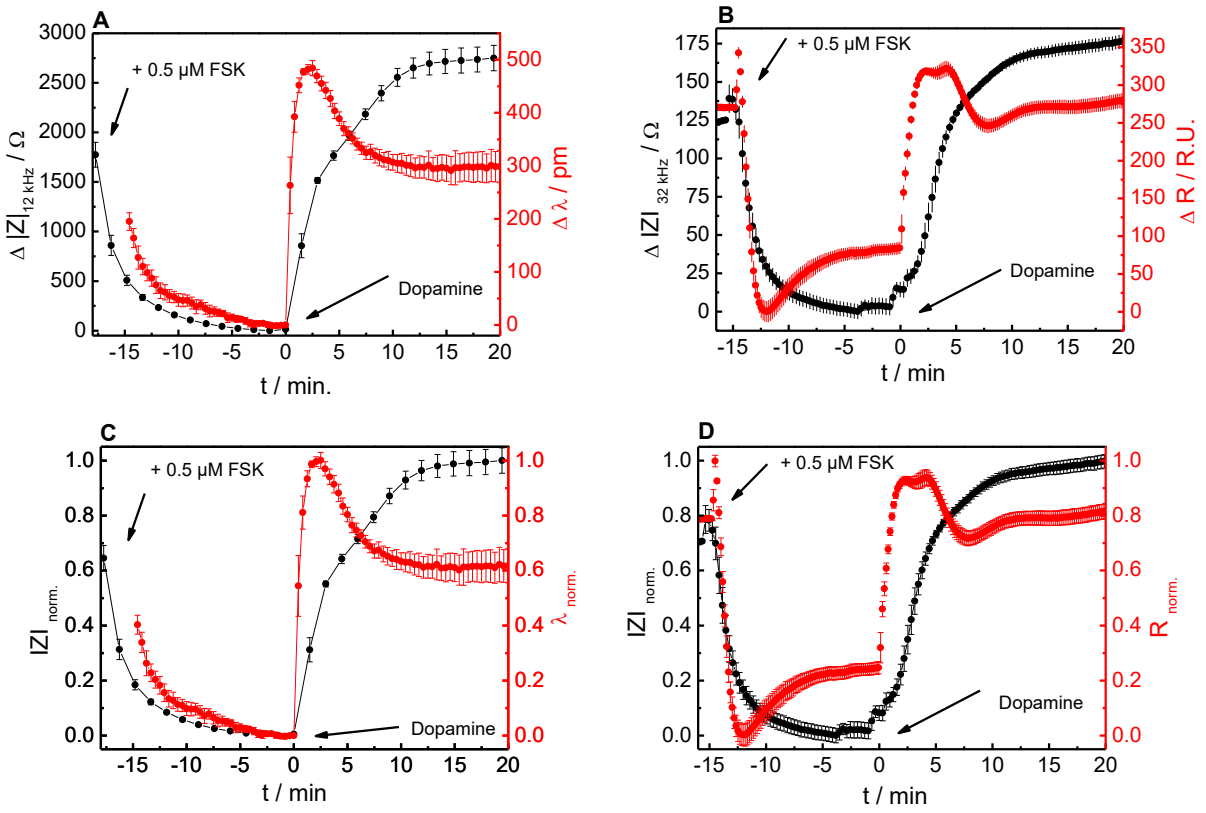

Fig. 4-61 (A) CHO D_2L (long) cells with FSK pre-stimulation (0.5 µM, black arrow) followed by dopamine (1 µM) stimulation (black arrow). Impedance-based (ECIS) readout (black curve, n≥3, mean ± SE) and DMR-based readout (red curve, n≥3, mean ± SE) below (**C**) Corresponding normalized datasets. (**B**) CHO D_2L (long) cells with FSK pre-stimulation (0.5 µM, black arrow) followed by dopamine (1 µM) stimulation (black arrow) recorded with the dual ECIS-SPR sensor. Impedance based readout (black curve, n=4, mean ± SE) and SPR based readout (red curve, n=4, mean ± SE) below (**D**) corresponding normalized datasets.

Comparing the two receptor isoforms D_2S (short) and D_2L (long) by ECIS-DMR profiles

Fig. 4-62 opposes time-resolved response profiles of CHO D_2S and CHO D_2L cells pre-stimulated with FSK followed by dopamine (c = 1 µM) addition recorded with the ECIS and DMR readouts. The signal responses for the two isoforms are compared to show the differences of the signal pattern. DMR for the CHO D_2L isoform (Fig. 4-62 B, red curve) show overall a more remarkable reaction to FSK addition and a much more higher signal response after dopamine addition compared to the CHO D_2S isoform (Fig. 4-62 A, red curve). The starting values for the baseline after FSK addition and the pattern are distinguishable. The signal increases for both isoforms but the pattern following the maximum value are different. The ECIS signal patterns for the two isoforms (Fig. 4-62, A = D_2S, B = D_2L, black curves) show only differences after dopamine addition as the signal increase over the starting value before FSK prestimulation for the D_2L isoforms. The normalized datasets (Fig. 4-62 C = D_2S, D = D_2L) provide a different view but although indicate small differences for the signal pattern.

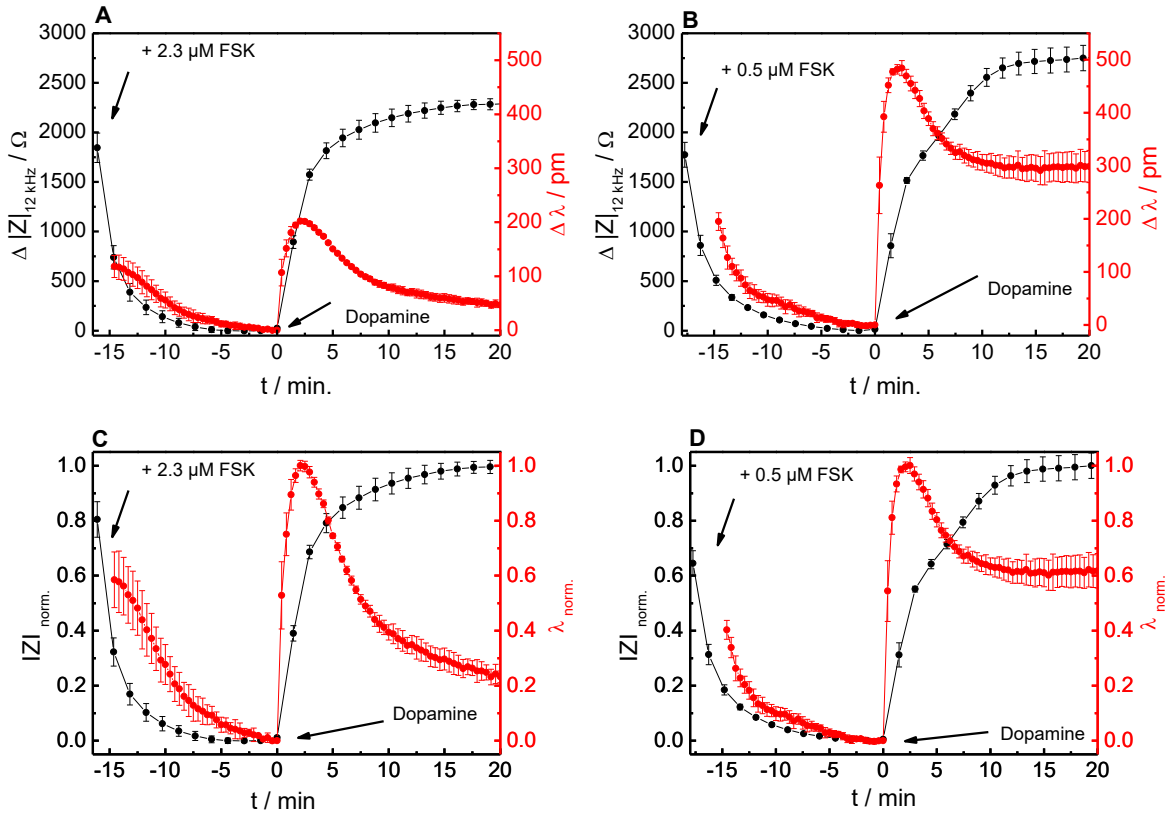

Fig. 4-62 shows dopamine induced response of CHO D_2S (short) cells (**A** and **C**) with FSK pre-stimulation (2.3 µM) and CHO D_2L (long) cells (**B** and **D**) with FSK pre-stimulation (0.5 µM) recorded by ECIS (black curves) and DMR (red curves). **A** and **B** are original datasets and **C** and **D** are the corresponding normalized data plots.

Comparing the two receptor isoforms D_2S (short) and D_2L (long) by ECIS-SPR profiles

Fig. 4-63 opposes CHO D_2S and CHO D_2L cells prestimulated with FSK followed by dopamine addition recorded with the ECIS-SPR sensor. The signal responses for the two isoforms are compared to show the differences of the signal pattern. The SPR response for CHO D_2L isoform (Fig. 4-63 B, red curve) show overall a much more remarkable reaction to FSK addition and dopamine stimulation compared to the CHO D_2S isoform (Fig. 4-63 A, red curve). The signals after dopamine addition provide a significant fingerprint for each isoform due to the different signals after passing the absolute maxima. The ECIS signal patterns for the two isoforms (Fig. 4-62, A = D_2S, B = D_2L, black curves) show differences in the impedance intensity and after dopamine addition as the signal increase shows differences. The normalized datasets (Fig. 4-62 C = D_2S, D = D_2L) provide a different view but also indicate the previously described differences for the signal pattern.

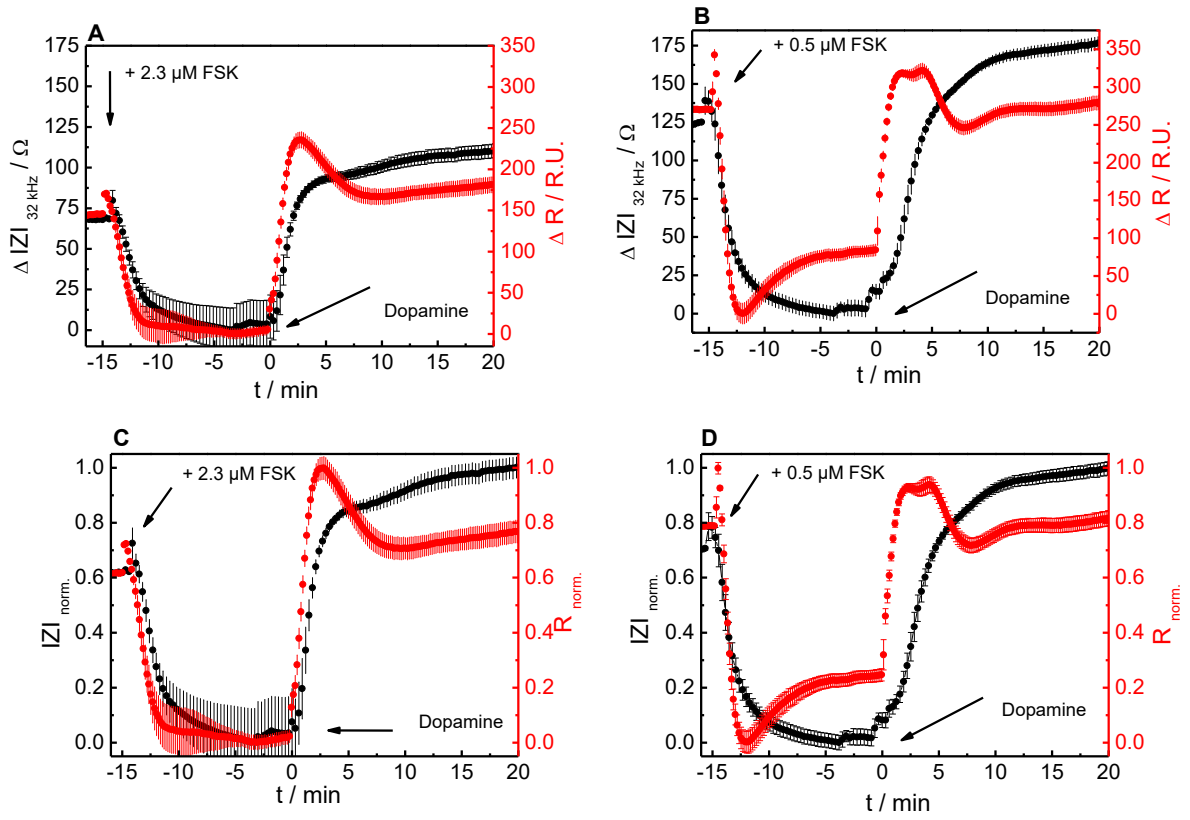

Fig. 4-63 shows dopamine induced response of CHO D_2S (short) cells (**A** and **C**) with FSK pre-stimulation (2.3 µM) and CHO D_2L (long) cells (**B** and **D**) with FSK pre-stimulation (0.5 µM) recorded by the dual ECIS-SPR sensor (ECIS, black curves; SPR red curves). **A** and **B** are original datasets and **C** and **D** are the corresponding normalized data plots

4.4.3 Discussion

The human glioblastoma cell line U-373 MG, expressing endogenously the $_hH_1$ receptor, was first used as model cell line for establishing a functional assay format for label-free analysis of GPCR signal transduction on dual ECIS-SPR sensor and was basement for the further experiments with the dual ECIS-SPR sensor (4.1).

The first part of dose response analysis for the endogenously expressed $_hH_1$ receptor in U-373 MG cells was performed with the endogenous agonist histamine (4.4.1.1). The first results show single experiments, performed with the dual ECIS-SPR sensor for increasing histamine concentrations. The dose response dependency could be shown and analyzed for both readouts methods. The experiments provided for both label-free readouts (dual ECIS-SPR sensor) EC_{50} values confirming each other: ECIS: EC_{50} = (0.48 ± 0.05) µM histamine; SPR: EC_{50} = (0.54 ± 0.04) µM histamine. Similar literature studies separately performed with the label-free readout methods (ECIS and DMR (RWG)) on U-373 MG cells have shown for dose

response investigations similar EC_{50} values: ECIS: EC_{50} = (0.30 ± 0.06) µM histamine; DMR: EC_{50} = (0.76 ± 0.18) µM histamine, [108]; ECIS: EC_{50} = (0.42 ± 0.06) µM histamine, [105].

To increase the throughput the agonist was successively added onto the same cell layer on the dual ECIS-SPR sensor. The method was successfully performed on commercial ECIS devices and inspired by pharmacological whole organs studies [105], but had to be modified to guarantee a reliable method, for the dual ECIS-SPR sensor platform. Performing single experiments (no serial dosing) with the model cell line (U-373 MG) for dose dependency experiments, one complete day was necessary with four cell layers to perform one dose response dependency, as for every histamine concentration one separate cell layer was necessary. The successive serial addition of the agonist histamine provided the possibility to increase the throughput fourfold for one day. Successive, serial histamine addition onto the same cell layer provided higher EC_{50} values: ECIS: EC_{50} = (0.79 ± 0.10) µM histamine; SPR: EC_{50} = (1.08 ± 0.23) µM histamine, n≥4 but very similar to successive, serial histamine addition performance for the assay on commercial ECIS devices (successive addition ECIS: EC_{50} = (0.8 ± 0.08) µM, [105]). The successive agonist addition onto the same cell layer has several significant advantages, compared to single experiment performance and provides in addition similar results. 1. The throughput increases (fourfold). 2. The economical factor as the reduction of costs and time for substrate production and application for the ECIS-SPR sensor drop. 3. The consumption of raw materials and the associated preliminary work in cell culture lab for the cell preparation drop.

The second part of dose response analysis for the endogenously expressed $_hH_1$ receptor in U-373 MG cells was performed with the synthetic agonist UR-KUM 530 (4.4.1.1). The results show single experiments performed with the dual ECIS-SPR sensor for increasing concentrations. The dose response dependency could be shown and calculated for both readouts methods. The experiments provided EC_{50} values for both label-free readouts: ECIS: EC_{50} = (0.06 ± 0.03) µM UR-KUM 530; SPR: EC_{50} = (0.12 ± 0.03) µM UR-KUM 530.

Comparing the results for endogenous agonist (histamine) and synthetic agonist (UR KUM 530) in terms of potency, UR KUM 530 showed higher potency for ECIS (8 fold) and SPR (4.5 fold). Regarding the efficacy of the two agonists, UR KUM 530 showed a lower efficacy for ECIS but a higher for SPR compared to histamine. Studies separately performed with the label-free readout methods (ECIS and DMR (RWG)) for genetically engineered HEK293T cells expressing the $_hH_1$ receptor have been performed with UR-KUM 530 for EC_{50} determination (ECIS: EC_{50} = (0.003 ± 0.0007) µM UR-KUM 530; DMR: EC_{50} = (0.010 ± 0.002) µM UR-KUM 530) [109]. The same cell line (engineered HEK293T) was investigated with the label-free readout methods (ECIS and DMR) with histamine for EC_{50} determination (ECIS: EC_{50} = (0.012 ± 0.005) µM histamine; DMR: EC_{50} = (0.033 ± 0.006) µM histamine) [109].

The dual ECIS-SPR sensor does not provide significant differences in signal pattern for U-373 MG stimulated with histamine and KUM 530, only differences for the calculated EC_{50} values are to mention. For both ligands the same receptor with the following signal transduction is activated. Differences can be seen in the potency but not in efficacy for the two ligands used for this cell system.

Deconvolution of the signalling cascade was performed using the ionophor *calcimycin* (*A23187*), i.e. a pharmacological tool, which makes the plasma membrane permeable for Ca^{2+} and mimics thereby the $G_{\alpha q/11}$ pathway. Ca^{2+} ions are released in the signalling cascade mediated by $G_{\alpha q/11}$ and induced by $_hH_1$ receptor activation by histamine. Ca^{2+} plays a huge role itself, is a second messenger needed for activation of protein kinase C, which (PKC) is involved in a bewildering array of biological processes [110]. The ionophor A23187 (*calcimycin*) has a wide range of applications by increasing intracellular artificially Ca^{2+} levels, like investigations on vascular endothelial growth factor (VEGF) secretion in different cells [111-113]. The results for histamine and *calcimycine* stimulation of U-373 MG cells are detailed in chapter 4.4.1.2. Results for the SPR recording (Fig. 4-40 SPR) show similar signal response for the stimulation of the U-373 MG model cell line with the agonist histamine and the ionophor *calcimycin*. The histamine provided for SPR readout the expected signal pattern with a maximum of Δ R = 280 R.U. at 2:15 min followed by a minimum and a second shoulder. The stimulation with the ionophor (*calcimycine*) described a signal delay 15 second after calcimycin addition with a signal plateau for 25 further seconds. The signal increase describes a smaller gradient after 40 seconds compared with the signal increase after histamine stimulation. The peak value occurs at 3:45 min with Δ R = 208 R.U.. The assumed mechanism of the ionophor gives a possibility for signal explanation. The ionophor is first integrated into the plasma membrane and then it shuttles selectively Ca^{2+} ions from the cell medium via membrane into the cytosol of the cell, where Ca^{2+} acts as second messenger. The integration of the ionophor into the membrane takes a certain, unknown time to happen. The $G_{\alpha q/11}$ signal transduction, activated via the $_hH_1$ receptor, increases the Ca^{2+} (second messenger) concentration within the cytosol and so does the calcimycin in a different way. It is to assume that the mechanistic way of GPCR activation goes much faster than the calcium increase inside the cytosol via ionophor. This might be a possibility to explanation for the recorded signal delay for *calcimycin*. Secondly the signal for *calcimycine* shows a minimum 30 seconds later than the histamine response minimum which could be caused by the previous mentioned ionophor integration into the membrane. The third difference in signal pattern is that the *calcimycin* signal has no second shoulder after the minimum, instead the signal increases till the end of data recording to a higher value compared to histamine stimulation. Similar behaviour is shown for the ECIS readout (Fig. 4-41 ECIS) with histamine and *calcimycin*. The histamine induced signal dip occurs more than two times faster and shows a two times larger

signal dip compared to the *calcimycine* induced signal. The histamine signal shows a maximum after 15 minutes then the signal starts decreasing while the *calcimycin* signal shows after 15 minute a smaller but constant signal increase till the end of data recording. For the ECIS and the SPR the histamine induced signal declines after 15 minutes, which differs from the *calcimycine* induced signal pattern as the ionophor stays in the membrane integrated and the signals increase for both readouts till the end of data recording time.

A further pharmacological tool was BAPTA-AM, an intracellular chelator of Ca^{2+}. The results of the recording with the dual ECIS-SPR sensor show three curves for each of the two readouts (ECIS and SPR). Two control experiments and one actual experiment containing BAPTA-AM (intracellular Ca^{2+} chelator) (Fig. 4-42) followed by histamine stimulation for all three experiments. The first experiment (blind control) shows that the addition of L15/DMSO to the U-373 MG cells has no major influence on the signal pattern, as after histamine addition a signal occurs similar to previously recorded histamine cell stimulations. The main difference for the SPR signal is the small signal intensity of this experiment. ECIS provides previously shown signal intensity (Fig. 4-37). The control with the cells being pre-incubated with sulfinpyrazone/Pluronic® F-127 showed for the SPR readout a similar and for the ECIS readouts a similar signal pattern to the L 15/DMSO preincubated cells of the before described experiment. This indicates that the incubation with sulfinpyrazone/Pluronic® F-127 has no major influence on the signal transduction on the $G_{\alpha q/11}$ pathway when the cells get afterwards stimulated with histamine. The incubation of the cells with sulfinpyrazone/ Pluronic® F-127 and BAPTA-AM suppressed the typical signal pattern after agonist addition in the ECIS readout and showed a tendency of supressed signal pattern for the SPR readout. The results for the BAPT-AM prestimulation of U-373 MG followed by histamine stimulation lead to the assumption that Ca^{2+} has been complexed inside the cell and could not act as second messenger subsequently. According to pharmacology textbooks Ca^{2+} is released from the endoplasmatic reticulum after $_hH_1$ receptor activation by histamine and acts as second messenger. Histamine and UR-KUM 530 induced similar signal patterns on the dual ECIS-SPR sensor. Both label free techniques showed for an artificial Ca^{2+} increase (ionophor Calcimycin) and artificial Ca^{2+} suppression (BAPTA-AM, intracellular chelator) distinguishable signal patterns, thereby Ca^{2+} release can be seen as predominant part of the signal pattern recorded with the dual ECIS-SPR sensor.

The dual ECIS-SPR sensor provides different physical properties of the cell layer, but through the readout of the identical cell layer it provides the advantage to compare the signals exactly (4.4.1.2). The minima and maxima of the impedance based and of the optical based readout (U-373 MG) occur at different time points (Fig. 4-43). The histamine induced ECIS based signal pattern, with a minimum followed by a signal increase with a maximum and a

subsequent signal decrease, is similar to previously released studies [105, 108]. The optical SPR readout provided for histamine stimulation a biphasic signal increase with a maximum followed by a minimum and a second maximum and a subsequent signal decrease, a similar signal pattern was also observed by the optical DMR readout [108] for histamine induced stimulation of U-373 MG cells. A major part for the reflectivity change should be caused by the increase of cytosolic Ca^{2+} due to $_hH_1$ receptor activation, resulting in a change of the cytosolic composition close to the surface leading to a reflectivity change. This was also a result for the SPR simulations (4.2.1.5). As main part of the ECIS impedance change also Ca^{2+} release should be considered, as calcium release changes cytosolic composition and should have therefore influence on the cytoskeleton and the shape of the cells. Changes on the cytosolic composition influences the cell itself and have therefore influence on cell-cell contact which is theoretically described by R_b. According to the ECIS model cell shape changes over the entire cell body are detected and changes to impedance are according to the simulations influenced by C_m and R_b, effectively α does not contribute to the signal for the experiments performed in this thesis (Fig. 4-26). Histamine receptor activation leads to Ca^{2+} release out of the endoplasmatic reticulum and is a second messenger and therefore a part of complex cytosolic reactions. Ca^{2+} release kinetics are difficult to measure with slow imaging methods, due to the highly reactive calcium and calcium-dependent chemical pathways within the cells [114]. The release of calcium from endoplasmic reticulum and the reuptake in the same [115] are also to consider in in the received signal pattern. A further point is the Ca^{2+} wave activity induced by IP_3 which is part of the $_hH_1$ signal transduction [116] and the wide scope of Ca^{2+} regulatory mechanism (Ca^{2+} channels, Ca^{2+} pumps, Ca^{2+} exchangers) [50]. The extreme points of the recorded signal patterns indicate for the two readouts major changes within the first five to ten minutes (Fig. 4-40 B, Fig. 4-41 B histamine and calcimycine; Fig. 4-43 B histamine ECIS and SPR). The dual ECIS-SPR sensor offers due to its high resolution and online monitoring a picture (signal pattern) for complex intracellular answers and underlay the necessity of fast signal tracking for GPCR investigations. The dual ECIS-SPR sensor offers by its high time resolution and the online recording of the agonist addition an exact overlay of the recorded signal patterns and therefore exactly comparison of the received signal pattern.

Analyzing the temperature dependent signal pattern of histamine induced response in U-373 MG cells (Fig. 4-44) was carried out to have more information about the influence of membrane fluidity at certain temperatures (4.4.1.3). The experiments were performed separately with SPR and ECIS. The standard temperature for all experiment performed in this thesis was chosen by nearly body temperature of 37 °C. The experiment at 37 °C provided the expected signal pattern for both methods previously shown. The lower temperature of 27 °C was chosen to stay under phase transition temperature just around 30 °C. The signal response for 27 °C shows for SPR a delayed maximum and minimum value. The ECIS

experiment shows a delayed signal dip followed by a constant signal increase without a maximum for the whole recording time. The experiments at 42 °C where chosen to imitate fever in a range of medical emergency (hyperthermia). The SPR signal shows the maximum, minimum and the second maximum earlier compared to standard temperature. Additionally the second maximum has a bigger signal value than the first maximum. ECIS readout shows the minimum and the maximum earlier than the standard experiment, both extreme values have additional smaller intensity. Studies have shown that the activity of neurotransmitters such as sereotonin$_{1A}$ receptor (GPCR) can be inhibited by cholesterol depletion in hippocampal membranes which might also be mediated by changes in membrane fluidity [118, 119]. Investigations on U-373 MG cells indicate that membrane fluidity not only decreases with decreased temperature but also with a decreasing cholesterol content, induced by MβCD (methyl-β-cyclodextrine) [120]. Cholesterol depletion has more effect on intracellular membranes than on plasma membranes [120]. This fact is not further investigated but necessary to mention when looking on intracellular processes. Literature reports also of no evidence for a membrane phase transition over a range of 14-37° C, but report instead of a smooth increase in diffusion coefficient as function of temperature. This effect is overall supporting a further example of how robust biological systems are on environmental changes [121]. The results in this thesis underlay mainly the overall effect for the received signal patterns for impedance and SPR based readout. The results show clearly for lower temperatures (27 °C) a deceleration of the signal pattern while higher temperatures (42 °C) show an accelerated signal pattern compared to the standard experimental temperature (37 °C).

Main objective in this thesis was to show by label-free (impedance and optical based readout) analysis differences in signal patterns on activation of g-protein coupled receptors. For investigations on a second GPCR system, the human dopamine D_2-receptor was chosen (0). According to pharmacological textbooks D_2-receptors are coupled to the G-protein $G_{\alpha i}$ which is known to inhibit the activity of the adenylate cyclase. The adenylate cyclase is an enzyme which converts ATP to cAMP, which acts as second messenger and is involved in further intracellular signal transduction [122, 123]. The D_2 receptor is expressed in CHO (Chinese Hamster Ovary) cells in two isoforms D_2S and D_2L. The D_2L differs from D_2S-receptor by the addition of 29 amino acids in the third intracellular loop in the protein structure [124]. Two agonist where used for investigation of the system, the endogenous ligand dopamine and the synthetic agonist quinpirole. Both receptor isoforms (D_2S and D_2L) display similar affinity for most agonist and antagonists, expressed in HEK 293 cells [125].

The dose response analysis of the CHO cell line with the two isoforms of the D_2 receptor (4.4.2.1) were performed under same conditions for both agonists (dopamine and quinpirole).

The impedance measurement for the dopamine stimulation (Fig. 4-45 ECIS) of D_2S and D_2L are distinguishable. The impedance increase of the D_2L (Fig. 4-45 B) isoform, compared to the D_2S isoform (Fig. 4-45 A), is overall almost two times higher. The signal pattern of the D_2L isoform shows (for concentrations 0.1 µM dopamine and higher) after the first maximum peak a small dip which ends in a second and higher maximum after 15 minutes, while the D_2S isoform describe after reaching first a maximum, a minor signal decrease dip reaching again values of the first maximum. The D_2L isoform reaches the first maximum one minute faster (4 min) compared to the D_2S isoform (5 min.). The EC_{50} values provide different values as the D_2L show a higher affinity to the agonist (dopamine) than the D_2S isoform: EC_{50} = (170 ± 60) nM dopamine for D_2S (short), EC_{50} = (72 ± 20) nM dopamine for D_2L (long). The two isoforms provide for the DMR measurement (Fig. 4-46 DMR) different signal increase but similar signal patterns. D_2S (Fig. 4-46 A) induces a maximum signal increase of 190 pm while D_2L (Fig. 4-46 B) shows a higher signal increase, 295 pm for maximum concentration dopamine (10 µM). The signal maxima are reached at the same time after agonist addition (2 min.) for both receptor isoforms. Both isoforms provide similar EC_{50} values: EC_{50} = (48 ± 11) nM for D_2S (short), EC_{50} = (36 ± 19) nM for D_2L (long). The stimulation of the two isoforms with quinpirole measured by impedance analysis (Fig. 4-47 ECIS) provides similar differences compared to dopamine stimulation (Fig. 4-45). For the highest quinpirole concentrations (3 µM quinpirole) the D_2S isoform (Fig. 4-47 A) show first a maximum followed by a signal dip and reach the values of the first maximum after 15 minutes. The D_2L (Fig. 4-47 B) isoform shows difference in the second maximum which reaches higher values compared to the first maximum (3 µM quinpirole). The maxima occur for D_2L 1.5 minutes (2 min) earlier, compared to the D_2S isoform (3.5 min.). The signal patterns themselves are distinguishable while the calculated EC_{50} values are similar: EC_{50} = (14 ± 5) nM quinpirole D_2S (short), EC_{50} = (24 ± 4) nM for D_2L (long) quinpirole. The DMR measurement of the two isoforms stimulated with quinpirole (Fig. 4-48 DMR) provide minor differences for the recorded signal patterns but higher differences for the calculated EC_{50} values: EC_{50} = (8 ± 2) nM quinpirole D_2S (short), EC_{50} = (66 ± 14) nM quinpirole for D_2L (long). The signal maxima are a bit higher and are reached a little bit faster for D_2L (Fig. 4-48 B) (Δ λ= 180 pm, 1.25 min) compared to the D_2S (Fig. 4-48 A) (Δ λ= 160 pm, 1.50 min) isoform. Overall the impedance based signal reaches the maxima values later compared to the DMR signal for both agonists (dopamine and quinpirole). The ECIS measurement provides more distinguishable signal patterns than DMR measurement for both ligands. The stimulation with the synthetic agonist quinpirole induces faster signal maxima for both isoforms compared to dopamine and on both label-free readouts (ECIS and DMR). The D_2L isoform reaches the signal maxima overall faster compared to the D_2S isoform.

Deconvolution of the signalling cascade was approached by using FSK (forskolin), a pharmacological tool which activates basal the adenylate cyclase directly (4.4.2.2). The D_2 receptors are preferably coupled to the $G_{\alpha i}$ pathway. Upon activation, $G_{\alpha i}$ inhibits adenylate cyclase that is responsible for converting AMP to cAMP, which is a second messenger and involved in a multiple intracellular pathways. However, under resting conditions the intracellular cAMP levels are rather low so that any inhibitory activity is hard to measure. Literature reports of several methods to measure cAMP levels, containing forskolin and forskolin free assay formats [126]. Forskolin is a general activator of all but one adenylyl cyclase isoform namely adenylate cyclase 9, connected to G_s pathway [107, 127, 128]. The FSK concentrations used for cell prestimulation in this thesis where determined by DMR readout, resulting in different concentrations, for the D_2S (2.3 µM FSK) and D_2L (0.5 µM) isoforms (Fig. 4-49). The two D_2 receptor isoforms where compared without (w/o) and with (w) FSK prestimulation, followed by agonist stimulation (dopamine and quinpirole) on their general signal pattern with ECIS and DMR readout.

CHO D_2S cells without and with FSK prestimulation followed by dopamine addition (Fig. 4-50 ECIS) provided signals differing in impedance values and in the signal pattern. The FSK prestimulation induced for the D_2S (Fig. 4-50 B) isoform a massive and steep impedance decrease for 10 minutes and have a stable signal before dopamine addition. The FSK free experiment for the D_2S (Fig. 4-50 A) isoform, show for control addition of L 15 (media control) minor signal changes. After dopamine addition the prestimulated D_2S (Fig. 4-50 B) isoform show massive steep impedance increase for 3 minutes followed by a further signal increase for 10 minutes and a slight signal increase for rest of recording time, for dopamine concentrations 0.3 µM and higher. The FSK free experiment for the D_2S (Fig. 4-50 A) isoform show a signal increase after dopamine addition (0.1 µM and higher) followed by a small signal dip and has after 13 minutes reached the first maximum value (t = 3 min.), stays then at a constant signal value till the end of data recording. The main difference for the impedance based readout for the D_2S isoform is the significant different baseline behaviour induced by FSK and the fourfold signal impedance increase after dopamine addition compared to the FSK free experiment. The DMR signal for dopamine stimulation of the D_2S isoform (Fig. 4-51 DMR), shows small differences for the FSK prestimulated cells compared to the FSK free experiment. The D_2S isoform with FSK prestimulation (Fig. 4-51 B) show a little bit larger baseline drop after FSK addition compared to the FSK free experiment (Fig. 4-51 A) ($\Delta \lambda$ = 5pm). The dopamine induced maxima are reached at identical times (2 min) but FSK prestimulation show 50 pm higher maximum values compared to the FSK free experiment. The differences for FSK prestimulation followed by dopamine stimulation are not significant for the D_2S isoform recorded with DMR.

CHO D_2L cells without and with FSK prestimulation followed by dopamine addition (Fig. 4-52 ECIS) provided signals differing in impedance values and in the signal pattern. The FSK prestimulation induced for the D_2L (Fig. 4-52 B) isoform show a massive and steep impedance decrease for 10 minutes and have a stable signal before dopamine addition. The FSK free experiment for the D_2L (Fig. 4-52 A) isoform shows for addition of L 15 (media control) minor signal changes. After dopamine addition the prestimulated D_2L (Fig. 4-52 B) isoform shows massive steep impedance increase for 3 minutes followed by a further signal increase, with less slope, for 10 minutes and a slight signal increase for rest of recording time, for dopamine concentrations 0.1 µM and higher. The FSK free experiment for the D_2L (Fig. 4-52 A) isoform show a signal increase to a maximum followed by a signal dip and reaches a second and higher maximum value (t =13 min.), stays then at a constant signal value till the end of data recording. The main difference for the impedance based readout for the D_2L isoforms is the different baseline behaviour induced by FSK and a threefold signal impedance increase compared to the FSK free experiment after dopamine addition. The D_2L isoform dopamine experiments (Fig. 4-53 DMR) showed for the comparison of the FSK free and prestimulated cell layer bigger differences for the baseline and signal increase. FSK prestimulation for D_2L isoform (Fig. 4-53 B) induced a two time bigger baseline drop ($\Delta \lambda = 220$) divided in a 5 minutes steep and a 10 minutes small signal drop, compared to the unstimulated experiment of D_2L isoform (Fig. 4-53 A) delivering a continuously signal decrease ($\Delta \lambda = 90$). The signals after dopamine addition reach the maximum values both within 2 minutes but differ massive in their individual maxima (D_2L $\Delta \lambda = 290$ pm (w/o FSK) Fig. 4-53 B, D_2L $\Delta \lambda = 500$ pm (w FSK) Fig. 4-53 A, for max. concentration of 10 µM dopamine). The main differences in the DMR readout are the big kinked baseline drop and the higher maxima values for the FSK prestimulated D_2L isoform compared to the FSK free experiment.

CHO D_2S cells without and with FSK prestimulation followed by quinpirole addition (Fig. 4-54 ECIS) provided signals differing in impedance increase and in the signal pattern. The FSK prestimulation induced a massive and steep impedance decrease for 10 minutes for the D_2S (Fig. 4-54 B) isoform and has a stable signal before dopamine addition. The FSK free experiment for the D_2S (Fig. 4-54 A) isoform shows minor signal changes for addition of L 15 (media control). After dopamine addition the prestimulated D_2S (Fig. 4-54 B) isoform shows massive steep impedance increase for 3 minutes followed by a further signal increase, with smaller slope, for 10 minutes and a slight signal increase for rest of recording time, for quinpirole concentrations 0.01 µM and higher. The FSK free experiment for the D_2S (Fig. 4-54 A) isoform show a signal increase to a maximum followed by a small signal dip and has after 13 minutes reached the first maximum value (t = 3 min.) and stays at a constant signal value till the end of data recording. The main difference for the impedance based readout for the D_2S

isoform is the different baseline behaviour induced by FSK and the fivefold signal impedance increase compared to the FSK free experiment after quinpirole addition.

The DMR signal for quinpirole stimulation of the D_2S isoform (Fig. 4-55 DMR) shows major differences for the FSK prestimulated cells compared to the FSK free experiment. The D_2S isoform with FSK prestimulation (Fig. 4-55 B) show a two time bigger baseline drop divided in a 2.5 minutes steep, 7.5 minutes small signal drop followed by 5 minutes stable signal ($\Delta \lambda$ = 135), compared to the unstimulated experiment (Fig. 4-55 A) which showed a continuously and much smaller baseline decrease ($\Delta \lambda$ = 60). The maximum is reached at identical times (1.25 min) but is two times higher for the FSK prestimulation (Fig. 4-55 A D_2S $\Delta \lambda$ = 160 pm (w/o FSK), Fig. 4-55 B D_2S $\Delta \lambda$ = 300 pm (w FSK) for concentration of 1 µM quinpirole). The maximum signals drop for 10 minutes (w/o and w FSK) and show then small signal drifts till the end of data recording. The FSK prestimulation provided differences for signal intensity and the recorded signal pattern overall for the D_2S isoform compared to the FSK free experiment.

CHO D_2L cells without and with FSK prestimulation followed by quinpirole addition (Fig. 4-56 ECIS) provided signals differing in impedance value and the signal pattern. The FSK prestimulation induced a steep impedance decrease for 10 minutes for the D_2L (Fig. 4-56 B) isoform and a stable signal before quinpirole addition. The FSK free experiment for the D_2L (Fig. 4-56 A) isoform shows minor signal changes for addition of L 15 (media control). After quinpirole addition the prestimulated D_2L (Fig. 4-56 B) isoform show massive steep impedance increase for 3 minutes followed by a further signal increase with smaller slope for 10 minutes followed by a slight signal increase for rest of recording time, for quinpirole concentrations 0.1 µM and higher. The FSK free experiment for the D_2L (Fig. 4-56 A) isoform show a signal increase followed by a signal dip and reaches a second and higher maximum value (t =13 min.), stays then at a constant signal value till the end of data recording. The main difference for the impedance based readout for the D_2L isoforms is the different baseline behaviour induced by FSK and a 2.5 fold impedance increase compared to the FSK free experiment after quinpirole addition.

Quinpirole stimulation of the D_2L isoform (Fig. 4-57 DMR) showed major differences between the FSK free and prestimulated experiments. FSK prestimulation for the D_2L isoform (Fig. 4-57 B) induced a more than four time bigger baseline drop ($\Delta \lambda$ = 270) divided in a 3 minutes steep signal decrease, 2 minutes increase and a 10 minutes slight signal decrease, compared to the unstimulated experiment delivering a continuously signal decrease ($\Delta \lambda$ = 60). The signal increase after quinpirole addition show main difference is in the maxima values (D_2L $\Delta \lambda$ = 180 pm (w/o FSK), D_2L $\Delta \lambda$ = 415 pm (w FSK), for max. concentration of 1 µM quinpirole). The maximum values appear with a time delay (D_2L $\Delta t_{max.}$= 1.25 min (w/o FSK), D_2L $\Delta t_{max.}$ = 2 min (w FSK)). For both isoforms the signals drop for nearly 8 minutes and stay then at a constant

value, but for the FSK prestimulated experiment at concentration dependent values. The main differences in the DMR readout for FSK prestimulation are the big baseline drop and the higher maxima values with concentration dependent final values for the D_2L isoform, compared to the FSK free experiments.

Comparing the EC_{50} values for the two D_2 receptor isoforms (D_2S and D_2L) and the endogenous (dopamine) and synthetic (quinpirole) agonist reveals some tendencies (Table 4-3). Dopamine induces higher EC_{50} values for the D_2S isoform compared to D_2L isoform. The prestimulation with FSK of D_2S show no tendency. The prestimulation with FSK of D_2L show smaller EC_{50} values compared to the FSK free experiments for dopamine. Quinpirole induces smaller EC_{50} values for the D_2S isoform compared to D_2L isoform. The prestimulation with FSK of D_2S show smaller EC_{50} values compared to the FSK free experiments for quinpirole. The prestimulation with FSK of D_2L show higher EC_{50} values compared to the FSK free experiments for quinpirole. The determined EC_{50} values confirm each other for the ECIS and DMR readouts, except for D_2S dopamine with and without FSK.

Table 4-3 EC_{50} values for the D2 receptor isoforms D2S (short) and D2l (long), without (w/o) and with (w) forskolin (FSK) prestimulation. For two agonist, the endogenous ligand dopamine and the synthetic ligand quinpirole (c = nM) have been used in the experiments.

	w/o FSK	D_2S (short)	**w** FSK			**w/o** FSK	D_2L (long)	**w** FSK
Dopamine								
ECIS Fig. 4-50	78 ± 15	**>**	54 ± 6	**>**	ECIS Fig. 4-52	30 ± 2	**>**	14 ± 1
DMR Fig. 4-51	48 ± 11	**<**	92 ± 23		DMR Fig. 4-53	36 ± 19	**>**	27 ± 14
Quinpirole								
ECIS Fig. 4-54	14 ± 5	**>**	1.5 ± 0.1	**<**	ECIS Fig. 4-56	23 ± 4	**<**	33 ± 7
DMR Fig. 4-55	8 ± 2	**>**	2 ± 1.6		DMR Fig. 4-57	66 ± 14	**<**	50 ± 7

The next step was to compare the two CHO D_2 receptor isoforms (D_2S and D_2L) by their ECIS and DMR signal pattern specifically for the endogenous agonist dopamine induced responses of unstimulated and FSK prestimulated celllayer. Quinpirole induced responses are not further discussed. The recorded signals (ECIS and DMR) were put together in one plot. The signals were compared by overlay of the original dataset with their specific values, additionally a normalized dataset was plotted below where the minimum and maximum signals were set to zero (min.) and one (max.), respectively.

The CHO D_2S isoform (Fig. 4-58 A & B, DMR, red curves) shows for the DMR readout no major differences for FSK pre-stimulation of the cells or not. The baseline recording shows a minor difference for the FSK prestimulated celllayer as it appears wavelike compared to the FSK free experiment. The differences in signal drop for baseline recording and for dopamine induced signal maximum are, with respect to the EnSpire multimode reader, insignificant. The ECIS readout (Fig. 4-58 A & B, ECIS, black curves) reveals major differences for the recorded signal pattern and impedance values. The FSK prestimulation induces a steep and massive impedance drop while the unstimulated celllayer shows for L 15 (media control) addition insignificant impedance changes. Dopamine addition induces for both experiments (w/o and w FSK) steep impedance increase but show distinguishable signal patterns with major differences in impedance increase. The FSK free experiment has a significant signal kink for dopamine addition after the maximum peak which disappears with the FSK prestimulation. The D_2S receptor activation (w/o and w FSK) recorded with ECIS provides fingerprint like signal pattern for either receptor while the DMR based signal pattern is indistinguishable. The normalized data plots for the ECIS and DMR (Fig. 4-58, C & D) show how the signal response can be concealed and how signal pattern can appear stretched, in this case mainly for the impedance based recording.

The CHO D_2L isoform (Fig. 4-59 A & B, DMR, red curves), shows for the DMR readout differences for FSK pre-stimulation of the cells or not. The baseline recording shows a difference for the FSK prestimulated cell layer as it drops with a curvature compared to the FSK-free experiment which decreases nearly continuously. The maximum values induced by dopamine are nearly twice as high for FSK prestimulation. The signal drop after the maximum value is smaller for the FSK experiment. The differences in signal drop for baseline recording and for the dopamine induced signal maximum with respect to the EnSpire multimode reader, are distinguishable. The ECIS readout (Fig. 4-59 A & B, ECIS, black curves) offers major differences for the recorded signal pattern and impedance values. The FSK prestimulation induces a steep and massive impedance drop while the unstimulated cell layer shows insignificant impedance changes for L 15 (media control) addition. Dopamine addition induces for both experiments (w/o and w FSK) steep impedance increase but show distinguishable signal patterns. The FSK free experiment has a significant signal kink for dopamine addition after the maximum peak which disappears with the FSK prestimulation. The D_2L receptor activation (w/o and w FSK) recorded with ECIS provide fingerprint like signal pattern for either isoform, also the DMR based signal pattern is distinguishable mainly for the baseline recording. The normalized data plots for ECIS and DMR (Fig. 4-59 C & D) show how the signal response can be concealed and how signal pattern can appear stretched, in this case (D_2L, w/o and w FSK) for both readouts, especially for the DMR signal as the original signal increase after dopamine addition is significant, while ECIS provides fingerprint like patterns

after dopamine addition. Comparing the electrical (ECIS) and the optical readout (DMR) signal pattern, the DMR method shows earlier the maximum values compared to the impedance based readout. In summary the electrical (ECIS) and optical (DMR) based readouts provide complementary signal pattern due to their different physical principles, even when the recorded signal values are collected from different cell layer.

The last readout method comparison was using the separately recorded ECIS and DMR signals and the signals recorded with the dual ECIS-SPR sensor, in this case only for D_2S and D_2L with FSK prestimulation followed by dopamine stimulation. Generally considered, the two data sets are provided by an electrical and optical readout method. In detail considered the two optical readouts record in a range 200 nm above the substrate surface but differ in their specific method (DMR, 1.3.4, SPR 1.3.2). The ECIS-SPR sensor offers the advantage of whole time online recording, which includes the moment of FSK and agonist (dopamine) addition, compared to the used EnSpire multimode reader (3.5). The ECIS values differ due to electrode size, compared to commercially available wells which have influence on the recorded impedance value, but online monitoring is given for both cases. The signals for CHO D_2S cells prestimulated with FSK followed by dopamine addition are collected from different cell layers for ECIS-DMR (Fig. 4-60 A & C) while ECIS-SPR (Fig. 4-60 B & D) recording is collected from the identical cell layer. The impedance based signals (Fig. 4-60 ECIS, black curves) provide similar signal responses. The prestimulation with FSK (2.3 µM) induces steep signal drop for about 5 minutes and gets in a stable position before dopamine addition. The ECIS signal from the dual ECIS-SPR sensor shows a small impedance increase when culture media was removed before dopamine addition. Dopamine addition shows for both ECIS plots a steep impedance increase for 5 minutes followed by a slight signal increase for rest of recording time. The impedance values for the ECIS-SPR sensor are much smaller compared to the commercially ECIS wells because of the bigger electrode size. Overall the recorded signal patters are similar, which is confirmed comparing the normalized datasets (Fig. 4-60 C & D).

The optical signals (Fig. 4-60, DMR A, SPR B) provide differences for the recorded signal pattern. SPR shows for the pre-stimulation with FSK (2.3 µM) a steep signal drop for about 5 minutes. The DMR signal shows a signal shift after the first 5 minutes toward smaller values while the SPR signal shows a nearly stable signal for more than 10 minutes. Differences for the FSK prestimulation and the corresponding baseline were expectable due to the experimental procedure but the DMR signal provides a signal shift while SPR delivers a stable signal before dopamine addition. Dopamine addition induces for DMR and SPR a steep signal increase with similar time till maximum value (DMR: t_{max} = 2 min, $\Delta \lambda$ = 202 pm, SPR t_{max} 2.7 min, Δ R = 231.5 R.U.). The maximum values have similar numbers which are not further

discussed. 10 minutes after dopamine addition DMR signal has dropped to half of the maximum value followed by a further small signal decrease till the end of data recording. The SPR shows from the maximum value a signal decrease reaches a minimum after 8 minutes and shift toward higher values till the end of data recording. The normalized datasets differ in the same manner as the plot size is identical to the original data plot and don't offer new insights.

The signals for CHO D_2L cells pre-stimulated with FSK followed by dopamine addition are collected from different cell layers for ECIS-DMR (Fig. 4-61 A & C) while ECIS-SPR (Fig. 4-61 B & D) recording is collected from identical cell layers. The impedance based signals (Fig. 4-61, black curves) provide similar signal responses. The prestimulation with FSK (0.5 µM) induces steep signal drop for about 5 minutes before the signal gets in a stable position before dopamine addition. The ECIS signal from dual ECI-SPR sensor shows a small impedance increase when culture medium was removed before dopamine addition. Dopamine addition shows for both ECIS plots a steep impedance increase for 5 minutes followed by a second signal increase for further 5 minutes, with smaller slope followed by a slightly signal increase for rest of the recording time. The impedance values for the ECIS-SPR sensor are much smaller compared to the commercially ECIS wells. Overall the recorded signal patters are similar, which is confirmed comparing the normalized datasets (Fig. 4-61 C & D). The optical signals (Fig. 4-61 DMR A, SPR B) provide major differences for the recorded signal responses. The prestimulation with FSK (0.5 µM) induce a signal drop. The DMR signal declines for the first 5 minutes and shift toward smaller values for 10 minutes before dopamine addition. The SPR signals drop massively for 2.5 minutes after FSK addition to a minimum value and increase within the next 7.5 minutes to a stable value, which stay for 5 minutes constant till dopamine addition. Differences for the FSK pre-stimulation and the therefore collected baseline where expectable due to the experimental procedure but the DMR signal differs completely to the SPR signal. The SPR response shows a unique signal pattern after FSK prestimulation. Dopamine addition induces for DMR and SPR a steep signal increase with comparable time till maximum value (DMR: t_{max} = 2.5 min, $\Delta \lambda$ = 484 pm, SPR t_{max1} 2.3 min, Δ R = 318 R.U.) The maximum values are different but not further discussed. The DMR signal drop after the maximum value for 10 minutes and stay at a constant signal value till the end of data recording. The SPR signal show after the first maximum a minor signal dip and reaches a second maximum (SPR t_{max2} = 4.1 min, Δ R = 322 R.U.). The signal drops for 4 minutes to a minimum value and increase wavelike till the end of data recording. The SPR signal differs completely from the DMR response. The normalized datasets differ in the same manner as the plot size is identical to the original data plot and don't offer new insights.

Last part of the results was the comparison of the two D_2 receptor isoforms (D_2S and D_2L) received by the ECIS and DMR readout (Fig. 4-62) and by the dual ECIS-SPR sensor readout (Fig. 4-63). Since Impedance and optical readout report on different physical properties, it is straightforward to compare the different readout experiments for the two isoforms of the D_2 receptor among themselves. It is the major idea of this thesis to find characteristic features in the time course data of either technique or methodical approach to identify characteristic changes that occur in synchrony.

Fig. 4-62 compares the FSK pre-stimulated CHO D_2S (Fig. 4-62 A) and the FSK pre-stimulated CHO D_2L (Fig. 4-62 B) followed by dopamine stimulation results received by ECIS (black curves) and DMR (red curves). The DMR responses (red curves) for CHO D_2S (Fig. 4-62 A) and CHO D_2L (Fig. 4-62 B) have differences in baseline recording and show major differences for maximum values after dopamine addition. The signal decreases after the maximum value shows differences in the declining signal pattern. The ECIS responses (black curves) for CHO D_2S (Fig. 4-62 A) and CHO D_2L (Fig. 4-62 B) differ mainly in the dopamine induced signal increase. FSK induced signal decrease is very similar. The impedance increase shows for CHO D_2S (Fig. 4-62 A) steep impedance increase with one major turning point and afterwards a small value increase. For CHO D_2L (Fig. 4-62 B) two remarkable kinks in impedance increase can be identified. The impedance pattern differs for the two isoforms

Fig. 4-63 compares the FSK prestimulated CHO D_2S (Fig. 4-63 A) and the FSK prestimulated CHO D_2L (Fig. 4-63 B) followed by dopamine stimulation results received by the dual ECIS-SPR sensor, with ECIS (black curves) and SPR (red curves). The SPR shows for the FSK induced signal change completely different signal patterns for CHO D_2S (Fig. 4-63 A) and CHO D_2L (Fig. 4-63 B) results. Every response shows a characteristic signal pattern and differs therefore clearly. Dopamine addition induces for both isoforms signal increase but shows major differences for the signal answer. CHO D_2S (Fig. 4-63 A) has one signal maximum followed by a minimum and a small signal shift toward higher values. CHO D_2L (Fig. 4-63 B) has a wavelike signal with a maximum value followed by a minimum and a second maximum. The two SPR signals provide for each receptor isoform a specific fingerprint like signal pattern. The ECIS responses (black curves) for CHO D_2S (Fig. 4-63 A) and CHO D_2L (Fig. 4-63 B) differ mainly in the dopamine induced signal increase. FSK induced signal decrease is very similar. The impedance increase shows for CHO D_2S (Fig. 4-63 A) a continuous signal with a specific turning point from where the signal increase slightly till the end of data recording. For CHO D_2L (Fig. 4-63 B) two remarkable points in slope change for impedance increase can be identified.

Overall some differences for cell answer of CHO D_2S and D_2L can be identified with ECIS-DMR. The ECIS-SPR sensor offers for both receptor isoforms fingerprint like signal patterns

which differ characteristically for the two isoforms. The dopamine receptor have been divided in D_1 like (D_1R and D_5R) and D_2 like (D_2R, D_3R and D_4R) receptors which stimulate (D_1R like) and inhibit (D_2 like) adenylyl cyclase and thereby regulating intracellular cAMP levels [129]. The two investigated isoforms are generated by alternative splicing [106]. The investigations with the dual ECIS-SPR sensor delivered two distinctive fingerprint like signal pattern for the two isoforms, which are confirmed by literature describing differences of the isoforms in CHO cells [130]. Literature reports of distinct functions for the two isoform for in vivo experiments [131, 132].

Overall considered the ECIS and DMR signals, for D_2S and D_2L (Fig. 4-62) show minor changes 10 minutes after dopamine addition what leads to the conclusion that the main part of the signalling pathway has ended. The received signal patterns by the dual ECIS-SPR sensor provide for FSK and dopamine addition signal value change with a characteristic signal pattern for each isoform. Within the first 5 minutes of recording, after stimulation (FSK and dopamine) the main part of the signal changes is to observe (Fig. 4-62 and Fig. 4-63).

Intracellular changes of cAMP levels can be considered as main part of the changes for ECIS and SPR signals.

Considering the theoretical results for the ECIS simulation signal changes can be related to C_m and R_b (4.2.2.5). The increase of intracellular cAMP through FSK induces an impedance decrease which correlates to a higher C_m and lower R_b value. The receptor activation with dopamine inhibits the adenylyl cyclase and induces an impedance increase which correlates with higher R_b values. The cell is, according to the ECIS model, considered as a capacitor which can change in reality capacitive behaviour and resistance between the cells by different stimuli (FSK and dopamine). The confluent and maturated cell layer has formed the cell-cell contacts already. The impedance change (decrease and increase) should be caused in major by changes occurring within the cytosol and can be mainly related to the theoretical value of C_m and minor R_b, as cAMP increase induces changes to the composition of the cytosol and have therefore influence morphology of the cell.

Both optical readouts show the same tendencies for the recorded signal pattern. SPR recordings show the changes more accurate compared to the DMR readout. Considering the theoretical results for the SPR simulation (4.2.1.5) signal changes can be related mainly to n_{cleft} and n_{cyt} for adherent cells. According to the SPR readout FSK addition causes reflectivity decrease. The signal decrease should be caused by a decrease of the refractive index within the cytosol (n_{cyt}) and indicating a cell volume increase. The receptor activation, with dopamine, causes reflectivity increase which should be caused by an increase of the refractive index within the cytosol (n_{cyt}) indicating cell volume decrease. The assumption of a maturated and

adherent cell layer, with defined d_{cleft}, indicates small influence of n_{cleft} and main influence of n_{cyt}.

The complexity of the signal transduction and cAMP concentration levels and further intracellular signalling is a topic for itself. The need of a high resolution imaging with label-free approaches to GPCR activation is given with the following example. The time frame in which cAMP levels can change is given by neuronal cells stimulated with serotonin where intracellular cAMP levels increase 20 fold after GPCR activation within 20 seconds [133].

The ECIS and DMR signals of the investigated D_2 receptor isoforms provide differences in the recorded signal pattern (Fig. 4-62). The dual ECIS-SPR is capable to provide fingerprint like signal pattern (Fig. 4-63) and therefore an accurate analytical tool for signal overlay and interpretation.

5 Summary

Label-free cell-based assays are an important analytical tool in drug research today. Optical approaches based on evanescent fields (e.g. Surface Plasmon Resonance, SPR; Dynamic Mass Redistribution, DMR) and altering current based impedance analysis (Electric Cell-substrate Impedance Sensing, ECIS) are the most widespread techniques. The aim of this thesis was to develop and establish a dual ECIS-SPR sensor for G-protein coupled receptor signal transduction analysis and to compare the readout with individual ECIS and DMR experiments. For this purpose two cell lines were selected as example, expressing the histamine $_hH_1$ and dopamine D_2 receptor.

The first step in the thesis was the establishment of a reliable assay format for the dual ECIS-SPR sensor. The development of a manual liquid handling procedure enabled reproducible signal patterns for the histamine H_1 receptor stimulation of the model cell line U-373 MG.

Theoretical analysis of SPR and ECIS signals with respect to changes occurring on the subcellular level (cell-surface junctions versus cell-cell junctions) provided a stronger basis for the interpretation of the experimental signals recorded by optical (SPR and DMR) and impedimetric means (ECIS). The simulations led to the conclusion that specific entities of the cell body have more and some have minor individual influence for either of the two analytical readouts (ECIS and SPR). ECIS integrates over the entire cell body and was found to be more sensitive for changes in cell morphology and less sensitive for the distance between lower membrane and substrate for the conditions of this thesis. SPR is mainly sensitive to the area close to substrate surface and reports on changes close to the sensor surface. The results show the complementary of optical and electrochemical approaches and the potential to provide a better understanding about the changes on the subcellular level during GPCR stimulation.

Cell adhesion experiments illustrated this complementary nature of the data of the dual ECIS-SPR sensor. The dual ECIS-SPR sensor offered the exact overlay of the recorded signal patterns of both readouts and those were compared with the well-known changes occurring in the cell layer during cell attachment and spreading. Whereas the interpretation of ECIS time courses is highly dependent on the AC frequency used for the measurement, interpretation of SPR time courses is dependent on the SPR parameter that is used to describe the experiment.

The cell line U-373 MG with the histamine H_1 receptor was used for setting up the experimental procedures and training the system. With the dual ECIS-SPR sensor dose

dependent receptor stimulation was found for the $_hH_1$ receptor expressed by U-373 MG cells when histamine was used as an agonist. Due to the time consuming experiments with the two chamber dual ECIS-SPR sensor, successive agonist addition was applied. Successive agonist addition provided a higher throughput and similar EC_{50} values compared to the single dose dependency experiments. The next step was to use a synthetic agonist for the histamine H_1 receptor. U-373 MG cells were stimulated with UR-KUM 530. Dose dependency was demonstrated revealing a higher potency compared to histamine. The dual ECIS-SPR sensor was not capable to provide different signal pattern for the different agonists (histamine, UR-KUM 530) and readings do not unequivocally support the notion that UR-KUM 530 behaves like a superagonist.

Based on the well-accepted coupling scheme activation of the $_hH_1$ receptor expressed by U-373 MG cells is presumably followed by a massive increase of Ca^{2+} within the cell. The ionophor *Calcimycin* increases artificially the Ca^{2+} concentration in the cytosol without involvement of a receptor and it provides similar signal patterns as histamine activation. This similarity in response profiles supports the role of Ca^{2+} as a second messenger in histamine signalling after $_hH_1$ receptor activation. In addition, the histamine-induced increase in Ca^{2+} levels was artificially blocked in U-373 MG cells by pre-incubation with the intracellular Ca^{2+} chelator BAPTA-AM. The BAPTA-AM pre-treatment provided distinguishable signal patterns after histamine stimulation. The main signal pattern part was blocked compared to the untreated experiments. The results show the influence of Ca^{2+} as second messenger for the signal pattern. These experimental series confirms the assumption that Ca^{2+} is the main second messenger dominating the recorded signal patterns received by a standard U-373 MG $_hH_1$ receptor stimulation.

Label-free monitoring of $_hH_1$ receptor stimulation was furthermore studied at different experimental temperatures. Experiments clearly demonstrated the temperature dependence of receptor-mediated signalling.

Another major subject of this thesis was the stimulation of the D_2 receptor heterologous expressed in two isoforms (D_2S and D_2L subtype) in CHO cells. The D_2 receptor activates the $G_{\alpha i}$ pathway which inhibits the adenylyl cyclase. Forskolin is an adenylyl cyclase activator and was used as pharmaceutical tool to confirm the signalling also by label-free means. The two receptor isoforms were first investigated using standard ECIS and DMR (EnSpire) devices providing distinguishable signal patterns for the isoforms. The investigation of the two isoforms with the dual ECIS-SPR sensor provided an exact comparison of the fingerprint-like time-resolved response profiles. The plot from the dual ECIS-SPR sensor offers precisely repeatable fingerprint like signal patterns. The two optical methods (SPR and DMR) show

similar tendencies but the dual ECIS-SPR sensor is capable of a more precisely recording for the cell answer and provides therefore additional analytical benefits.

The ECIS-SPR sensor offers high time resolution and online monitoring capabilities for both analytical methods from a single cell layer which proved its usefulness in receptor-mediated signal transduction in this thesis. The high time resolution of both readouts allows for precise kinetic analysis immediately after receptor stimulation. The whole signal transduction cascade is covered analytically and offers a precise look on the cell response. This thesis showed that recording of fingerprint-like signal patterns for cells with different GPCR receptor types is possible with the dual ECIS-SPR sensor.

6 Zusammenfassung

Markierungsfreie zellbasierte Assays sind heutzutage ein wichtiges analytisches Instrument in der Arzneimittelforschung. Optische Methoden die auf evaneszenten Feldern basieren (z. B. Oberflächenplasmonresonanz, SPR, dynamische Massenumverteilung, DMR) und Wechseltromwiederstand basierte Impedanzmessung (Electric Cell-Substrate Impedance Sensing, ECIS) sind die am weitesten verbreiteten Techniken. Das Ziel dieser Arbeit war die Entwicklung und Etablierung eines dualen ECIS-SPR Sensors zur Untersuchung von G-Protein-gekoppelter Rezeptor Signaltransduktion und der Vergleich der Messmethode mit individuellen ECIS und DMR Experimenten. Zu diesem Zweck wurden beispielhaft zwei Zelllinien ausgewählt die jeweils den Histamin $_hH_1$ beziehungsweise den Dopamin D_2 Rezeptor exprimieren.

Der erste Schritt der Arbeit bestand in der Etablierung eines zuverlässigen Assay Formats für den dualen ECIS-SPR Sensor. Die Entwicklung einer manuellen Zugabe Methode ergab reproduzierbare Signal Muster für die Histamin H_1 Rezeptor Stimulation der Modellzelllinie U-373 MG.

Die theoretische Analyse von SPR und ECIS Signalen in Bezug auf Änderungen auf subzellulärer Ebene (Zell-Oberflächen Kontaktstellen gegenüber Zell-Zell Kontaktstellen) lieferte eine stärkere Grundlage für die Interpretation der experimentellen Signale, aufgezeichnet mit optischen (SPR und DMR) und impedimetrischen Instrumenten (ECIS). Die Simulationen führten zu dem Schluss dass bestimmte Regionen des Zellkörpers mehr und einige einen geringen individuellen Einfluss auf eine der beiden analytischen Messmethoden (ECIS und SPR) haben. ECIS integriert über den gesamten Zellkörper und zeigte sich sensitiv für Veränderungen der Zellmorphologie und weniger empfindlich für den Abstand zwischen unterer Membran und Substrat für die verwendeten Bedingungen in dieser Arbeit. SPR ist vor allem sensitiv für den Bereich nahe der Substratoberfläche und reagiert auf Veränderungen direkt an der Sensoroberfläche. Die Ergebnisse zeigen die Komplementarität der optischen und elektrochemischen Ansätze und das Potenzial ein besseres Verständnis zu vermitteln für die Änderungen auf subzellulärer Ebene während der GPCR Stimulation.

Zell Adhäsion Experimente veranschaulichten die komplementäre Natur der Daten des dualen ECIS-SPR Sensors. Der duale ECIS-SPR Sensor ermöglichte die exakte Überlagerung der aufgezeichneten Signalmuster für beide Messmethoden, diese wurden verglichen mit den bekannten Veränderungen der Zellschicht während der Zell Bindung und Spreitung. Während die Interpretation der ECIS Zeitverläufe stark von der verwendeten Wechselstromfrequenz für

die Messung abhängt ist die Interpretation der SPR Zeitverläufe von den SPR Parametern abhängig die zur Wiedergabe des Experiments verwendet wurden.

Die Zelllinie U-373 MG mit dem Histamin H_1 Rezeptor wurde zum Einstellen des experimentellen Verfahrens und zum Training des Systems verwendet. Mit dem dualen ECIS-SPR Sensor konnte eine Dosis-Wirkungsbeziehung gezeigt werden für den $_hH_1$ Rezeptor exprimiert von U-373 MG Zellen mit Histamin als Agonist. Aufgrund der zeitaufwendigen Experimente für den dualen ECIS-SPR Sensor mit einem zwei Messkammer System wurde eine sukzessive Agonisten Zugabe angewendet. Sukzessive Zugabe des Agonisten ergab einen höheren Durchsatz und ähnliche EC_{50} Werte im Vergleich zu den Dosis Abhängigen einzel Zugabe Experimenten. Der nächste Schritt war die Verwendung eines synthetischen Agonisten für den Histamin H_1 Rezeptor. U-373 MG Zellen wurden mit UR-KUM 530 stimuliert. Es wurde eine Dosis Wirkungsbeziehung gezeigt die eine höhere Wirksamkeit zeigte im Vergleich zu Histamin. Der duale ECIS-SPR Sensor war nicht geeignet unterschiedliche Signalmuster für die verschiedenen Agonisten (Histamin, UR-KUM 530) zu liefern und die Messwerte unterstützen nicht eindeutig die Auffassung dass sich UR-KUM 530 wie ein Superagonist verhält.

Basierend auf dem allgemein akzeptierten Kopplungsschema für die Aktivierung des $_hH_1$ Rezeptors exprimiert in U-373 MG Zellen folgt wahrscheinlich ein massiver Anstieg der Ca^{2+} konzentration innerhalb der Zelle. Der Ionophor *Calcimycin* erhöht künstlich die Ca^{2+} konzentration im Cytosol ohne Beteiligung eines Rezeptors und liefert ähnliche Signalmuster wie durch Histamin Aktivierung. Die Ähnlichkeit in den Antwortprofilen unterstützt die Rolle von Ca^{2+} als sekundärem Botenstoff bei der Histamin Signalweiterleitung nach $_hH_1$ Rezeptor Aktivierung. Zusätzlich wurde der Histamin induzierte Anstieg des Ca^{2+} Spiegels in U-373 MG Zellen durch Vorinkubation mit dem intrazellulären Ca^{2+} Chelator BAPTA-AM künstlich blockiert. Die BAPTA-AM Vorbehandlung ergab nach Histamin Stimulation unterscheidbare Signalmuster. Der Hauptteil des Signals war im Vergleich zu den unbehandelten Experimenten blockiert. Die Ergebnisse zeigen den Einfluss von Ca^{2+} als sekundärer Botenstoff auf das Signalmuster. Diese Versuchsreihen bestätigen die Annahme dass Ca^{2+} der wichtigste sekundäre Botenstoff ist, welcher die aufgezeichneten Signalmuster dominiert, die bei einer Standard U-373 MG $_hH_1$ Rezeptorstimulation aufgezeichnet werden.

Das markierungsfreie Messen der $_hH_1$ Rezeptor Stimulation wurde ferner bei unterschiedlichen Temperaturen experimentell untersucht. Die Experimente zeigten deutlich die Temperaturabhängigkeit der Rezeptor vermittelten Signalübertragung.

Ein weiteres zentrales Thema dieser Arbeit war die Stimulierung des D_2 Rezeptors welcher heterolog exprimiert wird als zwei Isoformen (D_2S und D_2L Subtyp) in CHO Zellen. Der D_2

Rezeptor aktiviert den $G_{\alpha i}$ Signalweg welcher die Adenylylcyclase hemmt. Forskolin ist ein Adenylylcyclase Aktivator und wurde als pharmazeutisches Werkzeug verwendet um die Signalübertragung mit markierungsfreien Methoden zu bestätigen. Die beiden Rezeptor Isoformen wurden zunächst mit Standard ECIS und DMR (EnSpire) Geräten untersucht welche unterscheidbare Signalmuster für die beiden Isoformen ergaben. Die Untersuchung der beiden Isoformen mit dem dualen ECIS-SPR Sensor bietet einen exakten Vergleich der fingerabdruckähnlichen zeitaufgelösten Antwortprofile. Das Diagramm des dualen ECIS-SPR Sensors bietet präzise reproduzierbare Fingerabdruck ähnliche Signalmuster. Die beiden optischen Methoden (SPR und DMR) zeigen ähnliche Tendenzen aber der duale ECIS-SPR Sensor kann die Zellantwort präziser aufzeichnen und bietet daher zusätzliche analytische Vorteile.

Der ECIS-SPR Sensor bietet eine hohe Zeitauflösung und online Messung für beide Analysemethoden aus einer einzelnen Zellschicht was sich in dieser Arbeit als nützlich für die rezeptorvermittelte Signalübertragung erwiesen hat. Die hohe zeitliche Auflösung für beide Messmethoden ermöglicht eine präzise kinetische Analyse unmittelbar nach der Rezeptorstimulation. Die gesamte signalweiterleitungs Kaskade wird analytisch erfasst und bietet einen präzisen Blick auf die Zellantwort. Diese Arbeit zeigte dass mit dem dualen ECIS-SPR Sensor die Aufnahme fingerabdruckartiger Signalmuster für Zellen mit unterschiedlichen GPCR Rezeptortypen möglich ist.

7 References

1. Lodish, H., *Molecular Cell Biology.* 2000. **4**.
2. Bockaert, J. and J.P. Pin, *Molecular tinkering of G protein-coupled receptors: an evolutionary success.* Embo Journal, 1999. **18**(7): p. 1723-1729.
3. Overington, J.P., B. Al-Lazikani, and A.L. Hopkins, *How many drug targets are there?* Nature Reviews Drug Discovery, 2006. **5**: p. 993.
4. Pierce, K.L., R.T. Premont, and R.J. Lefkowitz, *Seven-transmembrane receptors.* Nature Reviews Molecular Cell Biology, 2002. **3**: p. 639.
5. Gether, U. and B.K. Kobilka, *G protein-coupled receptors. II. Mechanism of agonist activation.* J Biol Chem, 1998. **273**(29): p. 17979-82.
6. Lundstrom, K., *Present and future approaches to screening of G-protein-coupled receptors.* Future Med Chem, 2013. **5**(5): p. 523-38.
7. Fredriksson, R. and H.B. Schiöth, *The Repertoire of G-Protein–Coupled Receptors in Fully Sequenced Genomes.* Molecular Pharmacology, 2005. **67**(5): p. 1414-1425.
8. Schlyer, S. and R. Horuk, *I want a new drug: G-protein-coupled receptors in drug development.* Drug Discovery Today, 2006. **11**(11): p. 481-493.
9. Oldham, W.M. and H.E. Hamm, *Heterotrimeric G protein activation by G-protein-coupled receptors.* Nature Reviews Molecular Cell Biology, 2008. **9**: p. 60.
10. Sprang, S.R., *Activation of G Proteins by GTP and the Mechanism of Ga-Catalyzed GTP Hydrolysis.* Biopolymers, 2016. **105**(8): p. 449-462.
11. Gilchrist, A., *A perspective on more effective GPCR-targeted drug discovery efforts.* Expert Opinion on Drug Discovery, 2008. **3**(4): p. 375-389.
12. Gilman, A.G., *G proteins : transducers of receptor-generated signals.* 1987.
13. Cabrera-Vera, T.M., et al., *Insights into G Protein Structure, Function, and Regulation.* Endocrine Reviews, 2003. **24**(6): p. 765-781.
14. Hamm, H.E., *The Many Faces of G Protein Signaling.* Journal of Biological Chemistry, 1998. **273**(2): p. 669-672.
15. Hendriks-Balk, M.C., et al., *Regulation of G protein-coupled receptor signalling: Focus on the cardiovascular system and regulator of G protein signalling proteins.* European Journal of Pharmacology, 2008. **585**(2): p. 278-291.
16. Luttrell, L.M., *Reviews in Molecular Biology and Biotechnology: Transmembrane Signaling by G Protein-Coupled Receptors.* Molecular Biotechnology, 2008. **39**(3): p. 239-264.
17. Milligan, G. and E. Kostenis, *Heterotrimeric G-proteins: a short history.* British Journal of Pharmacology, 2006. **147**(S1): p. S46-S55.
18. Bokoch, G.M., et al., *Purification and properties of the inhibitory guanine nucleotide-binding regulatory component of adenylate cyclase.* Journal of Biological Chemistry, 1984. **259**(6): p. 3560-7.
19. Ross, E.M. and A.G. Gilman, *Biochemical-Properties of Hormone-Sensitive Adenylate-Cyclase.* Annual Review of Biochemistry, 1980. **49**: p. 553-564.
20. Sternweis, P.C., et al., *The regulatory component of adenylate cyclase. Purification and properties.* Journal of Biological Chemistry, 1981. **256**(22): p. 11517-11526.
21. Woehler, A. and E.G. Ponimaskin, *G Protein - Mediated Signaling: Same Receptor, Multiple Effectors.* Current Molecular Pharmacology, 2009. **2**(3): p. 237-248.
22. Gloerich, M. and J.L. Bos, *Epac: Defining a New Mechanism for cAMP Action.* Annual Review of Pharmacology and Toxicology, 2010. **50**(1): p. 355-375.
23. Kamato, D., et al., *Structure, Function, Pharmacology, and Therapeutic Potential of the G Protein, Gα(/q,11).* Frontiers in Cardiovascular Medicine, 2015. **2**: p. 14.
24. Kelly, P., P.J. Casey, and T.E. Meigs, *Biologic Functions of the G12 Subfamily of Heterotrimeric G Proteins: Growth, Migration, and Metastasis.* Biochemistry, 2007. **46**(23): p. 6677-6687.
25. Riobo, N.A. and D.R. Manning, *Receptors coupled to heterotrimeric G proteins of the G12 family.* Trends in Pharmacological Sciences, 2005. **26**(3): p. 146-154.

26. Radhika, V. and N. Dhanasekaran, *Transforming G proteins.* Oncogene, 2001. **20**: p. 1607.
27. Schwindinger, W.F. and J.D. Robishaw, *Heterotrimeric G-protein βγ-dimers in growth and differentiation.* Oncogene, 2001. **20**: p. 1653.
28. Desai, A.N., et al., *Involvement of G Protein-Coupled Receptor Kinase (GRK) 3 and GRK2 in Down-Regulation of the α_{2B}-Adrenoceptor.* Journal of Pharmacology and Experimental Therapeutics, 2006. **317**(3): p. 1027-1035.
29. Drake, M.T., S.K. Shenoy, and R.J. Lefkowitz, *Trafficking of G Protein–Coupled Receptors.* Circulation Research, 2006. **99**(6): p. 570-582.
30. Kostenis, E., M. Waelbroeck, and G. Milligan, *Techniques: Promiscuous Gα proteins in basic research and drug discovery.* Trends in Pharmacological Sciences, 2005. **26**(11): p. 595-602.
31. Hermans, E., *Biochemical and pharmacological control of the multiplicity of coupling at G-protein-coupled receptors.* Pharmacology & Therapeutics, 2003. **99**(1): p. 25-44.
32. Hill, S.J., *G-protein-coupled receptors: past, present and future.* British Journal of Pharmacology, 2006. **147**(S1): p. S27-S37.
33. Heng, B.C., D. Aubel, and M. Fussenegger, *An overview of the diverse roles of G-protein coupled receptors (GPCRs) in the pathophysiology of various human diseases.* Biotechnology Advances, 2013. **31**(8): p. 1676-1694.
34. Thompson, M.D., W.M. Burnham, and D.E.C. Cole, *The G protein-coupled receptors: Pharmacogenetics and Disease.* Critical Reviews in Clinical Laboratory Sciences, 2005. **42**(4): p. 311-389.
35. Luttrell, L.M. and R.J. Lefkowitz, *The role of β-arrestins in the termination and transduction of G-protein-coupled receptor signals.* Journal of Cell Science, 2002. **115**(3): p. 455-465.
36. Rozenfeld, R. and Lakshmi A. Devi, *Exploring a role for heteromerization in GPCR signalling specificity.* Biochemical Journal, 2011. **433**(1): p. 11-18.
37. Lefkowitz, R.J., *Seven transmembrane receptors: something old, something new.* Acta Physiologica, 2007. **190**(1): p. 9-19.
38. Park, J.Y., et al., *Structural mechanism of GPCR-arrestin interaction: recent breakthroughs.* Archives of Pharmacal Research, 2016. **39**(3): p. 293-301.
39. Stephen, S.G.F., et al., *Role of β-Arrestin in Mediating Agonist-Promoted G Protein-Coupled Receptor Internalization.* Science, 1996. **271**(5247): p. 363-366.
40. Prazeres, D.M.F. and S.A.M. Martins, *G protein-Coupled Receptors: An Overview of Signaling Mechanisms and Screening Assays*, in *G Protein-Coupled Receptor Screening Assays: Methods and Protocols*, D.M.F. Prazeres and S.A.M. Martins, Editors. 2015, Springer New York: New York, NY. p. 3-19.
41. Luttrell, L.M., et al., *β-Arrestin-Dependent Formation of β₂ Adrenergic Receptor-Src Protein Kinase Complexes.* Science, 1999. **283**(5402): p. 655-661.
42. Wise, A., S.C. Jupe, and S. Rees, *The Identification of Ligands at Orphan G-Protein Coupled Receptors.* Annual Review of Pharmacology and Toxicology, 2004. **44**(1): p. 43-66.
43. Drews, J., *Drug Discovery: A Historical Perspective.* Science, 2000. **287**(5460): p. 1960-1964.
44. Grundmann, M. and E. Kostenis, *Label-Free Biosensor Assays in GPCR Screening*, in *G Protein-Coupled Receptor Screening Assays: Methods and Protocols*, D.M.F. Prazeres and S.A.M. Martins, Editors. 2015, Springer New York: New York, NY. p. 199-213.
45. Lefkowitz, R.J., J. Roth, and I. Pastan, *Radioreceptor Assay of Adrenocorticotropic Hormone: New Approach to Assay of Polypeptide Hormones in Plasma.* Science, 1970. **170**(3958): p. 633-635.
46. Bylund, *Radioligand binding methods: practical guide and tips.* American Journal of Physiology-Lung Cellular and Molecular Physiology, 1993. **265**(5): p. L421-L429.
47. Hulme, E.C. and M.A. Trevethick, *Ligand binding assays at equilibrium: validation and interpretation.* British Journal of Pharmacology, 2010. **161**(6): p. 1219-1237.

48. Thomsen, W., J. Frazer, and D. Unett, *Functional assays for screening GPCR targets.* Current Opinion in Biotechnology, 2005. **16**(6): p. 655-665.
49. Bootman, M.D., et al., *Ca2+-Sensitive Fluorescent Dyes and Intracellular Ca2+ Imaging.* Cold Spring Harbor Protocols, 2013. **2013**(2): p. pdb.top066050.
50. Takashi A, C.P., Lechleiter JD, Herman B, *Measurement of Intracellular Calcium.* Physiological Reviews, 1999. **79**(4): p. 1089-1125.
51. Emkey, R. and N.B. Rankl, *Screening G Protein-Coupled Receptors: Measurement of Intracellular Calcium Using the Fluorometric Imaging Plate Reader*, in *High Throughput Screening: Methods and Protocols, Second Edition*, W.P. Janzen and P. Bernasconi, Editors. 2009, Humana Press: Totowa, NJ. p. 145-158.
52. Zhang, R. and X. Xie, *Tools for GPCR drug discovery.* Acta Pharmacologica Sinica, 2012. **33**: p. 372.
53. Banica, F.-G., *Chemical Sensors and Biosensors: Fundamentals and Applications (Google eBook).* John Wiley & Sons, 2012.
54. Fang, Y., *Label-free receptor assays.* Drug Discovery Today: Technologies, 2010. **7**(1): p. e5-e11.
55. Fang, Y., A.G. Frutos, and R. Verklereen, *Label-Free Cell-Based Assays for GPCR Screening.* Combinatorial Chemistry & High Throughput Screening, 2008. **11**(5): p. 357-369.
56. Fang, Y., *Label-Free Cell-Based Assays with Optical Biosensors in Drug Discovery.* ASSAY and Drug Development Technologies, 2006. **4**(5): p. 583-595.
57. Opp, D., et al., *Use of electric cell–substrate impedance sensing to assess in vitro cytotoxicity.* Biosensors and Bioelectronics, 2009. **24**(8): p. 2625-2629.
58. Wang, L., et al., *An automatic and quantitative on-chip cell migration assay using self-assembled monolayers combined with real-time cellular impedance sensing.* Lab on a Chip, 2008. **8**(6): p. 872-878.
59. Wegener, J., C.R. Keese, and I. Giaever, *Electric Cell–Substrate Impedance Sensing (ECIS) as a Noninvasive Means to Monitor the Kinetics of Cell Spreading to Artificial Surfaces.* Experimental Cell Research, 2000. **259**(1): p. 158-166.
60. Rocheville, M. and J.C. Jerman, *7TM pharmacology measured by label-free: a holistic approach to cell signalling.* Current Opinion in Pharmacology, 2009. **9**(5): p. 643-649.
61. Scott, C.W. and M.F. Peters, *Label-free whole-cell assays: expanding the scope of GPCR screening.* Drug Discovery Today, 2010. **15**(17): p. 704-716.
62. Peters, M.F., et al., *Comparing Label-Free Biosensors for Pharmacological Screening With Cell-Based Functional Assays.* ASSAY and Drug Development Technologies, 2010. **8**(2): p. 219-227.
63. Giaever, I. and C.R. Keese, *Monitoring fibroblast behavior in tissue culture with an applied electric field.* Proceedings of the National Academy of Sciences, 1984. **81**(12): p. 3761-3764.
64. Giaever, I. and C.R. Keese, *A morphological biosensor for mammalian cells.* Nature, 1993. **366**: p. 591+.
65. Stolwijk, J.A., *Electric manipulation and impedance analysis of adherent cells on gold-film electrodes*. 2011.
66. Giaever, I. and C.R. Keese, *Micromotion of mammalian cells measured electrically.* Proceedings of the National Academy of Sciences, 1991. **88**(17): p. 7896-7900.
67. Keese, C.R., et al., *Electrical wound-healing assay for cells in vitro.* Proceedings of the National Academy of Sciences of the United States of America, 2004. **101**(6): p. 1554-1559.
68. Tiruppathi, C., et al., *Electrical method for detection of endothelial cell shape change in real time: assessment of endothelial barrier function.* Proceedings of the National Academy of Sciences, 1992. **89**(17): p. 7919-7923.
69. Xiao, C. and J.H.T. Luong, *On-Line Monitoring of Cell Growth and Cytotoxicity Using Electric Cell-Substrate Impedance Sensing (ECIS).* Biotechnology Progress, 2003. **19**(3): p. 1000-1005.
70. Hug, T.S., *Biophysical Methods for Monitoring Cell-Substrate Interactions in Drug Discovery.* ASSAY and Drug Development Technologies, 2003. **1**(3): p. 479-488.

71. Schasfoort, R.B.M., *Handbook of Surface Plasmon Resonance: 2nd Edition*. 2017: Royal Society of Chemistry.
72. Otto, A., *Excitation of nonradiative surface plasma waves in silver by the method of frustrated total reflection.* Zeitschrift für Physik A Hadrons and nuclei, 1968. **216**(4): p. 398-410.
73. Kretschmann, E. and H. Raether, *Notizen: Radiative Decay of Non Radiative Surface Plasmons Excited by Light*, in *Zeitschrift für Naturforschung A*. 1968. p. 2135.
74. Robelek, R., *Surface plasmon resonance sensors in cell biology: basics and application.* Bioanalytical Reviews, 2009. **1**(1): p. 57.
75. Homola, J., *Surface Plasmon Resonance Sensors for Detection of Chemical and Biological Species.* Chemical Reviews, 2008. **108**(2): p. 462-493.
76. Piliarik, M., et al., *Compact and low-cost biosensor based on novel approach to spectroscopy of surface plasmons.* Biosensors and Bioelectronics, 2009. **24**(12): p. 3430-3435.
77. Olaru, A., et al., *Surface Plasmon Resonance (SPR) Biosensors in Pharmaceutical Analysis.* Critical Reviews in Analytical Chemistry, 2015. **45**(2): p. 97-105.
78. Michaelis, S., J. Wegener, and R. Robelek, *Label-free monitoring of cell-based assays: Combining impedance analysis with SPR for multiparametric cell profiling.* Biosensors and Bioelectronics, 2013. **49**: p. 63-70.
79. Wang, S.S., et al., *Guided-mode resonances in planar dielectric-layer diffraction gratings.* Journal of the Optical Society of America A, 1990. **7**(8): p. 1470-1474.
80. Fang, Y., et al., *Resonant Waveguide Grating Biosensor for Living Cell Sensing.* Biophysical Journal, 2006. **91**(5): p. 1925-1940.
81. Lee, P.H., et al., *Evaluation of Dynamic Mass Redistribution Technology for Pharmacological Studies of Recombinant and Endogenously Expressed G Protein-Coupled Receptors.* ASSAY and Drug Development Technologies, 2008. **6**(1): p. 83-94.
82. Fang, Y., *The development of label-free cellular assays for drug discovery.* Expert Opinion on Drug Discovery, 2011. **6**(12): p. 1285-1298.
83. Yanase, Y., et al., *Surface Plasmon Resonance for Cell-Based Clinical Diagnosis.* Sensors, 2014. **14**(3): p. 4948.
84. Steyer, J.A. and W. Almers, *A real-time view of life within 100 nm of the plasma membrane.* Nature Reviews Molecular Cell Biology, 2001. **2**: p. 268.
85. Straßer, A., et al., *Molecular Basis for the Selective Interaction of Synthetic Agonists with the Human Histamine H₁-Receptor Compared with the Guinea Pig H₁-Receptor.* Molecular Pharmacology, 2009. **75**(3): p. 454-465.
86. Chabot, V., et al., *Biosensing based on surface plasmon resonance and living cells.* Biosensors and Bioelectronics, 2009. **24**(6): p. 1667-1673.
87. Homola, J., *Present and future of surface plasmon resonance biosensors.* Analytical and Bioanalytical Chemistry, 2003. **377**(3): p. 528-539.
88. Tudos, A.J. and R.B.M. Schasfoort, *Chapter 1 Introduction to Surface Plasmon Resonance*, in *Handbook of Surface Plasmon Resonance*. 2008, The Royal Society of Chemistry. p. 1-14.
89. Viitala, T., et al., *Elucidating the Signal Responses of Multi-Parametric Surface Plasmon Resonance Living Cell Sensing: A Comparison between Optical Modeling and Drug–MDCKII Cell Interaction Measurements.* PLOS ONE, 2013. **8**(8): p. e72192.
90. Chen, K., H. Obinata, and T. Izumi, *Detection of G protein-coupled receptor-mediated cellular response involved in cytoskeletal rearrangement using surface plasmon resonance.* Biosens Bioelectron, 2010. **25**(7): p. 1675-80.
91. Kemper, B., et al., *Integral refractive index determination of living suspension cells by multifocus digital holographic phase contrast microscopy.* Journal of Biomedical Optics, 2007. **12**(5): p. 1-5, 5.
92. Wegener, J., A. Hakvoort, and H.-J. Galla, *Barrier function of porcine choroid plexus epithelial cells is modulated by cAMP-dependent pathways in vitro.* Brain Research, 2000. **853**(1): p. 115-124.

93. Beuthan, J., et al., *The spatial variation of the refractive index in biological cells.* Phys Med Biol, 1996. **41**(3): p. 369-82.
94. Lai, J., et al., *Experimental measurement of the refractive index of biological tissues by total internal reflection.* Applied Optics, 2005. **44**(10): p. 1845-1849.
95. Lanni, F., A.S. Waggoner, and D.L. Taylor, *Structural organization of interphase 3T3 fibroblasts studied by total internal reflection fluorescence microscopy.* The Journal of Cell Biology, 1985. **100**(4): p. 1091-1102.
96. Bereiter-Hahn, J., C.H. Fox, and B. Thorell, *Quantitative reflection contrast microscopy of living cells.* The Journal of Cell Biology, 1979. **82**(3): p. 767-779.
97. Bolin, F.P., et al., *Refractive index of some mammalian tissues using a fiber optic cladding method.* Applied Optics, 1989. **28**(12): p. 2297-2303.
98. Curl, C.L., et al., *Refractive index measurement in viable cells using quantitative phase-amplitude microscopy and confocal microscopy.* Cytometry Part A, 2005. **65A**(1): p. 88-92.
99. Rappaz, B., et al., *Measurement of the integral refractive index and dynamic cell morphometry of living cells with digital holographic microscopy.* Optics Express, 2005. **13**(23): p. 9361-9373.
100. Robelek, R. and J. Wegener, *Label-free and time-resolved measurements of cell volume changes by surface plasmon resonance (SPR) spectroscopy.* Biosensors and Bioelectronics, 2010. **25**(5): p. 1221-1224.
101. Liu, P.Y., et al., *Cell refractive index for cell biology and disease diagnosis: past, present and future.* Lab on a Chip, 2016. **16**(4): p. 634-644.
102. Albers W.M., V.-L.I., *Surface Plasmon Resonance on Nanoscale Organic Films.* Carrara S. (eds) Nano-Bio-Sensing. Springer, New York, NY, 2011.
103. Lo, C.M., C.R. Keese, and I. Giaever, *Impedance analysis of MDCK cells measured by electric cell-substrate impedance sensing.* Biophysical Journal, 1995. **69**(6): p. 2800-2807.
104. Wegener, J., *Impedance Analysis of Cell Junctions*, in *Nanotechnology*. 2010. p. 325-357.
105. Stolwijk, J.A., et al., *Increasing the throughput of label-free cell assays to study the activation of G-protein-coupled receptors by using a serial agonist exposure protocol.* Integr Biol (Camb), 2019.
106. Picetti, R., et al., *Dopamine D2 Receptors in Signal Transduction and Behavior.* 1997. **11**(2-3): p. 121-142.
107. Alasbahi, R.H. and M.F. Melzig, *Forskolin and derivatives as tools for studying the role of cAMP.* Die Pharmazie - An International Journal of Pharmaceutical Sciences, 2012. **67**(1): p. 5-13.
108. Lieb, S., et al., *Label-free analysis of GPCR-stimulation: The critical impact of cell adhesion.* Pharmacological Research, 2016. **108**: p. 65-74.
109. Lieb, S., et al., *Label-free versus conventional cellular assays: Functional investigations on the human histamine H1 receptor.* Pharmacological Research, 2016. **114**: p. 13-26.
110. Mellor, H. and P.J. Parker, *The extended protein kinase C superfamily.* Biochemical Journal, 1998. **332**(2): p. 281-292.
111. Liu, C., et al., *Real-time monitoring biomarker expression of carcinoma cells by surface plasmon resonance biosensors.* Chemical Communications, 2012. **48**(84): p. 10389-10391.
112. Delfino, G., et al., *In vitro ultraviolet A irradiation decreases both release ability and gene-expression of vascular endothelial growth factor-A from mast cells.* Photodermatology, Photoimmunology & Photomedicine, 2012. **28**(3): p. 165-168.
113. Li, X., et al., *Plasmonic nanohole array biosensor for label-free and real-time analysis of live cell secretion.* Lab on a Chip, 2017. **17**(13): p. 2208-2217.
114. Beier, H.T., et al., *Resolving the spatial kinetics of electric pulse-induced ion release.* Biochemical and Biophysical Research Communications, 2012. **423**(4): p. 863-866.
115. Melzer, W., E. Rios, and M.F. Schneider, *Time course of calcium release and removal in skeletal muscle fibers.* Biophysical Journal, 1984. **45**(3): p. 637-641.

116. Camacho, P. and J.D. Lechleiter, *Increased frequency of calcium waves in Xenopus laevis oocytes that express a calcium-ATPase.* Science, 1993. **260**(5105): p. 226.
117. Stricker, S.A., et al., *Confocal microscopy of fertilization-induced calcium dynamics in sea urchin eggs.* Developmental Biology, 1992. **149**(2): p. 370-380.
118. Pucadyil, T.J. and A. Chattopadhyay, *Cholesterol modulates ligand binding and G-protein coupling to serotonin1A receptors from bovine hippocampus.* Biochimica et Biophysica Acta (BBA) - Biomembranes, 2004. **1663**(1): p. 188-200.
119. Pucadyil, T.J. and A. Chattopadhyay, *Cholesterol modulates the antagonist-binding function of hippocampal serotonin1A receptors.* Biochimica et Biophysica Acta (BBA) - Biomembranes, 2005. **1714**(1): p. 35-42.
120. Weber, P., M. Wagner, and H. Schneckenburger, *Microfluorometry of cell membrane dynamics.* Cytometry Part A, 2006. **69A**(3): p. 185-188.
121. Lee, I.-H., et al., *Live Cell Plasma Membranes Do Not Exhibit a Miscibility Phase Transition over a Wide Range of Temperatures.* The Journal of Physical Chemistry B, 2015. **119**(12): p. 4450-4459.
122. Kebabian, J.W. and D.B. Calne, *Multiple receptors for dopamine.* Nature, 1979. **277**(5692): p. 93-96.
123. Stoof, J.C. and J.W. Kebabian, *Opposing roles for D-1 and D-2 dopamine receptors in efflux of cyclic AMP from rat neostriatum.* Nature, 1981. **294**(5839): p. 366-368.
124. Dal Toso, R., et al., *The dopamine D2 receptor: two molecular forms generated by alternative splicing.* The EMBO Journal, 1989. **8**(13): p. 4025-4034.
125. Leysen, J.E., et al., *Comparison of in vitro binding properties of a series of dopamine antagonists and agonists for cloned human dopamine D2S and D2L receptors and for D2 receptors in rat striatal and mesolimbic tissues, using [125I] 2'-iodospiperone.* Psychopharmacology, 1993. **110**(1): p. 27-36.
126. Gilissen, J., et al., *Forskolin-free cAMP assay for Gi-coupled receptors.* Biochemical Pharmacology, 2015. **98**(3): p. 381-391.
127. Dahle, M.K., et al., *Effects of Forskolin on Kupffer Cell Production of Interleukin-10 and Tumor Necrosis Factor Alpha Differ from Those of Endogenous Adenylyl Cyclase Activators: Possible Role for Adenylyl Cyclase 9.* Infection and Immunity, 2005. **73**(11): p. 7290.
128. Hacker, B.M., et al., *Cloning, Chromosomal Mapping, and Regulatory Properties of the Human Type 9 Adenylyl Cyclase (ADCY9).* Genomics, 1998. **50**(1): p. 97-104.
129. Jackson, D.M. and A. Westlind-Danielsson, *Dopamine receptors: molecular biology, biochemistry and behavioural aspects.* Pharmacol Ther, 1994. **64**(2): p. 291-370.
130. Zhang, L.J., J.E. Lachowicz, and D.R. Sibley, *The D2S and D2L dopamine receptor isoforms are differentially regulated in Chinese hamster ovary cells.* Molecular Pharmacology, 1994. **45**(5): p. 878.
131. Usiello, A., et al., *Distinct functions of the two isoforms of dopamine D2 receptors.* Nature, 2000. **408**(6809): p. 199-203.
132. Radl, D., et al., *Differential regulation of striatal motor behavior and related cellular responses by dopamine D2L and D2S isoforms.* Proceedings of the National Academy of Sciences, 2018. **115**(1): p. 198.
133. Bacskai, B.J., et al., *Spatially resolved dynamics of cAMP and protein kinase A subunits in Aplysia sensory neurons.* Science, 1993. **260**(5105): p. 222.

8 Acknowledgments

I thank my supervisor Prof. Dr. Joachim Wegener for issuing this thesis, for any support during the work and for the excellent working conditions in his group.

Moreover, I thank the board of examinars for their thesis reports and the oral examination as well as the chairman of the committee for leading the doctoral exam.

I thank Dr. Judith Stolwijk fort the support during the last years and the provided data.

I thank Dr. Stefanie Michaelis fort the support on different topics.

I thank Barbara Goricnik for the support in the laboratory.

Finally, thank you Sensei.

HALLELUJA!!!